



UDR-TR-2000-00092

DEVELOPMENT OF NEW HIGH
TEMPERATURE AND HIGH PERFORMANCE
PERMANENT MAGNET MATERIALS

• • • • •

SEPTEMBER 2000

20001010 029

UDR-TR-2000-00092

**Development of New High Temperature and High Performance
Permanent Magnet Materials**

FINAL REPORT

Prepared for:

**Office of Naval Research
800 N. Quincy Street
Arlington, VA 22217**

Prepared by:

**S. Liu and G. Edward Kuhl
Metals and Ceramics Division
University of Dayton Research Institute
Dayton, OH 45469-0170**

SEPTEMBER 2000

ABSTRACT

Permanent magnet materials capable of operating at high temperatures ($\geq 400^{\circ}\text{C}$) are required for advanced aerospace power systems. Prior to the UDRI AMPS team's successful program, the best available high temperature permanent magnets could not operate above 300°C . The problem for higher temperature operation has been that the strength of conventional magnets, as characterized by their intrinsic coercivity ($_{\text{M}}\text{H}_c$) drops sharply upon heating. The $_{\text{M}}\text{H}_c$ of the best 2:17 rare earth-transition metal permanent magnets previously available drops from 20 to 30 kOe at room temperature to only 1 to 3 kOe at 500°C . This also results in nonlinear 2nd-quadrant induction demagnetization curves (B curves) at temperatures above 200 to 300°C . A linear B curve is critical in all dynamic applications such as in generators and motors.

The UDRI AMPS team's research advanced the maximum operating temperature of permanent magnets by as much as 250°C , to 550°C . The $_{\text{M}}\text{H}_c$ of these new Sm-Co based magnets reached 9 kOe at 500°C (four to nine times higher than the current materials), with linear B curves to as high as 550°C (a 250 to 350°C increase). The temperature coefficients of $_{\text{M}}\text{H}_c$ for the new magnets can be nearly constant and can range from a small negative value ($-0.1\%/\text{ }^{\circ}\text{C}$) to near zero, or they may even be large and positive (up to $+0.27\%/\text{ }^{\circ}\text{C}$). In comparison, the temperature coefficient of $_{\text{M}}\text{H}_c$ is $-0.36\%/\text{ }^{\circ}\text{C}$ for conventional 2:17 and SmCo₅ magnets, and $-0.9\%/\text{ }^{\circ}\text{C}$ for Nd-Fe-B. In a conventional long-term aging test (500°C in air for 1,000 hours) the new magnets show a flux density loss less than one-third that of the best conventional 2:17 magnets. Using a dynamic characterization method (cycled between 0 and -6 kOe) at 400°C , the new magnet displays a dynamic energy product more than 20 times higher than the best conventional 2:17 magnet.

The UDRI AMPS team also proposed a new theory of coercivity mechanisms in permanent magnet materials based on this breakthrough result. This new theory explains the variations in the temperature dependencies of coercivity and provides important guidance to the R&D of new magnetic materials. In addition, EEC has successfully commercialized the new high temperature permanent magnets. These advances represent a major breakthrough in high temperature permanent magnet materials.

TABLE OF CONTENTS

| SECTION | PAGE |
|--|------|
| 1 BACKGROUND | 1 |
| 1.1 Introduction | 1 |
| 1.2 Requirement for High Temperature Permanent Magnet Materials | 1 |
| 1.3 Temperature Dependence of Magnetic Properties of Conventional Permanent Magnets | 2 |
| 1.4 Key Parameters to be Improved in Conventional High Temperature Permanent Magnets | 6 |
| 2 APPROACH TO SIGNIFICANTLY IMPROVING HIGH TEMPERATURE PERFORMANCE OF PERMANENT MAGNET MATERIALS | 7 |
| 2.1 Develop New $\text{Sm}_2\text{TM}_{17}$ -type Sintered Permanent Magnet Materials | 7 |
| 2.2 New Sintered Rare Earth Permanent Magnets Based on SmCo_7 Phase | 8 |
| 2.3 Temperature Compensated Permanent Magnets | 10 |
| 2.4 Nanocrystalline Composite Permanent Magnet Materials | 11 |
| 3 RESULTS AND DISCUSSIONS | 12 |
| 3.1 Effect of Fe on High Temperature Intrinsic Coercivity of $\text{Sm}(\text{Co,Fe,Cu,Zr})_z$ Magnets | 12 |
| 3.2 Effect of Sm (z value) on High Temperature Intrinsic Coercivity of $\text{Sm}(\text{Co,Fe,Cu,Zr})_z$ Magnets | 13 |
| 3.3 Effect of Cu on High Temperature Intrinsic Coercivity of $\text{Sm}(\text{Co,Fe,Cu,Zr})_z$ Magnets | 15 |
| 3.4 Effect of Zr on High Temperature Intrinsic Coercivity of $\text{Sm}(\text{Co,Fe,Cu,Zr})_z$ Magnets | 16 |

TABLE OF CONTENTS (Continued)

| SECTION | PAGE |
|--|------|
| 3.5 New Class of Sm-Co Based Sintered High temperature Permanent Magnets | 17 |
| 3.5.1 High Temperature Performance and Maximum Operating Temperature T_M | 17 |
| 3.5.2 High Temperature Coercivity and Its Temperature Coefficient | 21 |
| 3.5.3 High Temperature Dynamic Characterization | 23 |
| 3.5.4 Long-Term Thermal Stability | 27 |
| 3.5.4.1 Air Aging at 500°C | 27 |
| 3.5.4.2 Analysis of Irreversible Flux Losses in Aging | 29 |
| 3.5.5 Pinning Strength in Sm(Co,Fe,Cu,Zr) _z Magnets | 37 |
| 3.5.6 Microstructure and Crystal Structure | 39 |
| 3.5.7 Novel Temperature Dependence of Intrinsic Coercivity and New Model of Coercivity Mechanism in Sm(Co,Fe,Cu,Zr) _z Magnets | 45 |
| 3.5.7.1 Novel Temperature Dependence of Intrinsic Coercivity | 45 |
| 3.5.7.2 Description of the New Model of Coercivity | 46 |
| 3.5.7.3 Explanation of Various Temperature Dependencies of Coercivity Using the New Model | 50 |
| 3.5.7.4 Calculations of Temperature Dependence of MH_c Using the Proposed Model | 52 |
| 3.5.7.5 Discussion on the Model | 56 |
| 3.5.7.6 Applications of the New Coercivity Model | 56 |

TABLE OF CONTENTS (Concluded)

| SECTION | | PAGE |
|---------|---|------|
| 3.6 | New Sintered Rare Earth Permanent Magnets Based on SmCo ₇ Phase | 57 |
| 3.6.1 | <u>X-ray Diffraction Result and Microstructure</u> | 57 |
| 3.6.2 | <u>Effects of Compositions on Magnetic Properties</u> | 59 |
| 3.7 | Temperature-Compensated Rare Earth Permanent Magnets | 63 |
| 3.7.1 | <u>A New Approach for Calculating Temperature Coefficient</u> | 63 |
| 3.7.2 | <u>Modeling of Temperature Coefficients in (LRE-HRE)-TM Compounds</u> | 68 |
| 3.8 | Preliminary Results of Nanocrystalline Composite Permanent Magnet Materials | 71 |
| 4 | <u>CONCLUSIONS AND RECOMMENDATIONS</u> | 75 |
| 5 | <u>REFERENCES</u> | 77 |
| | <u>APPENDIX: PUBLICATIONS</u> | 80 |

LIST OF FIGURES

| FIGURE | | PAGE |
|--|--|-------------|
| 1.1 A summary of $(BH)_{\max}$ vs. temperature for most commercial permanent magnets. | | 3 |
| 1.2 A summary of MH_c vs. temperature for most commercial permanent magnets. | | 4 |
| 1.3 Temperature dependence of magnetic properties of the best conventional high temperature $Sm_2(Co,Fe,Cu,Zr)_{17}$ magnet. | | 5 |
| 1.4 Schematic illustration of importance of a linear B curve in a dynamic condition. | | 6 |
| 2.1 Saturation magnetization ($4\pi M_s$) of Sm-Co binary compounds vs. Co content. $4\pi M_s$ of $LaCo_{13}$ is also given in the figure. | | 9 |
| 3.1 High temperature intrinsic coercivity, MH_c , as a function of Fe content, v, in $Sm(Co_{\text{bal}}Fe_vCu_{0.09}Zr_{0.03})_{7.5}$. | | 13 |
| 3.2 Dependence of intrinsic coercivity of $Sm(Co_{0.795}Fe_{0.09}Cu_{0.09}Zr_{0.025})_z$ on z value at various temperatures. | | 14 |
| 3.3 Temperature dependence of intrinsic coercivity for $Sm(Co_{0.795}Fe_{0.09}Cu_{0.09}Zr_{0.025})_z$ from 300 to 600°C. | | 15 |
| 3.4 Temperature dependence of intrinsic coercivity of $Sm(Co_{\text{bal}}Fe_{0.1}Cu_{0.05}Zr_{0.025})_{7.38}$ magnet. | | 16 |
| 3.5 Demagnetization curves of magnet with $T_M = 330^\circ C$. | | 19 |
| 3.6 Demagnetization curves of magnet with $T_M = 250$ to $550^\circ C$. | | 19 |
| 3.7 Intrinsic and normal demagnetization curves of magnet with $T_M = 500^\circ C$. | | 20 |
| 3.8 Temperature dependence of intrinsic coercivity of various $Sm(Co,Fe,Cu,Zr)_z$ magnets | | 21 |
| 3.9 Temperature coefficients of various permanent magnets. Numbers (1-5) denote the same magnets as shown in Figure 3.8. | | 22 |
| 3.10 Demagnetization curves of dynamic characterization performed at 20°C. | | 24 |

LIST OF FIGURES (Continued)

| FIGURE | PAGE |
|--|------|
| 3.11 Demagnetization curves of dynamic characterization performed at 300°C. | 24 |
| 3.12 Demagnetization curves of dynamic characterization performed at 400°C. | 25 |
| 3.13 Demagnetization curves of dynamic characterization performed at 450°C. | 25 |
| 3.14 A summary of the first set of dynamic characterizations. | 26 |
| 3.15 A summary of the second set of dynamic characterizations. | 26 |
| 3.16 Loss of flux density vs. aging time at 500°C for the first 100 hours for $\text{Sm}(\text{Co}_{0.795}\text{Fe}_{0.09}\text{Cu}_{0.09}\text{Zr}_{0.025})_z$ and commercial 2:17 magnets. | 28 |
| 3.17 Loss of flux density vs. aging time at 500°C up to 2,000 hours for $\text{Sm}(\text{Co}_{0.795}\text{Fe}_{0.09}\text{Cu}_{0.09}\text{Zr}_{0.025})_z$ and commercial 2:17 magnets. | 28 |
| 3.18 Magnetic flux readings after exposure to various temperatures for 2 hours. | 31 |
| 3.19 Surface oxidation at 500 and 550°C. | 32 |
| 3.20 Relationship of surface oxidation and the exposed temperature. | 33 |
| 3.21 Magnetic loss vs. aging time at 500°C for different types of magnets. | 36 |
| 3.22 Magnetic loss vs. time at 500°C for high temperature magnets with and without coating. | 36 |
| 3.23 Intrinsic demagnetization curves for the magnetic hardening experiment. | 38 |
| 3.24 Initial magnetization curves for the magnets with different T_M . | 39 |
| 3.25 SEM micrograph of $\text{Sm}(\text{Co}_{0.794}\text{Fe}_{0.1}\text{Cu}_{0.09}\text{Zr}_{0.026})_{7.0}$ (Nominal $z = 6.46$) | 41 |
| 3.26 TEM microstructure for magnet D with $T_M = 500^\circ\text{C}$. | 41 |

LIST OF FIGURES (Continued)

| FIGURE | PAGE |
|---|------|
| 3.27 TEM microstructure for magnets D with $T_M = 500^\circ\text{C}$ and B with $T_M = 330^\circ\text{C}$. Cell size is 78 nm for magnet D, and 123 nm for magnet B. | 42 |
| 3.28 Composition map for magnet type D with $T_M = 500^\circ\text{C}$, which was obtained by using electron energy loss spectroscopy. | 43 |
| 3.29 XRD pattern of $\text{Sm}(\text{Co}_{0.794}\text{Fe}_{0.09}\text{Cu}_{0.09}\text{Zr}_{0.026})_{7.0}$ after solid solution heat treatment | 44 |
| 3.30 XRD pattern of $\text{Sm}(\text{Co}_{0.794}\text{Fe}_{0.09}\text{Cu}_{0.09}\text{Zr}_{0.026})_{7.0}$ after aging. | 44 |
| 3.31 Temperature dependence of intrinsic coercivity of sintered $\text{Sm}(\text{Co}_{\text{bal}}\text{Fe}_{0.04}\text{Cu}_{0.09}\text{Zr}_{0.027})_{7.26}$ magnet. | 45 |
| 3.32 Schematic temperature dependence of crystalline anisotropy of 2:17 cell phase and 1:5 cell boundary phase. | 47 |
| 3.33 Temperature dependence of intrinsic coercivity of $\text{Sm}(\text{Co}_{0.81}\text{Fe}_{0.025}\text{Cu}_{0.14}\text{Mn}_{0.025})_{7.0}$. | 48 |
| 3.34 Energy barrier between the 2:17 cell phase and 1:5 cell boundary phase. | 49 |
| 3.35 Assumed temperature dependence of crystalline anisotropy constant for 2:17 cell phase and 1:5 cell boundary phase. Case I, $\Delta E(T)$ decreases with T. | 52 |
| 3.36 Calculated temperature dependence of MH_c . Case I, $\Delta E(T)$ decreases with T. | 53 |
| 3.37 Assumed temperature dependence of crystalline anisotropy constant for 2:17 cell phase and 1:5 cell boundary phase. Case II, $\Delta E(T)$ increases with T. | 54 |
| 3.38 Calculated temperature dependence of MH_c . Case II, $\Delta E(T)$ increases with T. | 54 |
| 3.39 Assumed temperature dependence of crystalline anisotropy constant for 2:17 cell phase and 1:5 cell boundary phase. Case III, $\Delta E(T)$ increases rapidly with T. | 55 |

LIST OF FIGURES (Concluded)

| FIGURE | PAGE |
|---|------|
| 3.40 Calculated temperature dependence of MH_c . Case III, $\Delta E(T)$ increases rapidly with T. | 55 |
| 3.41 X-ray diffraction pattern of $Sm(Co_{bal}Cu_{0.085}Ti_{0.043})_{6.4}$. | 58 |
| 3.42 SEM micrograph of $Sm(Co_{bal}Fe_{0.15}Cu_{0.085}Ti_{0.043})_{6.4}$. | 59 |
| 3.43 Magnetic properties vs. Fe content, v, in $Sm(Co_{bal}Fe_vCu_{0.085}Ti_{0.043})_{6.4}$. | 60 |
| 3.44 Magnetic properties vs. Cu content, x, in $Sm(Co_{bal}Cu_xTi_{0.043})_{6.4}$. | 60 |
| 3.45 Magnetic properties vs. Ti content, y, in $Sm(Co_{bal}Cu_{0.085}Ti_y)_{6.4}$. | 61 |
| 3.46 Magnetic properties vs. z value in $Sm(Co_{bal}Cu_{0.085}Ti_{0.043})_z$. | 61 |
| 3.47 Demagnetization curves of $Sm(Co_{0.957}Ti_{0.043})_{6.4}$. | 62 |
| 3.48 Demagnetization curves of $Sm(Co_{0.872}Cu_{0.085}Ti_{0.043})_{6.4}$. | 62 |
| 3.49 Demagnetization curves of $Sm(Co_{0.875}Cu_{0.085}Ti_{0.04})_{6.4}$. | 63 |
| 3.50 Temperature dependence of $4\pi M$ at 10 kOe of $Gd_2(Co,Fe,Cu,Zr)_{17}$. | 65 |
| 3.51 α of $4\pi M$ at 10 kOe of some rare earth permanent magnets. | 66 |
| 3.52 α of MH_c of some rare earth permanent magnets. | 67 |
| 3.53 α of $(BH)_{max}$ of some rare earth permanent magnets. | 67 |
| 3.54 α of $4\pi M$ at 10 kOe of $(Sm_{(1-x)}Gd_x)Co_5$ vs. temperature. | 70 |
| 3.55 Temperature for zero α of $4\pi M$ and $4\pi M$ vs. Gd content in $(Sm_{(1-x)}Gd_x)Co_5$ and $(Sm_{(1-x)}Gd_x)_2TM_{17}$ systems. | 70 |
| 3.56 XRD patterns of as-spun ribbons for $Sm(Co_{0.773}Fe_{0.186}C_{0.041})_{10.44}$. | 72 |
| 3.57 XRD patterns of as-spun ribbons for $Sm(Co_{0.773}Fe_{0.186}Ti_{0.0205}C_{0.041})_{10.44}$. | 73 |
| 3.58 Figure 3.58. XRD patterns of as-spun ribbons for $Sm(Co_{0.773}Fe_{0.186}Nb_{0.0205}C_{0.041})_{10.44}$. | 73 |

LIST OF TABLES

| TABLE | PAGE |
|--|------|
| 1-1 Magnetic Properties and T_C for Most Commercial Magnet Materials | 4 |
| 2-1 Saturation Magnetization of a Few Sm-Co Compounds | 10 |
| 3-1 Maximum Operating Temperature T_M and Magnetic Properties at 25 to 600°C for $\text{Sm}(\text{Co}_w\text{Fe}_v\text{Cu}_x\text{Zr}_y)_z$ Magnets | 18 |
| 3-2 T_M , Compositions, and Temperature Coefficient β of MH_c of New Class of $\text{Sm}(\text{Co}_w\text{Fe}_v\text{Cu}_x\text{Zr}_y)_z$ Magnets | 18 |
| 3-3 Irreversible flux loss due to <i>NLC</i> Factor. (Samples were maintained at the temperature indicated for 2 hours.) | 31 |
| 3-4 Flux Losses After Aging at 300 to 400°C for 3,140 Hours | 32 |
| 3-5 Flux Losses After Aging at 500°C for 360 Hours | 34 |
| 3-6 Flux Losses After Aging at 550°C for 360 Hours | 35 |
| 3-7 Pinning Field H_p at 300°C | 39 |
| 3-8 XRD Data for $\text{Sm}(\text{Co}_{\text{bal}}\text{Fe}_v\text{Cu}_{0.085}\text{Ti}_{0.043})_{6.4}$ | 58 |
| 3-9 Temperatures for Zero α of $4\pi M$ for $(\text{Sm}_{(1-x)}\text{Gd}_x)\text{Co}_5$ and $(\text{Sm}_{(1-x)}\text{Gd}_x)_2(\text{Co,Fe,Cu,Zr})_{17}$ Magnets | 71 |
| 3-10 Composition of Sm-Co-Fe-M-C Ribbons | 71 |
| 3-11 Magnetic Properties of "Nanocomposite" Sm-CO-based Magnets | 74 |

LIST OF ACRONYMS AND SYMBOLS

| | |
|---------------------------|--|
| 2:17 | Magnets with general compositional form (Rare Earth) ₂ (Transition Metal) ₁₇ |
| 4πM | Magnetization |
| 4πM_s | Saturation magnetization |
| α | Temperature coefficient |
| α_T | Instantaneous temperature coefficient at temperature T |
| AFRL/PR | Air Force Research Laboratory Propulsion Directorate |
| AMPS | Advanced Magnets for Power Systems |
| B | Magnetic induction |
| (BH)_{max} | Maximum energy product |
| B_r | Remanence |
| E | Domain wall energy density |
| EEC | Electron Energy Corporation |
| H | External applied field |
| H_A | Magentocrystalline anisotropy field |
| H_k | Knee field |
| MH_c | Intrinsic coercivity |
| H_p | Magnetic pinning field |
| HRE | Heavy rare earth |
| IPU | Integrated power unit |
| IS/G | Internal starter/generators |
| IVD | Ion vapor deposition |
| K | Crystalline anisotropy constant |
| kG | Kilogauss |
| kOe | Kilo-Oersted |
| LRE | Light rare earth |
| μ | Permeability |
| MEA | More Electric Aircraft |
| MGOe | Megagauss Oersted |
| Q | Generalized magnetic parameter |
| SEM | Scanning electron microscopy |
| SSHT | Solid solution heat treatment |
| STTR | Small-Business Technology Transfer |
| T | Temperature |
| T_c | Curie temperature |
| TEM | Transmission electron microscopy |
| TM | Transition metal |
| T_M | Maximum temperature at which induction demagnetization curve remains a straight line |
| UD | University of Dayton |
| UDRI | University of Dayton Research Institute |
| VSM | Vibrating sample magnetometer |

1. BACKGROUND

1.1 Introduction

The University of Dayton Research Institute (UDRI), Electron Energy Corporation (EEC), and Rhodia team proposed an ONR/DARPA Advanced Magnets for Power Systems (AMPS) program entitled "Development of New High Temperature and High Performance Permanent Magnet Materials" to provide permanent magnet materials that meet the higher temperature requirements ($> 400^{\circ}\text{C}$) for advanced power systems. The University of Dayton (UD) and its Research Institute (UDRI) have long been recognized as a leading research institution in the field of development of high performance permanent magnets. EEC is the leading producer of high temperature rare earth permanent magnets in the US. Rhodia is one of the leading developers of permanent magnet materials. UDRI and EEC have successfully pioneered much of the development of the rare earth permanent magnet materials that are in use today in numerous military and commercial applications.

The UDRI/EEC/Rhodia AMPS team's research on high temperature permanent magnet materials was based on the successful completion of a US Air Force Small Business Technology Transfer (STTR) Phase I program by EEC and UDRI in which a record intrinsic coercivity at 400°C was reached. In this AMPS program, the UDRI research team systematically investigated the effects of Sm, Fe, Cu, Zr, and processing parameters on the high temperature performance of $\text{Sm}_2(\text{Co,Fe,Cu,Zr})_{17}$ ($\text{Sm}_2\text{TM}_{17}$ or 2:17) type permanent magnet materials. The UDRI AMPS team's research has led to a major breakthrough in high temperature permanent materials. The maximum operating temperature of permanent magnets has been increased from previously around 300 to 550°C . A new class of high temperature rare earth permanent magnets resulting from this research has been successfully commercialized by EEC.

1.2 Requirement for High Temperature Permanent Magnet Materials

A national initiative, led by the Air Force Research Laboratory Propulsion Directorate (AFRL/PR), is underway to develop and test a more electric aircraft (MEA). A major objective of the MEA initiative is to increase military aircraft reliability, maintainability, and supportability, including drastically reducing the need

for ground support equipment. This advancement will be accomplished in part through the development of advanced power components such as magnetic bearings, Integrated Power Units (IPU), and Internal Starter/Generators (IS/G) for main propulsion engines. New high temperature magnets are enabling technologies for the development of these new power components.

Successful completion of this project will provide permanent magnetic materials capable of operating in advanced Air Force power system components. Power system designers frequently find that these materials impose technological limitations on their designs. Compromises are generally required between the performance desired and the magnetic, mechanical, and electrical properties of available materials. New materials developed under this effort will operate at $\geq 400^{\circ}\text{C}$ and will enable new designs. Air-cooling, rather than complicated liquid cooling and its necessary logistic support, will become an operational capability. Likewise, oilless/lubeless gas turbine engines and space power systems will be possible.

1.3 Temperature Dependence of Magnetic Properties of Conventional Permanent Magnets

The basic requirements for the new permanent magnet materials for applications at temperatures higher than 400°C are high Curie temperature (at least $> 800^{\circ}\text{C}$), high magneto-crystalline anisotropy, and high saturation magnetization. At least within the foreseeable future, these requirements can be met only in the Sm-Co based system. Sm and Co form many binary compounds, such as Sm_3Co , Sm_9Co_4 , SmCo_2 , SmCo_3 , Sm_2Co_7 , SmCo_5 , and $\text{Sm}_2\text{Co}_{17}$. Among them, SmCo_5 and $\text{Sm}_2\text{Co}_{17}$ have been developed into useful high performance permanent magnets. SmCo_5 magnets have been commercially available since the mid-1970s. It is a mature technology and has little room for further development. On the other hand, the metallurgical and magnetic behaviors of $\text{Sm}_2\text{Co}_{17}$ -based permanent magnet materials are far from being fully understood. It has proven to be very difficult to develop high coercivity in the $\text{Sm}_2\text{Co}_{17}$ compound. In order to develop useful coercivity, a considerable amount of nonmagnetic elements, such as Cu and Zr, must be added. In order to enhance saturation magnetization, Fe is added, which results in a very complicated metallurgical system of $\text{Sm}_2(\text{Co,Fe,Cu,Zr})_{17}$ ($\text{Sm}_2\text{TM}_{17}$ or 2:17) [1-3].

Figures 1.1 and 1.2 summarize maximum energy product $(BH)_{max}$ and intrinsic coercivity MH_c vs. temperature properties for most commercial permanent magnetic materials. Magnetic properties including Curie temperature (T_C) for all these materials are shown in Table 1-1. These data were obtained at EEC using a KJS hysteresigraph. As shown in Figures 1.1 and 1.2 and Table 1-1, the magnetic properties of rare earth magnets are superior to all other magnet materials. Among rare earth magnets, Nd-Fe-B-type magnets have the highest static $(BH)_{max}$ at temperatures $T < 130^\circ\text{C}$. At $T > 130^\circ\text{C}$, Sm-TM magnets have the highest $(BH)_{max}$.

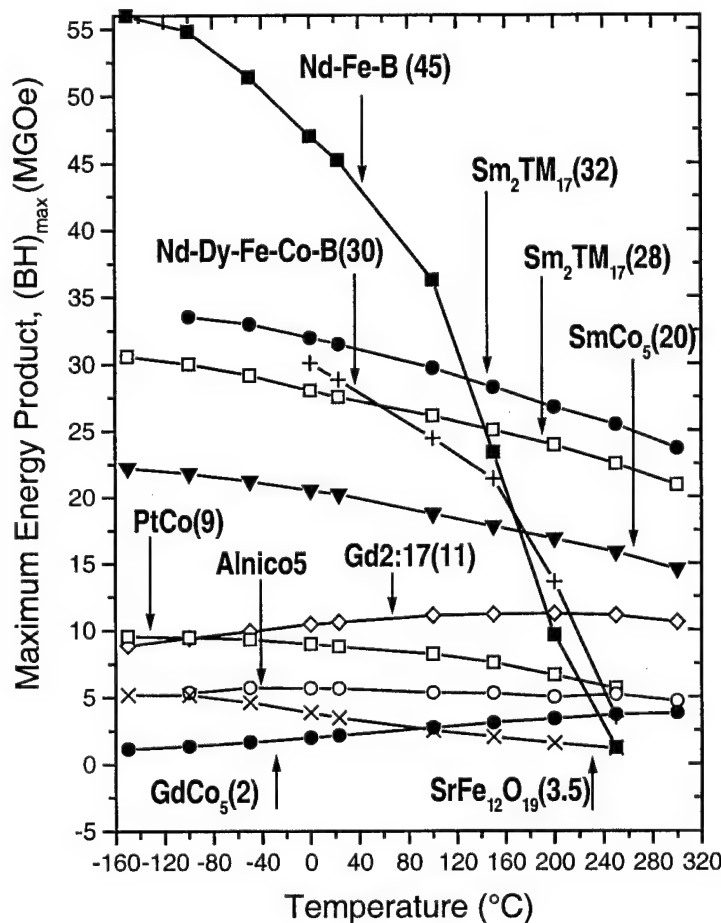


Figure 1.1. A summary of $(BH)_{max}$ vs. temperature for most commercial permanent magnets.

The values in parentheses are $(BH)_{max}$ at 25°C .

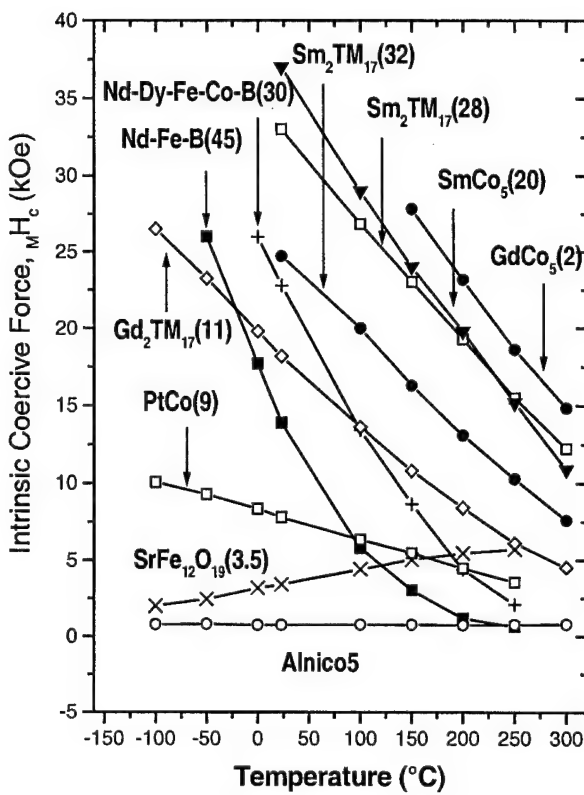


Figure 1.2. A summary of M_H_c vs. temperature for most commercial permanent magnets.

The values in parentheses are $(BH)_{max}$ at 25°C.

Table 1-1. Magnetic Properties and T_c for Most Commercial Magnet Materials

| Material | At 25°C | | | | At 250°C | | | | T_c (°C) |
|---------------------|------------|--------------|--------------|---------------------|------------|--------------|--------------|---------------------|------------|
| | B_r (kG) | BH_c (kOe) | MH_c (kOe) | $(BH)_{max}$ (MGoe) | B_r (kG) | BH_c (kOe) | MH_c (kOe) | $(BH)_{max}$ (MGoe) | |
| $Nd_{14}Fe_{80}B_6$ | 13.79 | 13.70 | 13.9 | 45.2 | 8.65 | 0.63 | 0.65 | 1.52 | 310 |
| (Nd,Dy)-Fe-Co-B | 10.97 | 10.64 | 25 | 29.1 | 7.32 | 2.10 | 1.50 | 3.50 | 340 |
| Sm_2TM_{17} (A) | 11.67 | 10.69 | 25 | 31.5 | 10.65 | 8.68 | 10.3 | 25.4 | 805 |
| Sm_2TM_{17} (B) | 10.74 | 10.14 | 33 | 27.5 | 9.81 | 9.03 | 15.5 | 22.5 | 820 |
| $SmCo_5$ | 9.02 | 8.95 | 29 | 20.2 | 8.07 | 7.86 | 15.2 | 15.8 | 691 |
| Gd_2TM_{17} | 6.79 | 6.10 | 18.2 | 10.6 | 7.12 | 5.25 | 6.10 | 11.1 | 830 |
| $GdCo_5$ | 2.92 | 2.89 | >45 | 2.1 | 3.86 | 3.78 | 18.62 | 3.69 | 710 |
| PtCo (isotropic) | 6.40 | 6.85 | 7.66 | 9.5 | 5.27 | 2.95 | 3.55 | 5.63 | 475 |
| Alnico 5 | 12.84 | 0.74 | 0.75 | 5.3 | 12.22 | 0.73 | 0.75 | 5.18 | 840 |
| $SrFe_{12}O_{19}$ | 3.85 | 3.34 | 3.39 | 3.5 | 2.18 | 2.00 | 5.72 | 1.16 | 450 |

The best conventional high temperature 2:17 magnets can operate up to 300°C. The problem associated with higher temperature ($> 300^\circ\text{C}$) operation has been that the intrinsic coercivity ($_{\text{M}}\text{H}_c$) of these magnets drops sharply upon heating. Among all magnetic parameters of 2:17 magnets, $_{\text{M}}\text{H}_c$ possesses the largest negative temperature coefficient. At around room temperature, the temperature coefficients of $_{\text{M}}\text{H}_c$, $(\text{BH})_{\text{max}}$, and B_r of a typical high coercivity type of 2:17 magnet are -0.36, -0.10, and -0.03 $\text{%/}^\circ\text{C}$, respectively. Upon heating, $_{\text{M}}\text{H}_c$ of 2:17 magnets drops sharply from their room temperature values of 20 to 30 kOe (or higher) to 3 to 6 kOe at 400°C and 1 to 3 kOe at 500°C . Figure 1.3 shows the temperature dependence of magnetic properties of the best conventional high temperature $\text{Sm}_2(\text{Co,Fe,Cu,Zr})_{17}$ magnet.

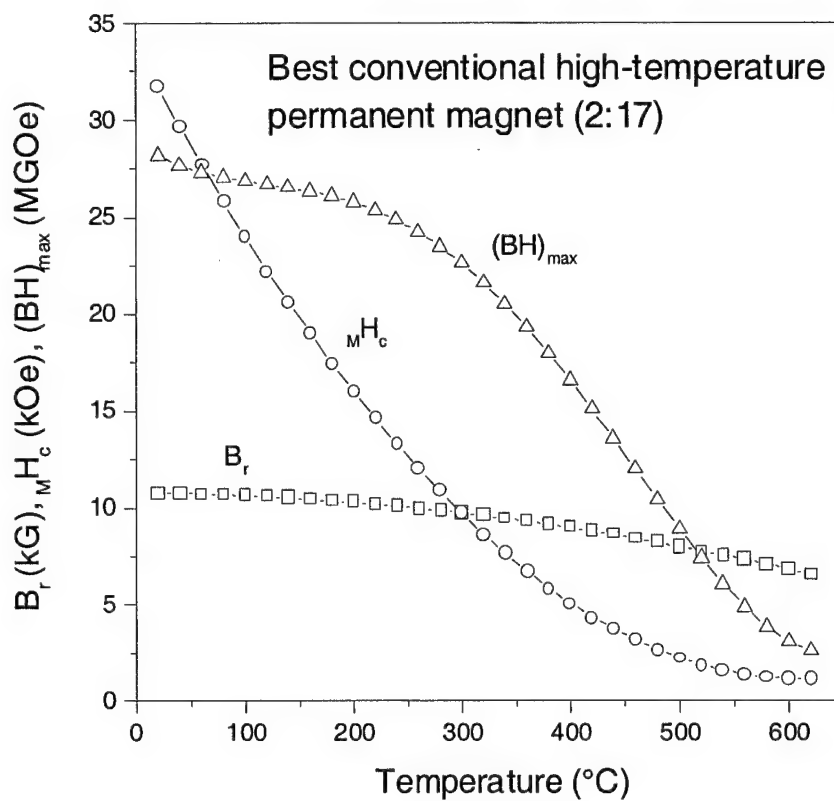


Figure 1.3. Temperature dependence of magnetic properties of the best conventional high temperature $\text{Sm}_2(\text{Co,Fe,Cu,Zr})_{17}$ magnet.

1.4 Key Parameters to be Improved in Conventional High Temperature Permanent Magnets

Low intrinsic coercivity at high temperatures results in nonlinear 2nd-quadrant induction demagnetization curves (B curves) above $\approx 300^{\circ}\text{C}$. A linear 2nd-quadrant B curve is critical in all dynamic applications, such as in generators and motors. Therefore, in order to meet the requirement of operation above 400°C , the current 2:17 magnets must be substantially improved. The key is to increase their Curie temperature and their intrinsic coercivity at high temperatures.

The importance of a linear induction demagnetization curve in dynamic applications is schematically illustrated in Figure 1.4. In a dynamic application, the working point of a magnet keeps cycling. If its intrinsic coercivity is low, then its induction demagnetization curve can be nonlinear. Under this circumstance, the work point of the magnet can be reduced to below the knee in the induction demagnetization curve and its induction can be significantly reduced irreversibly. If the intrinsic coercivity of the magnet is sufficiently high, then its induction demagnetization curve will be linear. Under this circumstance, its induction will be reversible around the working point even at a quite low permeance value.

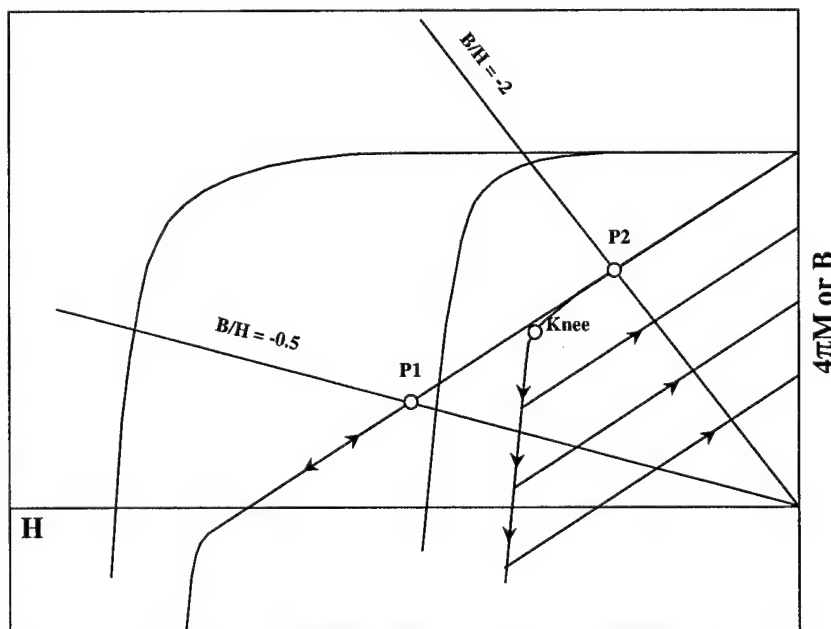


Figure 1.4. Schematic illustration of importance of a linear B curve in a dynamic condition.

Therefore, in order to increase the operating temperature of sintered rare earth permanent magnets, the key is to increase their intrinsic coercivity at high temperature, so that their induction demagnetization curves remain linear at the operating temperatures. The maximum operating temperature, T_M , of a magnet is the temperature limit at which the induction demagnetization curve of the magnet still keeps its linearity. As mentioned before, this temperature for the best conventional high temperature magnets was around 300°C.

2. APPROACH TO SIGNIFICANTLY IMPROVING HIGH TEMPERATURE PERFORMANCE OF PERMANENT MAGNET MATERIALS

2.1 Develop New $\text{Sm}_2\text{TM}_{17}$ -type Sintered Permanent Magnet Materials

In 1981, S. Liu et al. [4] measured the magnetic properties of SmCo_5 and $\text{Sm}_2\text{TM}_{17}$ magnets to temperatures as high as 727°C and observed that a SmTM_z magnet with $z = 7$ had higher MH_c at high temperatures than the magnet with $z = 7.43$. A. Kim [5] reported that a SmTM_z magnet with $z = 7$ and a high Cu content demonstrated low temperature coefficient of MH_c . In recent years, it has been observed that the high temperature stability of 2:17 magnets is very sensitive to the Fe content in magnet alloys. High Fe content (low Co content) resulted in low MH_c at high temperatures [6-8]. A recent experiment by C. Chen et al. has established that reducing Fe content (increasing Co content) leads to much higher intrinsic coercivity at high temperatures [9]. More recently, J. F. Liu et al. [10] investigated the relationship between MH_c and z , Cu, and Fe contents in SmTM_z ingot magnets. Their study showed that the high temperature stability of 2:17 magnets can be improved by applying lower z (higher Sm content), lower Fe content (higher Co content), and higher Cu content in the magnet alloys.

In this study, we systematically investigated the effects of changing Fe, Sm, Cu, and Zr on high temperature performance, with an emphasis on high temperature intrinsic coercivity, of sintered $\text{Sm}_2(\text{Co},\text{Fe},\text{Cu},\text{Zr})_{17}$ -type permanent magnets. In our study, sintered magnets were prepared using induction melting and conventional powder metallurgy techniques. The alloy compositions were $\text{Sm}(\text{Co}_w\text{Fe}_v\text{Cu}_x\text{Zr}_y)_z$ with $v = 0 - 0.22$, $x = 0 - 0.12$, $y = 0 - 0.04$, $w = 1-v-x-y$, and effective $z = 7.14 - 8.10$. The effective z is defined as the atomic ratio of the transition metals to the metallic part of Sm. Fine

powders with particle size \approx 3 to 5 μm were aligned in a pulsed magnetic field of \approx 100 kOe and then compacted using an isostatic press. The green bodies were sintered at 1180 to 1220°C for 1 to 3 hours in Ar, solid solution heat treated at 1160 to 1190°C for 2 to 4 hours, and then aged at 750 to 850°C for 10 to 30 hours, followed by a slow cooling to 400°C. The magnetic characterizations were performed at 20 to 600°C using a vibrating sample magnetometer (VSM). Since VSM characterization is an open-circuit measurement, careful calibration was done to ensure that the results were equivalent to those made by a closed-circuit hysteresigraph. In order to obtain an accurate temperature indication, a Pt/Pt-Rh thermocouple was installed with its tip very close to the sample. In addition, He was used to improve the thermal conductivity in sample holder.

2.2 New Sintered Rare Earth Permanent Magnets Based on SmCo_7 Phase

The $\text{Sm}_2\text{Co}_{17}$ compound has the highest Curie temperature (920°C) and moderately high saturation magnetization and crystalline anisotropy among all of the rare earth-transition metal compounds. However, as mentioned before, it is very difficult to develop high coercivity in $\text{Sm}_2\text{Co}_{17}$ compound. In order to obtain useful coercivity, a considerable amount of nonmagnetic elements, such as Cu and Zr, must be added, which results in significantly reduced magnetization and energy product. Another disadvantage of the current $\text{Sm}_2(\text{Co,Fe,Cu,Zr})_{17}$ magnets is that a long-term heat treatment is necessary to develop high coercivity.

The SmCo_7 phase is a metastable binary phase in the Sm-Co binary system. It has a TbCu_7 crystal structure and the structure can be derived from that of SmCo_5 [11-12]. The SmCo_7 compound has a saturation magnetization and Curie temperature lower than $\text{Sm}_2\text{Co}_{17}$ but higher than the SmCo_5 compound. Figure 2.1 illustrates the saturation magnetization of Sm-Co compounds versus Co content in Sm-Co binary compounds. The experimentally determined saturation magnetization of LaCo_{13} and the estimated saturation magnetization of SmCo_7 are also given in Figure 2.1. It can be seen in Figure 2.1 that the saturation magnetization of Sm-Co binary compounds increases linearly with Co content.

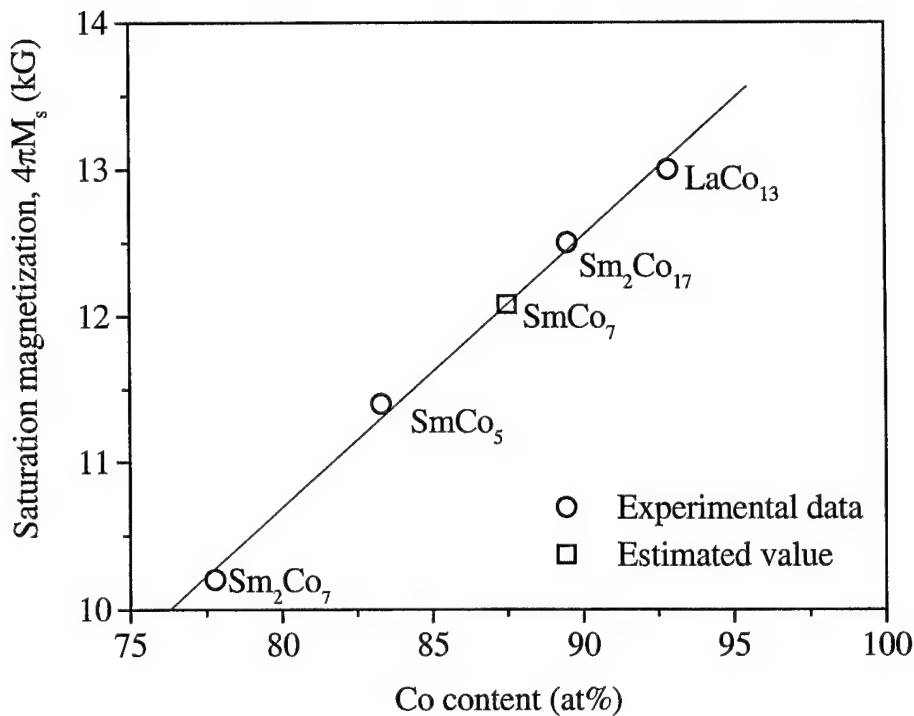


Figure 2.1. Saturation magnetization ($4\pi M_s$) of Sm-Co binary compounds vs. Co content.

$4\pi M_s$ of LaCo_{13} is also given in the figure.

It has been reported that the metastable SmCo_7 phase can be obtained by melt-spinning [12], splat cooling [13], or mechanical alloying [14]. It has been also reported that some transition metals, such as Zr and Ti, can stabilize the SmCo_7 phase [15-16]. Recently, P. Liu [16] reported that high coercivity and a positive temperature coefficient of coercivity were obtained without aging in $\text{SmCo}_{7-x}\text{Ti}_x$ and $\text{SmCo}_{7-x-y}\text{Cu}_x\text{Ti}_y$ cast alloys. If the Ti and/or Ti, Cu substitutions can be made very low, and if the Fe substitution for Co can effectively enhance the saturation magnetization as it does in the $\text{Sm}_2(\text{Co},\text{Fe})_{17}$ system, then it would be possible for these 1:7 based compounds to have a virtually higher saturation magnetization than $\text{Sm}_2(\text{Co},\text{Fe},\text{Cu},\text{Zr})_{17}$ magnets (Table 2-1). In addition, if high coercivity can be developed without long-term aging, it would be also very significant for cutting the cost of production. Therefore, we believe that now is the time to explore the possibility of synthesizing sintered anisotropic magnet materials based on the SmCo_7 phase.

Table 2-1. Saturation Magnetization of a Few Sm-Co Compounds

| Compound | $4\pi M_s$ (kG) | Reference |
|--|-----------------|-----------|
| SmCo ₅ | 11.4 | [17] |
| SmCo ₇ | 12.1 | estimated |
| Sm(Co _{0.8} Fe _{0.2}) ₇ | 13.7 | estimated |
| Sm ₂ Co ₁₇ | 12.5 | [17] |
| Sm ₂ (Co _{0.8} Fe _{0.2}) ₁₇ | 14.0 | [18] |
| Sm ₂ (Co _{0.72} Fe _{0.2} Cu _{0.06} Zr _{0.02}) _{7.4} * | 12.0 | [18] |

*Sintered magnet

2.3 Temperature Compensated Permanent Magnets

New high temperature and high performance permanent magnet materials for future Department of Defense power system applications may be required to operate in environments involving temperature cycling from 20 to 400°C or higher. When heated from 20 to 400°C, the (BH)_{max} of the best 2:17 magnets drops from 28 to 17 MGOe - a 39% loss. Obviously, a small temperature coefficient of (BH)_{max} over a wide range of operating temperatures is required for applications involving temperature cycling.

A small temperature coefficient of magnetization, and in turn (BH)_{max}, can be realized by internal temperature compensation. This is based on the fact that in the rare earth transition metal compounds (RE_xTM_y) the magnetic moment coupling between RE and TM atoms depends on the type of RE utilized in the alloy. When the RE is a light rare earth (LRE) such as Ce, Pr, Nd, or Sm, the RE moment couples parallel to the TM moment (ferromagnetic coupling). The compound moment in this case exhibits a decrease with increasing temperature over the entire temperature range up to the Curie temperature. In contrast, when the RE is a heavy rare earth (HRE) such as Gd, Tb, Dy, Ho, Er, etc., the RE moment couples antiparallel to the TM moment (ferrimagnetic coupling). In this case, variations of the compound moment versus temperature are more complex because the response of the magnetization of each sublattice to temperature is different. It is possible that in a certain temperature range the compound moment

increases with increasing temperature. Therefore, by partial substitution of some HRE elements for LRE elements in magnet alloys, the compensation for the loss of magnetization during heating can be obtained.

In the past 25 years, many researchers have worked on reduction of the temperature coefficient of B_r in the temperature range of -50°C to $+150^{\circ}\text{C}$. Benz et al. in 1974 [19] and Jones et al. in 1976 [20] demonstrated partial substitution of Gd and Ho for Sm in SmCo_5 . Martis et al. in 1978 [21] explored the potential of using Tb, Dy or Er in the SmCo_5 magnets. Narasimhan in 1981 [22] studied partial substitution of Dy, Ho, Er, and Gd for Sm in SmCo_5 magnets. Li et al. in 1980 and 1983 [23,24] prepared the first temperature compensated $\text{RE}_2\text{TM}_{17}$ magnets of the low MH_C variety. Mildrum et al. in 1983 [25] applied the concept to high MH_C $\text{RE}_2\text{TM}_{17}$ magnets by incorporating Er.

The efforts described above led to the production of temperature compensated magnets which have been satisfying many special applications with near zero temperature coefficients up to 150°C . EEC has been providing the $(\text{Sm, Gd})\text{Co}_5$ magnets with near zero temperature coefficient from -50°C to $+150^{\circ}\text{C}$ since 1974, and $(\text{Sm, Gd})_2\text{TM}_{17}$ since 1986. For applications at 300°C and higher, the magnetic properties obtained by combining light and heavy rare earth elements require further investigation.

2.4 Nanocrystalline Composite Permanent Magnet Materials

In recent years, progress in the development of nanocrystalline composite permanent magnet materials has been notable [26-29]. The distinguishing feature of this new type of permanent magnet material is that they are composed of a mixture of two ultra-fine hard and soft phases, for example $\text{Nd}_2\text{Fe}_{14}\text{B}$ and $\alpha\text{-Fe}$. This composite structure combines the high saturation magnetization of a soft magnetic phase and the high magneto-crystalline anisotropy of a hard magnetic phase. Theoretical analysis assumes that the exchange interactions between the hard and soft ultra-fine grains enhance the remanence and stabilize the magnetization direction of the magnetically soft phase. This would result in a moderately high intrinsic coercivity in these composite materials. This has been confirmed by experiments. Therefore, nanocrystalline composite magnet materials hold great promise for future development.

Recent studies on nanocrystalline composite magnets have focused primarily on isotropic $\text{Nd}_2\text{Fe}_{14}\text{B}/\alpha\text{-Fe}$ and $\text{Sm}_2\text{Fe}_{17}\text{N}_3/\alpha\text{-Fe}$ systems [30-34]. The low Curie temperatures of the hard magnetic phases in these systems (312°C for $\text{Nd}_2\text{Fe}_{14}\text{B}$ and 560°C for $\text{Sm}_2\text{Fe}_{17}\text{N}_3$) certainly limit their usefulness for high temperature applications. The UDRI AMPS team proposed to investigate magnetic properties and thermal stability of nanocrystalline composite $\text{Sm}_2\text{Co}_{17}/\text{Co}$, $\text{Sm}_2(\text{C}_{0.7}\text{Fe}_{0.3})_{17}/\text{Co}_{0.65}\text{Fe}_{0.35}$, SmCo_5/Co , and $\text{SmCo}_5/\text{Co}_{0.65}\text{Fe}_{0.35}$ permanent magnet material systems. The Curie temperature and $4\pi M_s$ of the $\text{Sm}_2(\text{C}_{0.7}\text{Fe}_{0.3})_{17}$ compound are 840°C and 14.5 kG, while those of the $\text{Co}_{0.65}\text{Fe}_{0.35}$ phase are 985°C and 24.5 kG, respectively. The theoretical upper limit of $(\text{BH})_{\text{max}}$ for the nanocrystalline composite $\text{Sm}_2(\text{C}_{0.7}\text{Fe}_{0.3})_{17}/\text{Co}_{0.65}\text{Fe}_{0.35}$, with a 60% volume fraction of the magnetically hard phase, is as high as 86 MGOe. With materials properties such as these, new nanocrystalline composite magnet materials hold great promise if they can be developed into new high performance permanent magnets for high temperature applications. Since the anisotropy field of the SmCo_5 compound is as high as 300 kOe, it may be easier to obtain high coercivity in a nanocrystalline composite system containing SmCo_5 than in one containing $\text{Sm}_2\text{Co}_{17}$.

3. RESULTS AND DISCUSSIONS

3.1 Effect of Fe on High Temperature Intrinsic Coercivity of $\text{Sm}(\text{Co,Fe,Cu,Zr})_z$ Magnets

Results of a systematic investigation of intrinsic coercivity as a function of Fe content in $\text{Sm}(\text{Co}_{\text{bal}}\text{Fe}_v\text{Cu}_{0.09}\text{Zr}_{0.03})_{7.5}$ at high temperatures from 400 to 600°C are given in Figure 3.1. It should be noted that the Fe content of conventional 2:17 magnets is $v = 0.21$ to 0.31, much higher than the Fe content in magnet materials in this study. It can be seen in Figure 3.1 that high temperature intrinsic coercivity increases rapidly with decreasing Fe content (increasing Co content) in the magnet alloys. At 400°C, the intrinsic coercivity increases from 5.6 kOe at $v = 0.22$ to 12.7 kOe at $v = 0.1$. Continued decrease in Fe results in lower coercivity. Or, in other words, at 400°C a coercivity peak appears when $v = 0.1$. This coercivity peak shifts to $v = 0.7$ at higher temperatures. Apparently, the effect of Fe content is closely related to the higher Curie temperature and higher magnetocrystalline anisotropy in magnet alloys with lower Fe (higher Co) content.

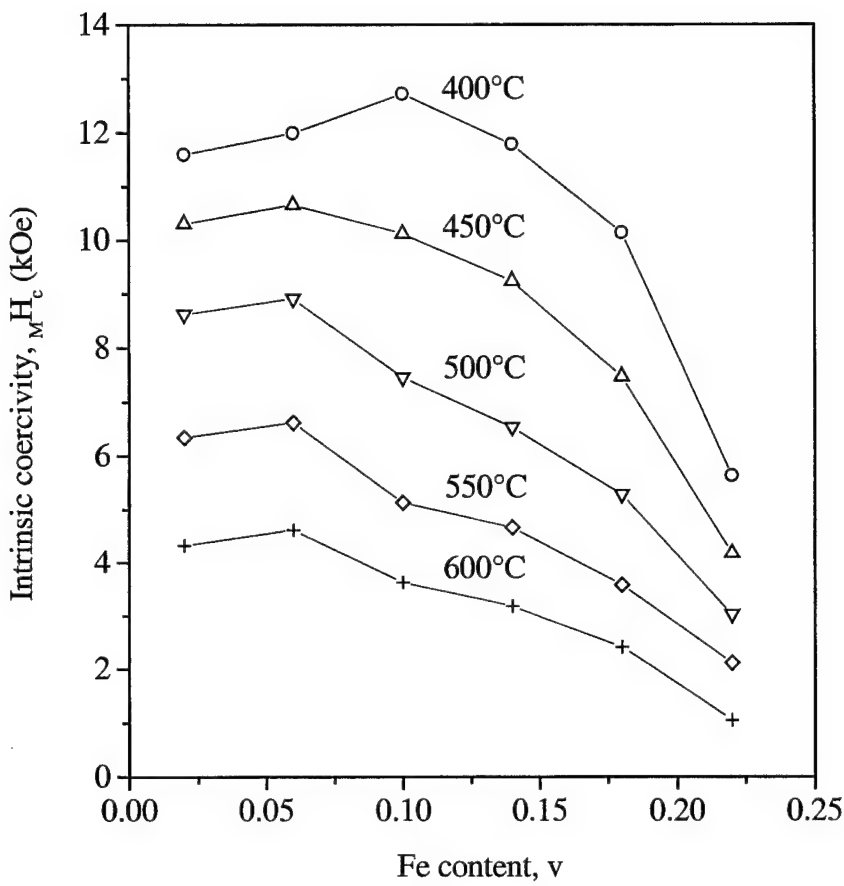


Figure 3.1. High temperature intrinsic coercivity, M_H_c , as a function of Fe content, v, in $Sm(Co_{bal}Fe_vCu_{0.09}Zr_{0.03})_{7.5}$.

3.2 Effect of Sm (z value) on High Temperature Intrinsic Coercivity of $Sm(Co,Fe,Cu,Zr)_z$ Magnets

Figure 3.2 summarizes the effect of z value on the intrinsic coercivity (M_H_c) of $Sm(Co_{0.795}Fe_{0.09}Cu_{0.09}Zr_{0.025})_z$ magnets. The effective z value in most conventional 2:17 magnets is approximately 8.3, – a value much higher than all magnets presented in this figure. It can be seen in Figure 3.2 that M_H_c is very sensitive to the z value at room temperature and that M_H_c increases rapidly with increasing z. As temperature rises, especially when $T \geq 500^\circ C$, M_H_c becomes less sensitive to z. It can be seen that there is a peak (denoted by pk) in each M_H_c -z curve in the temperature range of 300 to 500°C. When z is smaller than the z value corresponding to the peak M_H_c , M_H_c increases with z;

when z is larger than the z value corresponding to the peak MH_c , MH_c decreases with z . It is interesting to note that as temperature increases, the z value corresponding to the peak MH_c shifts toward lower values of z . As shown in Figure 3.2, the effective z values corresponding to the peak MH_c at 300, 450, and 500°C are 7.86, 7.62, and 7.38, respectively. It is obvious that at room temperature the peak should occur at $z \geq 8.10$, while at 550 and 600°C the peaks should occur at $z \leq 7.14$. It can be seen from Figure 3.2 that MH_c becomes more and more sensitive to temperature with increasing z . This trend can be seen more clearly in Figure 3.3, which shows the temperature dependence of MH_c for $Sm(Co_{0.795}Fe_{0.09}Cu_{0.09}Zr_{0.025})_z$. It can be seen in Figure 3.3 that when the effective $z = 7.14$, the coercivity slightly increases with increasing temperature in the temperature range from 300 to 450°C. As z increases, MH_c gradually increases in the temperature range of 300 to 450°C and displays an increased negative temperature coefficient up to $z = 7.62$. Further increasing z results in a very large negative temperature coefficient for MH_c . When z exceeds 7.86, the MH_c decreases with z over the entire temperature range from 300 to 600°C.

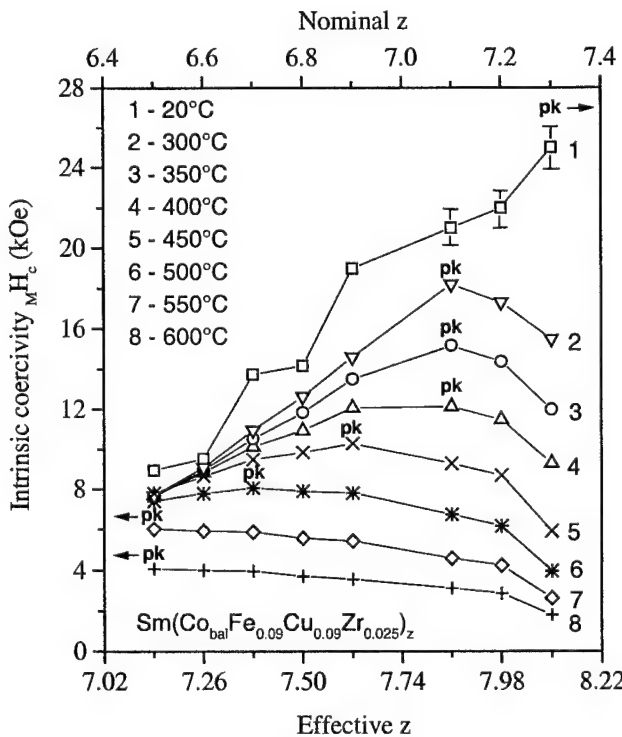


Figure 3.2. Dependence of intrinsic coercivity of $Sm(Co_{0.795}Fe_{0.09}Cu_{0.09}Zr_{0.025})_z$ on z value at various temperatures.

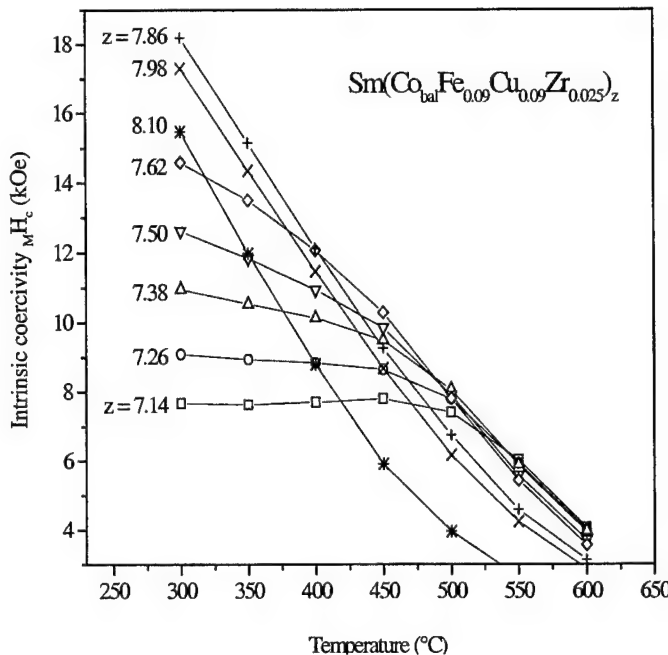


Figure 3.3. Temperature dependence of intrinsic coercivity for $\text{Sm}(\text{Co}_{0.795}\text{Fe}_{0.09}\text{Cu}_{0.09}\text{Zr}_{0.025})_z$ from 300 to 600°C.

3.3 Effect of Cu on High Temperature Intrinsic Coercivity of $\text{Sm}(\text{Co,Fe,Cu,Zr})_z$ Magnets

It is well known that coercivity in $\text{Sm}_2(\text{Co,Fe,Cu,Zr})_{17}$ type of magnets originates from the pinning of domain wall in Cu-rich cell boundary phase in a fine scaled cellular microstructure. Therefore, sufficient Cu content is essential in order to develop high coercivity at both room temperature and high temperatures. Generally speaking, M_{H_c} increases with x monotonously. However, the effect of Cu on increasing M_{H_c} is quite different at different temperatures. It was observed that when a magnet contained very low Cu, its M_{H_c} could have a positive temperature coefficient. Figures 3.4 shows the temperature dependence of M_{H_c} from 20 to 700°C for $\text{Sm}(\text{Co}_{\text{bal}}\text{Fe}_{0.09}\text{Cu}_{0.05}\text{Zr}_{0.025})_{7.38}$. Upon heating from room temperature, M_{H_c} first slightly drops and remains low from 100 to 400°C. When temperature is above 400°C, M_{H_c} increases rapidly and forms a maximum at 550°C. The intrinsic coercivity of this magnet at 550°C is 3.7 times higher than that at room temperature. This abnormal temperature dependence of intrinsic coercivity is explained in Section 3.5.7.

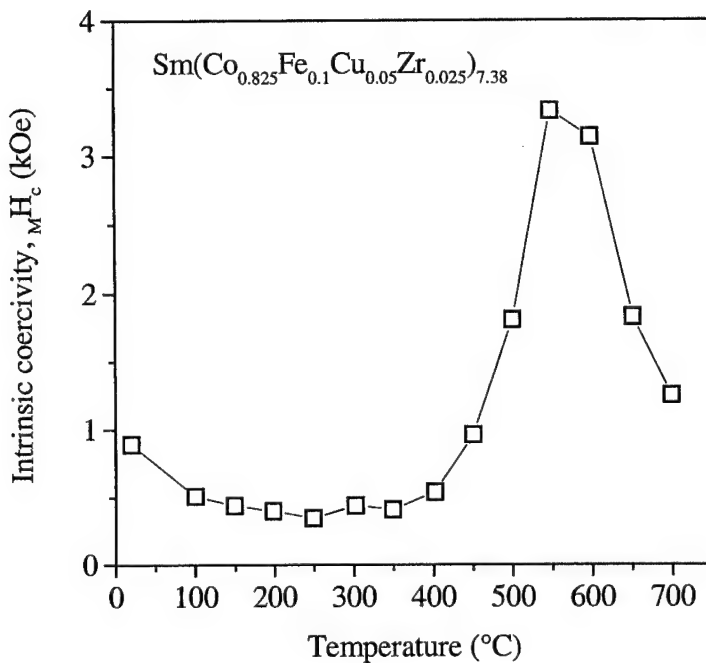


Figure 3.4. Temperature dependence of intrinsic coercivity of $\text{Sm}(\text{Co}_{0.825}\text{Fe}_{0.1}\text{Cu}_{0.05}\text{Zr}_{0.025})_{7.38}$ magnet.

3.4 Effect of Zr on High Temperature Intrinsic Coercivity of $\text{Sm}(\text{Co,Fe,Cu,Zr})_z$ Magnets

Zr has an important effect on the development of coercivity in $\text{Sm}_2(\text{Co,Fe,Cu,Zr})_{17}$ type magnets. According to A. Ray's metallurgical model on $\text{Sm}_2(\text{Co,Fe,Cu,Zr})_{17}$ magnet alloys [2,35,36], Zr-vacancy pairs occupy some of the dumbbell sites in the 2:17 rhombohedral (2:17R) precursor at the solutionizing temperature. This effectively stabilizes the 2:17R precursor as it is cooled below the magnetic ordering temperature by significantly reducing the preference of Fe for the dumbbell sites. At low temperature, the disorder represented by the Zr-vacancy pairs becomes destabilized. At the isothermal aging temperature, the strong tendency of the 2:17R crystal structure to order is initiated by the precipitation of the Zr-rich platelet phase. This results in a matrix phase slightly Sm-rich of 2:17 stoichiometry. The re-establishment of 2:17 stoichiometry and the fact that the matrix phase is supersaturated by Cu appear to be the driving forces for the subsequent precipitation of the Sm- and Cu-rich 1:5 cell boundary phase.

It has been observed in this study that Zr is critical in developing high coercivity at both low and high temperatures even when Fe content is low. It was observed that intrinsic coercivity rapidly increased with increasing Zr and that the peak coercivity value was reached at an optimum Zr content. The squareness of the second-quadrant demagnetization curve is strongly depended on Zr content in magnet alloys. The knee field rapidly enhances with increasing Zr content.

3.5 New Class of Sm-Co Based Sintered High Temperature Permanent Magnets

Based on our systematic investigations of the $\text{Sm}(\text{Co},\text{Fe},\text{Cu},\text{Zr})_z$ system, the effects of all components (Sm, Co, Fe, Cu, Zr) are thoroughly understood, especially their effect on the maximum operating temperature, T_M , of magnets. This enabled us to make a new class of Sm-Co based sintered high temperature permanent magnets with new record operating temperature.

3.5.1 High Temperature Performance and Maximum Operating Temperature T_M

The magnetic properties of $\text{Sm}(\text{Co}_w\text{Fe}_v\text{Cu}_x\text{Zr}_y)_z$ ($w+v+x+y = 1$) magnets are shown in Table 3-1. Magnets A and B have the maximum operating temperature $T_M = 250$ and 330°C , respectively. They were the best high temperature magnets prior to this work. Magnets C, D, and E have $T_M = 400$, 500 , and 550°C , respectively. They were developed in this work for use at $T \geq 400^\circ\text{C}$. It is noted that magnet A has the highest static $(\text{BH})_{\text{max}}$ (31.5 MGOe) at room temperature, and the lowest static $(\text{BH})_{\text{max}}$ at $T \geq 500^\circ\text{C}$. Co content, w, the ratio of transition metal to Sm, z, and the temperature coefficients of ${}_{\text{M}}\text{H}_c$, β , for each magnet are given in Table 3-2. It is observed that as w increases (or v decreases), T_M increases, and the value of β is reduced. A higher T_M magnet has a lower z, or higher Sm. The effective z also affects T_M . Higher T_M requires a slightly lower z. Figure 3.5 shows the induction demagnetization curves for the previous highest T_M magnet with $T_M = 330^\circ\text{C}$. Figure 3.6 shows the demagnetization curves at each T_M for the magnet types A through E. Figure 3.7 shows intrinsic and normal demagnetization curves for magnet type D with $T_M = 500^\circ\text{C}$ at different temperatures. All induction demagnetization curves shown in Figure 3.7 are essentially linear.

Table 3-1. Maximum Operating Temperature T_M and Magnetic Properties at 25 to 600°C for
 $\text{Sm}(\text{Co}_w\text{Fe}_v\text{Cu}_x\text{Zr}_y)_z$ Magnets

| Magnet Type | T_M (°C) | 25°C | | 300°C | | 400°C | | 500°C | | 600°C | |
|-------------|------------|------------------|--------|------------------|--------|------------------|--------|------------------|--------|------------------|--------|
| | | ${}_M H_c$ (kOe) | (MGOe) |
| A* | 250 | 25 | 31.5 | 8.1 | 23.7 | 3.4 | 13.8 | 1.5 | 5.9 | 0.7 | 2.3 |
| B* | 330 | 33 | 27.5 | 11.6 | 21.0 | 5.4 | 16.7 | 2.9 | 8.7 | 1.2 | 3.5 |
| C | 400 | 34 | 24.6 | 14.6 | 18.8 | 8.8 | 16.5 | 4.7 | 12.5 | 2.1 | 5.6 |
| D | 500 | 29 | 20.8 | 16.7 | 15.6 | 12.4 | 13.2 | 7.3 | 10.4 | 3.6 | 6.8 |
| E | 550 | 25 | 16.4 | 17.0 | 12.0 | 13.2 | 9.9 | 8.8 | 7.6 | 4.7 | 5.2 |

* The best high temperature magnets prior to this project.

Table 3-2. T_M , Compositions, and Temperature Coefficient β of ${}_M H_c$ of New Class of
 $\text{Sm}(\text{Co}_w\text{Fe}_v\text{Cu}_x\text{Zr}_y)_z$ Magnets

| Magnet Type | T_M (°C) | Co content | | Average β (%/°C) of ${}_M H_c$ for the Temperature Range | | |
|-------------|------------|------------|------|--|------------|------------|
| | | z^* | w | 25 – 300°C | 25 – 400°C | 25 – 500°C |
| A | 250 | 7.9 | 0.64 | -0.246 | -0.230 | -0.198 |
| B | 330 | 7.8 | 0.68 | -0.236 | -0.223 | -0.192 |
| C | 400 | 7.7 | 0.73 | -0.207 | -0.198 | -0.181 |
| D | 500 | 7.6 | 0.78 | -0.154 | -0.153 | -0.157 |
| E | 550 | 7.6 | 0.81 | -0.116 | -0.128 | -0.136 |

* z is the effective z .

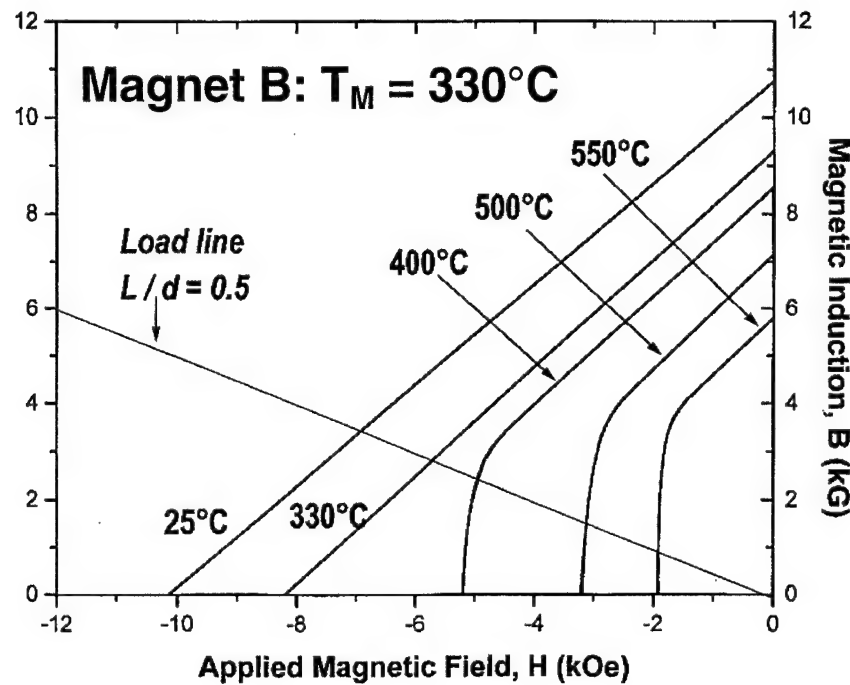


Figure 3.5. Demagnetization curves of magnet with $T_M = 330^\circ\text{C}$.

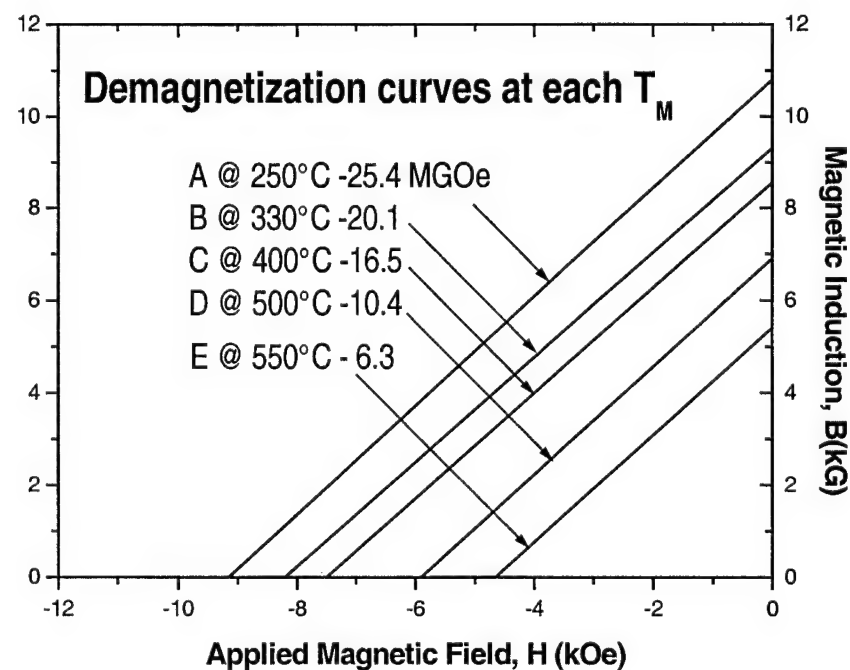


Figure 3.6. Demagnetization curves of magnet with $T_M = 250$ to 550°C .

Magnet D ($T_M = 500^\circ\text{C}$) DEMAGNETIZATION CURVES, $f(T)$

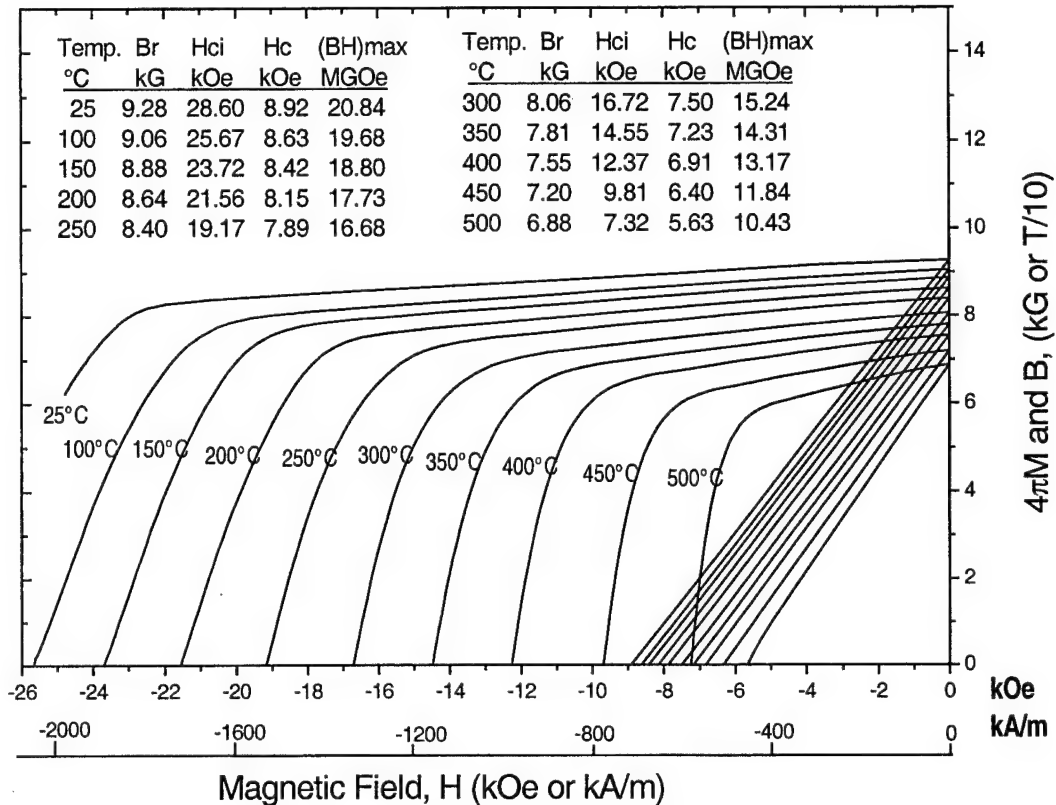


Figure 3.7. Intrinsic and normal demagnetization curves of magnet with $T_M = 500^\circ\text{C}$.

It has been determined that for each desired maximum operating temperature T_M , there is a discrete Co content for the magnet. The relationship of Co content, w , and T_M can be expressed as:

$$w = 0.5332 + 0.0004935 T_M \quad (200^\circ\text{C} \leq T_M \leq 550^\circ\text{C}) \quad (3-1)$$

This equation makes it possible to determine the amount of Co needed in the magnet while producing the highest possible $(BH)_{\text{max}}$ and a linear induction demagnetization curve for each high temperature application.

3.5.2 High Temperature Coercivity and Its Temperature Coefficient

As mentioned in Section 1.3, in conventional high temperature 2:17 magnets the intrinsic coercivity MH_c possesses a very large negative temperature coefficient. The temperature coefficient of MH_c in typical high coercivity types of 2:17 magnets is -0.36% at around room temperature.

Figure 3.8 displays the temperature dependence of MH_c of some newly developed sintered Sm-Co based permanent magnets. In comparison, the temperature dependence of MH_c of a high coercivity type of conventional 2:17 magnet is also shown as Curve 1 in the figure. It can be seen from Figure 3.8 that the MH_c of the new magnets is less temperature sensitive in comparison to the conventional 2:17 magnet. At temperatures above 100°C, the MH_c of $Sm(Co_{bal}Fe_{0.09}Cu_{0.09}Zr_{0.03})_{7.69}$ (Curve 2) is higher than that of the conventional 2:17 magnet. At 400°C, its MH_c is three times higher than that of the conventional magnet. Curve 4 has a very flat portion at a quite high coercivity level from 200 to 400°C. From room temperature to 450°C, the MH_c of $Sm(Co_{bal}Fe_{0.09}Cu_{0.09}Zr_{0.025})_{7.14}$ remains almost constant (Curve 5), making its temperature coefficient very close to zero over this wide temperature range.

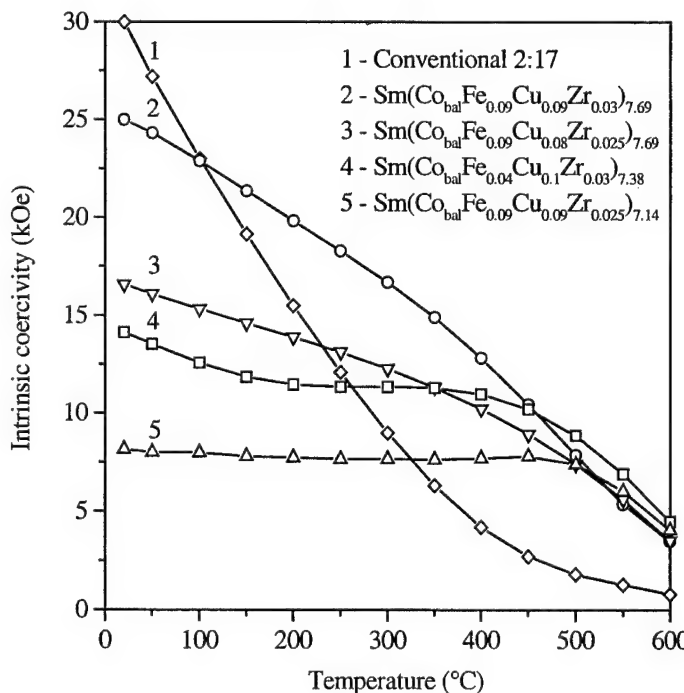


Figure 3.8. Temperature dependence of intrinsic coercivity of various $Sm(Co,Fe,Cu,Zr)_z$ magnets.

The variation of temperature coefficients of MH_c as a function of temperature for the magnets shown in Figure 3.8 is given in Figure 3.9. As a comparison, Figure 3.9 also gives temperature coefficients of MH_c for a typical SmCo₅, a Nd-Fe-B, and a newly developed magnet with positive temperature coefficient of MH_c . The temperature coefficient of MH_c demonstrated in Figure 3.6 is defined as:

$$\beta = \frac{d(MH_c)}{dT} \times \frac{100}{M H_c} \quad (\%/\text{°C}) . \quad (3-2)$$

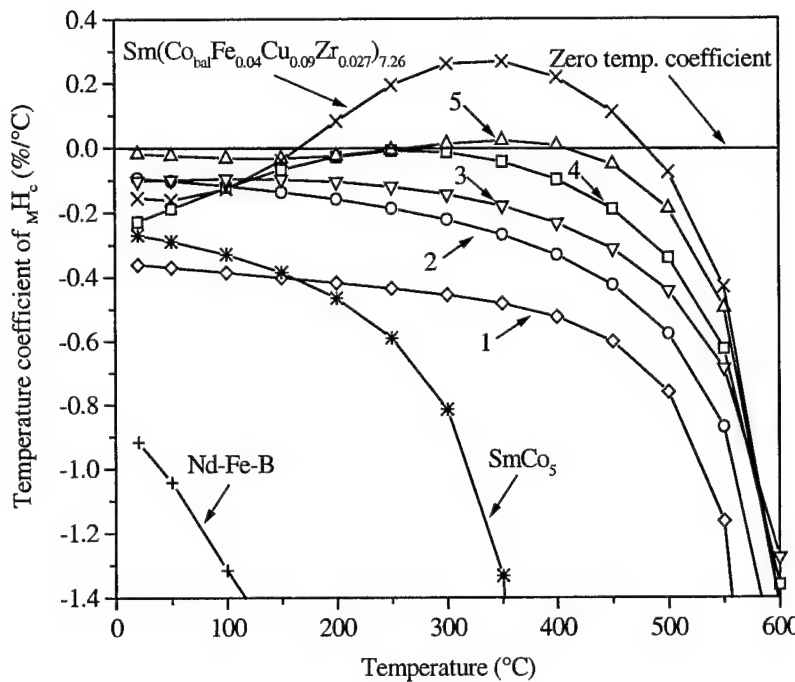


Figure 3.9. Temperature coefficients of various permanent magnets. Numbers (1-5) denote the same magnets as shown in Figure 3.8.

3.5.3 High Temperature Dynamic Characterizations

It is important to realize that the typical magnetic characterization is a static characterization. Its results are only meaningful for the static applications in which the working point of a magnet in the 2nd-quadrant induction demagnetization curve is fixed. Examples of static applications of magnets include loud speakers and magnetic recording. Data obtained from a static characterization do not necessarily represent the real capability of a magnet in dynamic applications in which the working point of the magnet in the induction demagnetization curve is cycled. Examples of dynamic applications are motors, generators, magnetic bearings, and magnetic actuators.

Because these important applications of permanent magnets are dynamic applications, it is of the utmost importance to know the capability of a magnet under dynamic rather than static conditions. This is especially true for magnets operating at high temperatures. Bearing this in mind, we devised two sets of dynamic characterizations. In the first one, the magnet specimens were first magnetically cycled under an applied demagnetizing field of 0 to BH_c before their magnetic properties were determined. The first set of characterizations was performed from room temperature to 500°C. The second set of characterizations was carried out at a fixed temperature, 400°C, with various applied demagnetizing fields ranging from 0 to 9 kOe. We compared the dynamic magnetic properties of the new magnets with those of the best conventional 2:17 magnets in these two sets of dynamic characterizations. The maximum operating temperature of the magnet specimens used in these dynamic characterizations is 450°C.

Results of the first set of dynamic characterizations are given in Figures 3.10 through 3.13 and summarized in Figure 3.14. It can be seen from these figures that at room temperature the conventional 2:17 has higher dynamic $(BH)_{max}$. However, at about 250°C, the dynamic $(BH)_{max}$ of the conventional 2:17 begins to sharply decrease. At 400°C, its $(BH)_{max}$ drops to less than 1/20 of the new magnet. Results of the second set of dynamic characterizations are summarized in Figure 3.15. It is obvious that the maximum applied demagnetizing field to which the best conventional 2:17 can be subjected without a significant loss of $(BH)_{max}$ was about 2 kOe, while for the new magnet it is as high as 8 kOe.

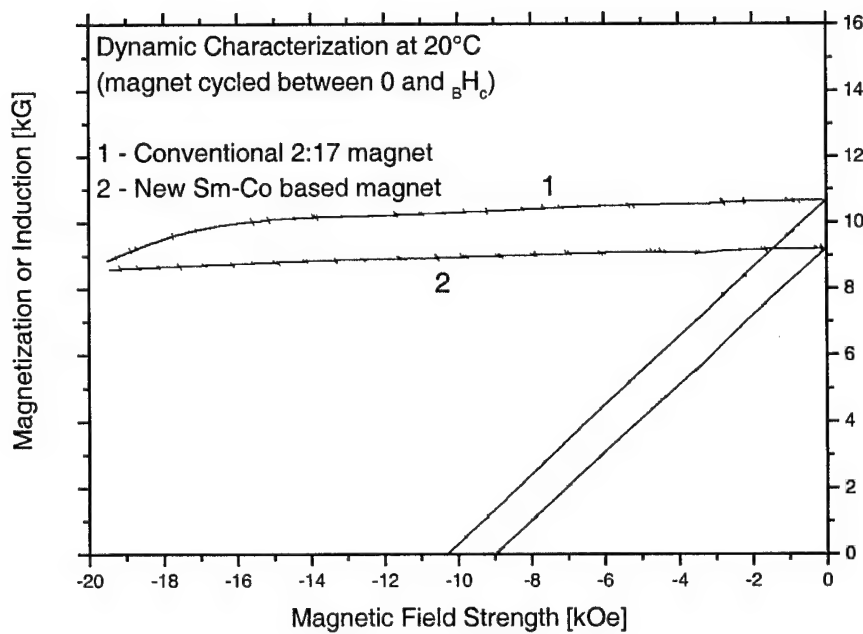


Figure 3.10. Demagnetization curves of dynamic characterization performed at 20°C.

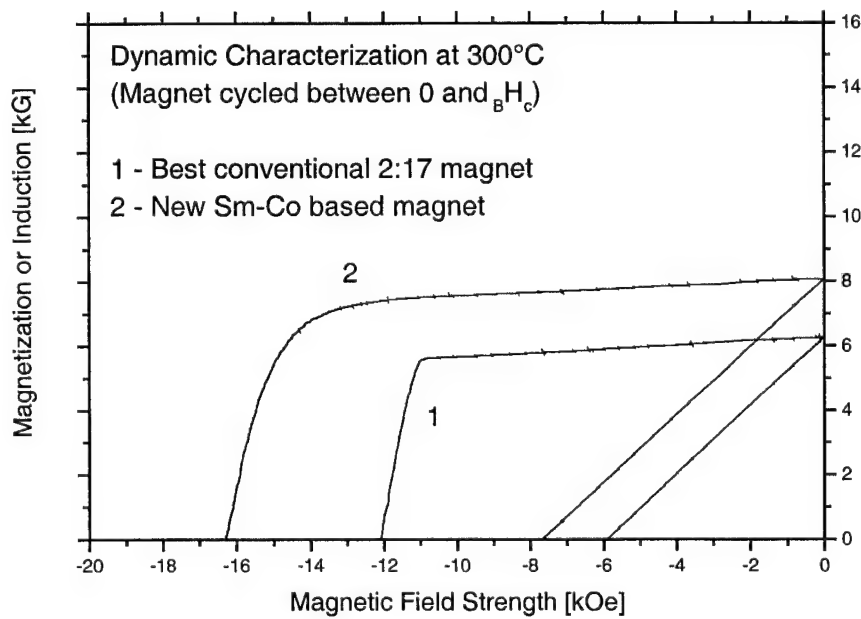


Figure 3.11. Demagnetization curves of dynamic characterization performed at 300°C.

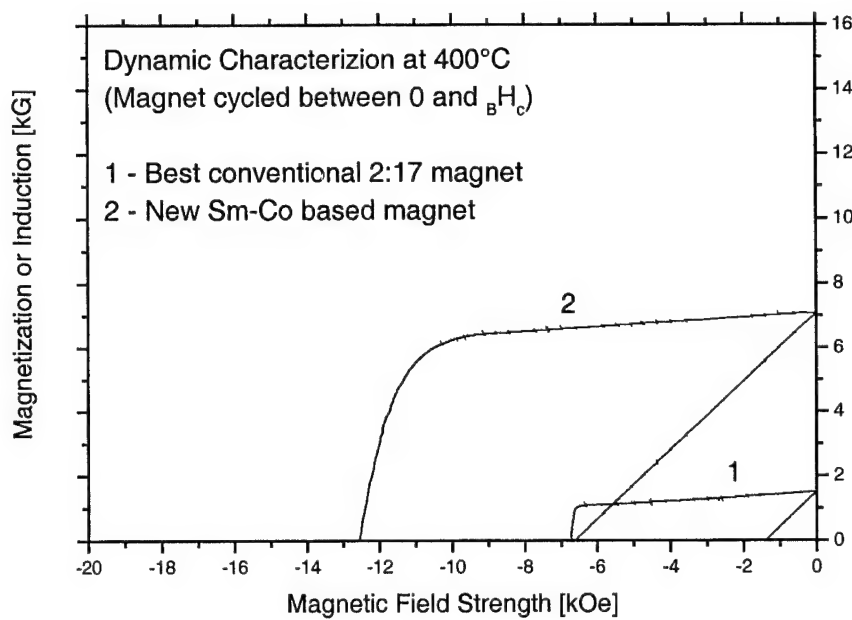


Figure 3.12. Demagnetization curves of dynamic characterization performed at 400°C.

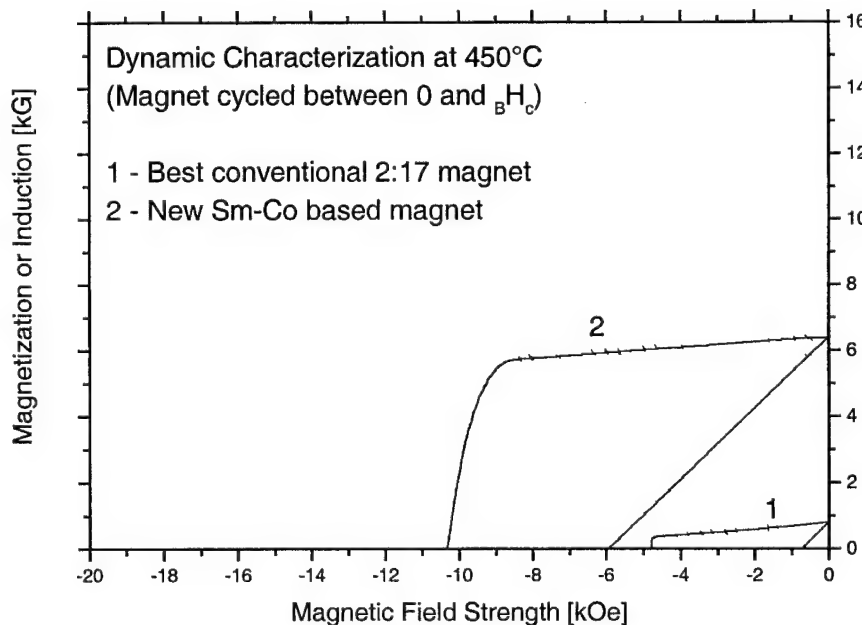


Figure 3.13. Demagnetization curves of dynamic characterization performed at 450°C.

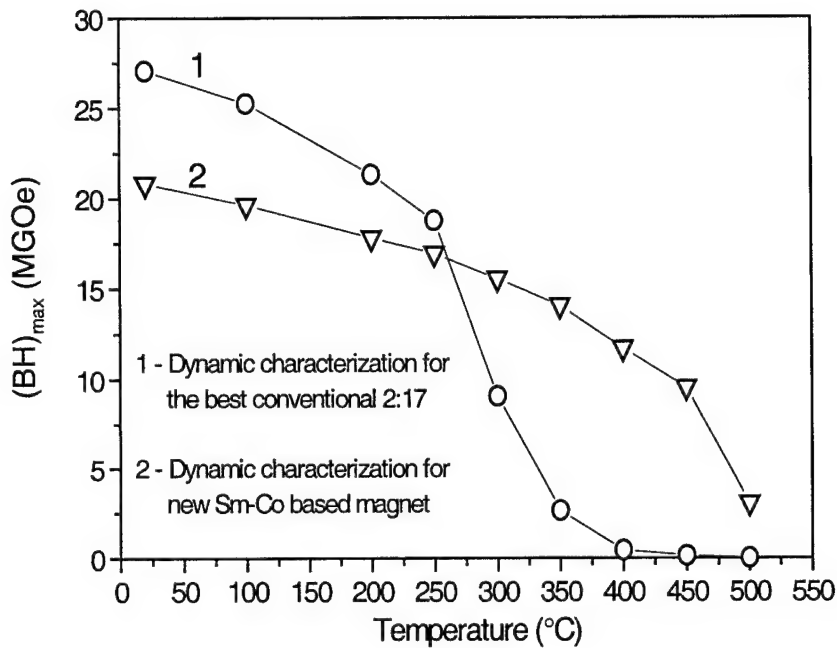


Figure 3.14. A summary of the first set of dynamic characterizations.

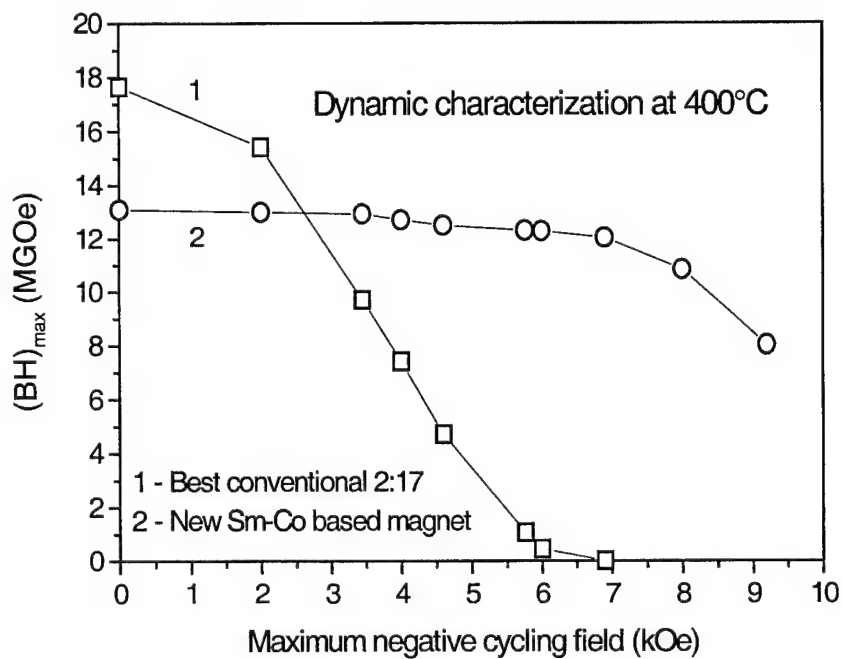


Figure 3.15. A summary of the second set of dynamic characterizations.

3.5.4 Long-Term Thermal Stability

The above experimental results illustrate the excellent static and dynamic performance of the newly developed sintered Sm-Co based magnets at high temperatures. Its long-term stability at high temperatures, then, became a great concern. We employed conventional long-term aging experiments to test the loss of magnetic flux density after aging in air at high temperatures.

3.5.4.1 Air Aging at 500°C

Figure 3.16 shows the loss of flux density in the first 100 hours when aged in air at 500°C for $\text{Sm}(\text{Co}_{0.795}\text{Fe}_{0.09}\text{Cu}_{0.09}\text{Zr}_{0.025})_z$ with effective $z = 7.26, 7.62, 7.86$, and 8.10 . In comparison, data for the best conventional high temperature 2:17-28 magnet (room temperature $(\text{BH})_{\text{max}} = 28$ MGOe) and a conventional 2:17-30 magnet (room temperature $(\text{BH})_{\text{max}} = 30$ MGOe) are also included in the figure. Figure 3.17 shows the loss of flux density after aging for up to 2000 hours for the same magnets. It is obvious from Figure 3.17 that the newly developed magnets display significantly lower losses of flux density than the conventional 2:17 magnets under the same test conditions. The magnet with $z = 7.62$ gives the best long-term stability. Magnets with z values lower or higher than 7.62 illustrate relatively larger losses. It is observed that the magnet with $z = 7.26$ displays the largest loss among the four new magnets, although at high temperatures it has higher MH_c than magnets with $z = 7.86$ and $z = 8.10$ (Figure 3.2). This is related to the fact that it has a low room temperature MH_c .

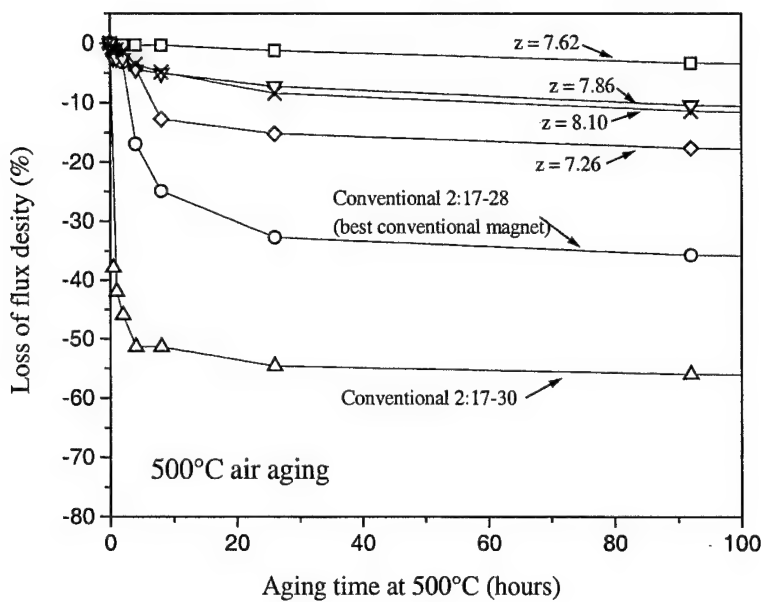


Figure 3.16. Loss of flux density vs. aging time at 500°C for the first 100 hours for $\text{Sm}(\text{Co}_{0.795}\text{Fe}_{0.09}\text{Cu}_{0.09}\text{Zr}_{0.025})_z$ and commercial 2:17 magnets.

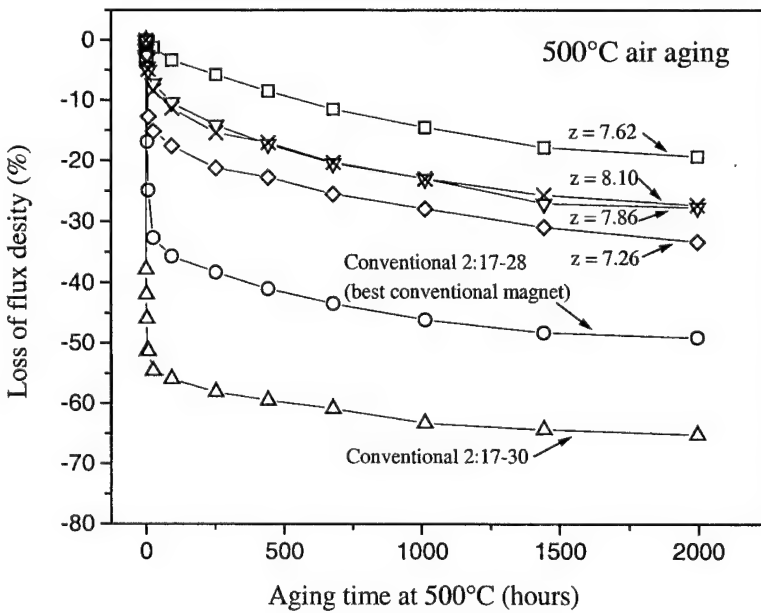


Figure 3.17. Loss of flux density vs. aging time at 500°C up to 2,000 hours for $\text{Sm}(\text{Co}_{0.795}\text{Fe}_{0.09}\text{Cu}_{0.09}\text{Zr}_{0.025})_z$ and commercial 2:17 magnets.

It can be seen from Figure 3.17 that most of the loss of flux density occurs in the first few hours in the aging test. This is especially true for the conventional 2:17 magnets. The nonlinearity of the induction demagnetization curves of the conventional 2:17 magnets at 500°C can explain this phenomenon. The conventional long-term aging test is a static test, not a dynamic test. However, the magnet specimens being tested were not only subjected to their own self-demagnetizing field, but also to the field produced by their neighboring specimens. In our experimental set-up, all specimens were placed in the same orientation. In this case, the field produced by a neighbor was a demagnetizing field. Thus, the working point of a magnet specimen could be reduced to below the knee in the induction demagnetization curve if its induction demagnetization was not linear. When the specimen was removed from its neighbors before the characterization, its flux density could not be restored to its original value. On the other hand, the new magnets demonstrate linear 2nd-quadrant induction demagnetizing curves. Therefore, their initial losses of flux density are far lower than the conventional 2:17 magnets. The magnet with $z = 7.62$ does not show any initial loss at all. This can also explain the large magnetization difference between the new magnets and the best conventional high temperature magnet shown in the dynamic characterization (Figures 3.11 through 3.13), in which the applied demagnetizing field lowered the working point of the conventional 2:17 magnet to below the knee in the induction curve. After the initial losses, the loss of flux density continues to increase gradually. This can be attributed primarily to the oxidation of the magnet surfaces.

3.5.4.2 Analysis of Irreversible Flux Losses in Aging

The irreversible flux losses in aging consist of three parts: (1) loss due to a nonlinear induction demagnetization curve (*NLC*), (2) loss due to surface oxidation (*SO*), and (3) loss due to metallurgical change (*MC*).

The Loss Due to *NLC*: Figure 3.18 shows the magnetic flux after exposure to each temperature in air for 2 hours. This 2-hour effect is primarily due to the *NLC* factor. Changes due to *SO* and *MC* factors occur over a longer period of time. The *NLC* factor is actually the largest factor for magnets used at temperatures $T > T_M$ and results in significant irreversible loss. At $T > T_M$, all magnets have nonlinear induction demagnetization curves which are characterized by a “knee.” When the load line of the magnet falls at or below the knee, significant irreversible loss occurs (Figure 1.4). At $T \leq 400^\circ\text{C}$, metallurgical change is unlikely to occur because the final stage of heat treatment was 400°C to obtain fine precipitation in the magnetic phase. The irreversible flux losses due to the *NLC* factor are listed in Table 3-3.

The Loss Due to Surface Oxidation and Metallurgical Change: The loss due to surface oxidation, *SO*, and metallurgical changes, *MC*, becomes more severe with increasing temperature and time at high temperature. Tables 3-4 through 3-6 list flux losses of different types of magnets aged at various temperatures. As given in Table 3-4, the maximum loss due to *SO* is only $\leq 0.5\%$ after 3,140 hours at 300°C for all the magnets. The irreversible loss due to the *SO* factor increases to $\sim 6\%$ after 3,140 hours at 400°C . Surface oxidation is severe at temperatures $\geq 500^\circ\text{C}$. Figure 3.19 shows micrographs of surface oxidation at 500°C and 550°C with different aging times. Some cracks were observed underneath the oxidation layers. These cracks were caused by the difference of thermal expansion coefficients between the oxide layer and the metal. It is noted in Figure 3.19 (c) that a nonuniform coating (or porous coating) cannot protect the sample from oxidation. The oxidation layers in some areas are as thick as the magnet without a coating.

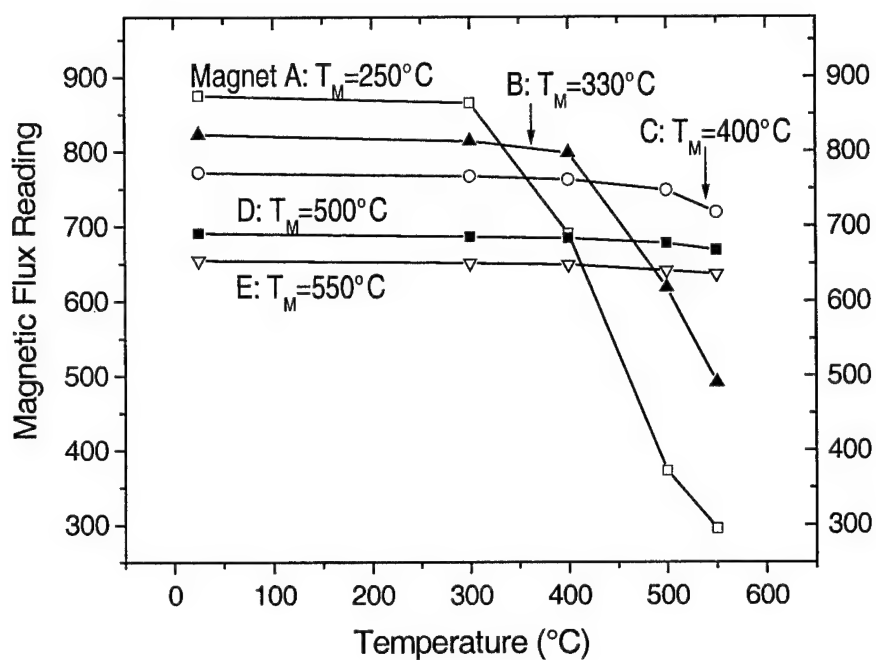


Figure 3.18. Magnetic flux readings after exposure to various temperatures for 2 hours.

Table 3-3. Irreversible Flux Loss Due to *NLC* Factor. (Samples were maintained at the temperature indicated for 2 hours.)

| Magnet Type | (BH) _{max} @ 25°C (MGoe) | T _M (°C) | Irreversible Flux Loss (%) | | | |
|-------------|-----------------------------------|---------------------|----------------------------|-------|-------|-------|
| | | | 300°C | 400°C | 500°C | 550°C |
| A | 32 | 250 | -1.1 | -21.1 | -57.7 | -66.0 |
| B | 28 | 330 | -1.1 | -3.5 | -25.1 | -39.9 |
| C | 24 | 400 | -0.6 | -1.6 | -3.3 | -7.2 |
| D | 20 | 500 | -0.6 | -1.0 | -2.1 | -3.4 |
| E | 16 | 550 | -0.6 | -0.7 | -1.7 | -2.7 |

Table 3-4. Flux Losses After Aging at 300 to 400°C for 3,140 Hours

| Magnet | T _M | Magnetic Loss (%) After 3,140 Hours | | | | | |
|--------|----------------|-------------------------------------|------|------|----------|------|-------|
| | | At 300°C | | | At 400°C | | |
| Type. | (°C) | Total | SO | NLC | Total | SO | NLC |
| A | 250 | -2.2 | -0.5 | -1.7 | -33.5 | -5.5 | -28.0 |
| B | 330 | -1.5 | -0.2 | -1.3 | -10.6 | -5.4 | -5.2 |
| C | 400 | -1.0 | -0.2 | -0.8 | -8.1 | -5.9 | -2.2 |
| D | 500 | -0.8 | -0.1 | -0.7 | -7.4 | -6.2 | -1.2 |
| E | 550 | -0.6 | -0.1 | -0.5 | -6.7 | -5.7 | -1.0 |

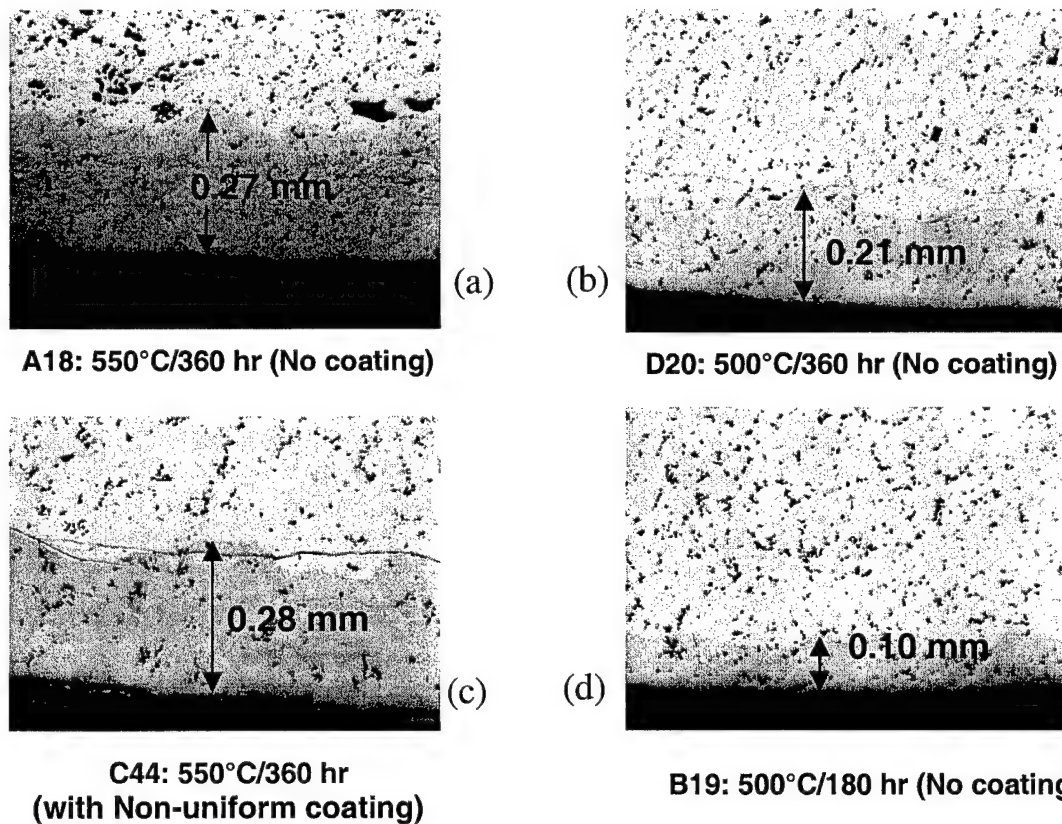


Figure 3.19. Surface oxidation at 500 and 550°C.

The loss due to *SO* is ~ 9% after 360 hours at 500°C, and ~16% after 360 hours at 550°C. As shown in Figure 3.20, the loss due to *SO* vs. temperature is an exponential function. For this experimental condition, an equation is established by using the average data from all of the samples:

$$SO \text{ Loss} = 0.023 e^{T/83} \quad (3-3)$$

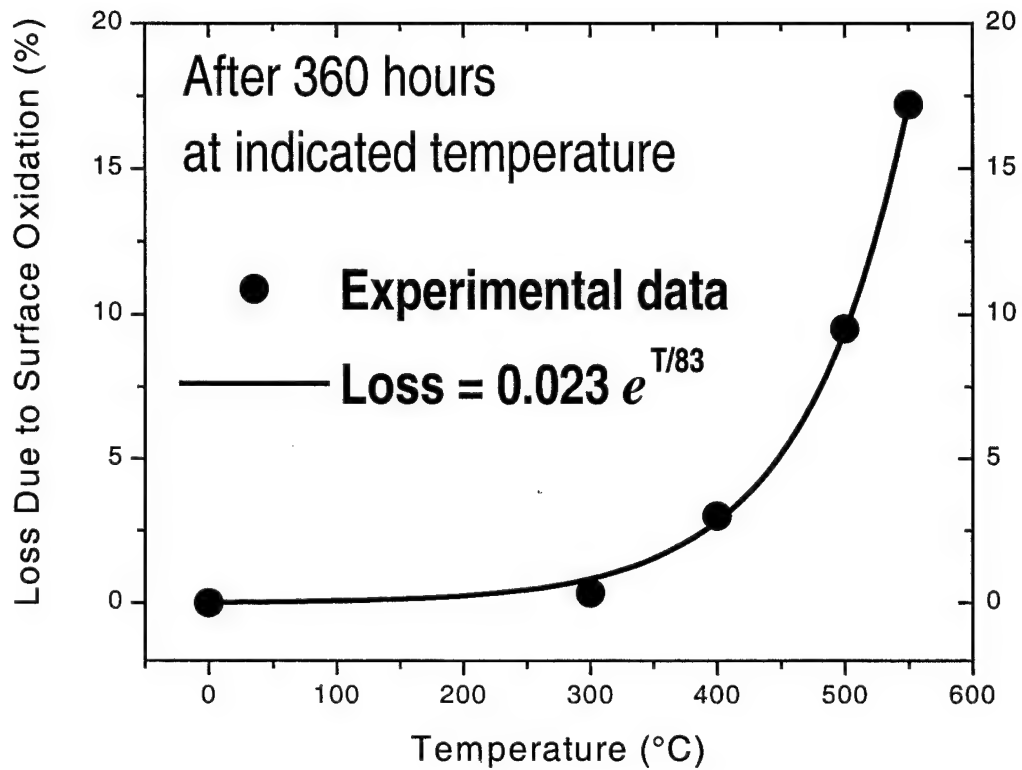


Figure 3.20. Relationship of surface oxidation and the exposed temperature.

Table 3-5. Flux Losses After Aging at 500°C for 360 Hours

| Magnet | T _M (°C) | Magnetic Loss (%) | | |
|----------|------------------------|-------------------|---------|-------|
| | | Total | SO & MC | NLC |
| I. D. | | | | |
| A | 250 | -70.1 | -11.1 | -59.0 |
| B | 330 | -40.4 | -11.0 | -29.4 |
| C | 400 | -15.9 | -11.1 | -4.8 |
| D | 500 | -12.4 | -10.5 | -1.9 |
| E | 550 | -12.0 | -10.9 | -1.1 |
| Coated C | | -5.9 | -1.7 | -4.2 |
| Coated D | | -4.3 | -2.3 | -2.3 |
| Coated E | | -4.2 | -2.9 | -1.3 |

Coating can significantly reduce the *SO* loss. Figure 3.21 shows the irreversible loss vs. time at 500°C for the magnets without a coating. Figure 3.22 shows magnetic loss vs. time at 500°C for high temperature magnets with and without coating. These results indicate that the coating reduced the *SO* loss by more than 70% for magnet types C, D, and E after 360 hours at 500°C, even though the coating was not applied effectively. In this study, a coating was applied by painting the magnet with a high temperature ceramic coating material. Some edges were peeled off during each interval of testing. Figure 3-19 (shows a coated magnet sample C44 with thick oxidation layer in an area where the coating layer is poor and very nonuniform. Although the coating application was not optimized, a reduction in the loss due to *SO* was observed.

An experiment with various coatings was carried out. The Ni plating cannot tolerate 500°C temperature. The Ni plating peeled from the sample surface after several hours at 500°C. Aluminum ion vapor deposition (IVD) works very well for temperatures < 485°C. The maximum operating temperature for Al IVD is 485°C. An Al IVD-coated magnet type E has 3.8% loss due to surface oxidation. Other coatings are being evaluated.

Table 3-6. Flux Losses After Aging at 550°C for 360 Hours

| Magnet | T _M | Magnetic Loss (%) | | | | | | |
|------------------------|----------------|-------------------|------|-------|---------|-------|-------------------|-------------------|
| | | I. D. | (°C) | Total | SO & MC | NLC | SO | MC |
| A | 250 | -83.0 | | -20.3 | | -62.7 | -16* | -4.2** |
| B | 330 | -58.6 | | -19.5 | | -39.1 | -16* | -3.5** |
| C | 400 | -26.7 | | -19.0 | | -7.7 | -16* | -3.0** |
| D | 500 | -21.3 | | -17.7 | | -3.6 | -16* | -1.7** |
| E | 550 | -20.0 | | -17.9 | | -2.1 | -16* | -1.9** |
| Coated C ^{!!} | | -14.4 | | -6.7 | | -7.7 | -3.7 [⊗] | -3.0 [*] |
| Coated D ^{!!} | | -11.9 | | -7.7 | | -4.2 | -6.0 [⊗] | -1.7 [*] |
| Coated E ^{!!} | | -8.2 | | -6.6 | | -1.6 | -4.7 [⊗] | -1.9 [*] |
| E (Al-IVD) | | -6.7 | | -5.7 | | -1.0 | -3.8 | -1.9 |

* Calculated from the optical micrographs.

** MC - Loss due to metallurgical change = Permanent loss (SO & MC) - SO loss

• Data from above for magnets C, D, and E without coating.

⊗ SO - Loss due to surface oxidation = (SO & MC) loss - MC loss

!! Coated with high temperature ceramic adhesive

It is clear that for Sm-TM magnet applications up to 300°C, surface oxidation is not a factor. For applications up to 400°C, coating is recommended. At temperature $\geq 500^\circ\text{C}$, surface oxidation plays a major role. A coating is necessary for magnets used at this temperature if the application is not under vacuum or in an inert gas atmosphere. The MC loss is relatively small, especially for the magnets with higher T_M. It is observed that MC loss is only $< 2\%$ for magnets type D and E (T_M = 500 and 550°C) after 360 hours at 550°C. This work suggests that these high temperature magnets, properly coated, will be suitable for long-term service at high temperatures.

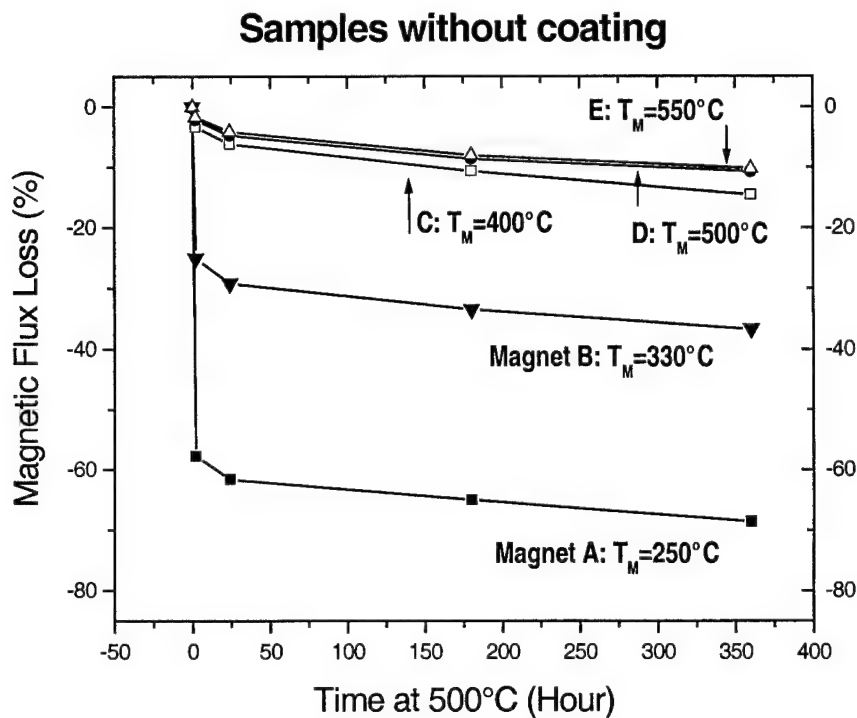


Figure. 3.21. Magnetic loss vs. aging time at 500°C for different types of uncoated magnets.

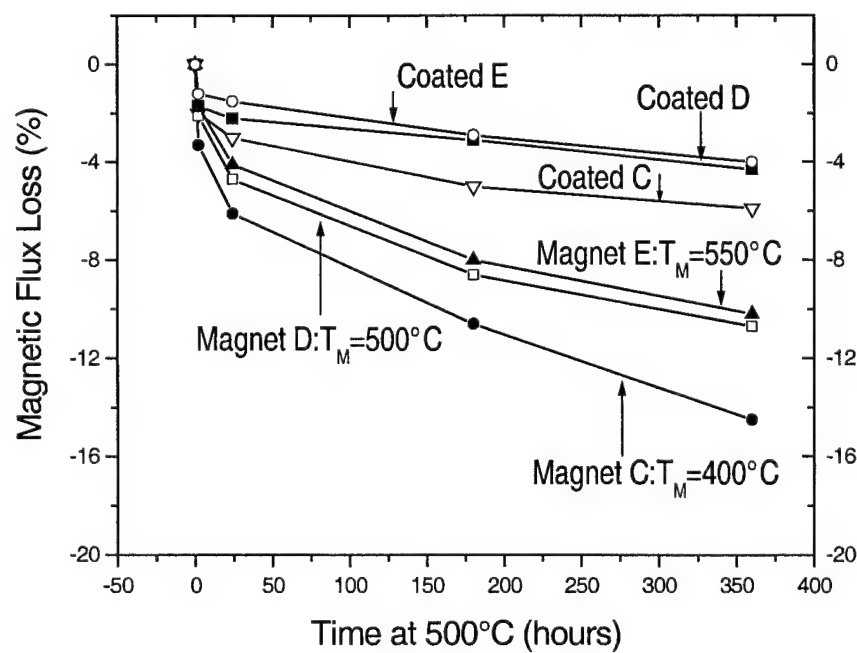


Figure 3.22. Magnetic loss vs. time at 500°C for high temperature magnets with and without coating.

3.5.5 Pinning Strength in Sm(Co,Fe,Cu,Zr)z Magnets

For 2:17 type magnets, magnetic hardening is achieved through the precipitation process. As J. Fidler described[37], the coherent precipitation of cell boundary phase and the cell interior phase determine the pinning of magnetic domain walls. Magnet types B ($T_M = 330^\circ\text{C}$) and E ($T_M = 550^\circ\text{C}$) were studied in this magnetic hardening experiment.

Figure 3.23 shows the intrinsic demagnetization curves for the magnet samples quenched from different indicated temperatures. The magnets were cooled down from sinter temperature at the rate of $50^\circ\text{C}/\text{minute}$, and from solid solution temperature at the rate of $100^\circ\text{C}/\text{minute}$. After sinter and solution heat treatment, the MH_c of type D magnet was ~ 1.5 kOe higher than type B. All the magnet samples were aged at 850°C for 10 hours. The temperature was then ramped down at the rate of $1^\circ\text{C}/\text{minute}$. Samples were quenched from each of the following temperatures: 850 , 700 , 600 , 500 , and 400°C . It was observed that the magnetic hardening was completed at 400°C for type B with $T_M = 330^\circ\text{C}$, and was completed at about 550°C for magnet type E with $T_M = 550^\circ\text{C}$. This can explain why the high temperature magnets are thermally stable at temperatures $\leq 550^\circ\text{C}$.

At 25°C , the applied field of the hysteresigraph (~ 26 kOe) cannot overcome the pinning strength of any of these alloys. Therefore, pulse magnetization is required to saturate these magnets at room temperature. However, at 300°C , a field of 26 kOe can actually saturate all of these alloys. The pinning field, H_p , is defined as the intersection of the tangents of two sections of an initial magnetization curve as shown in Figure 3.24, which indicates the behavior of pinning type magnets. Also shown is that at 300°C , the magnets with higher T_M have higher pinning field H_p than those with lower T_M . The values of H_p for different T_M are listed in Table 3-7. Higher H_p requires a higher magnetization field. With higher H_p at 300°C , the magnets have higher resistance to thermal demagnetization at $T \geq 300^\circ\text{C}$. For most permanent magnets, MH_c decreases as the temperature increases. The negative temperature coefficient of MH_c for these magnets is due to thermal agitation or thermal demagnetization. When temperature increases, thermal agitation increases, and domain walls move more easily. If a higher pinning strength exists in the magnet, the movement of the walls will be more difficult.

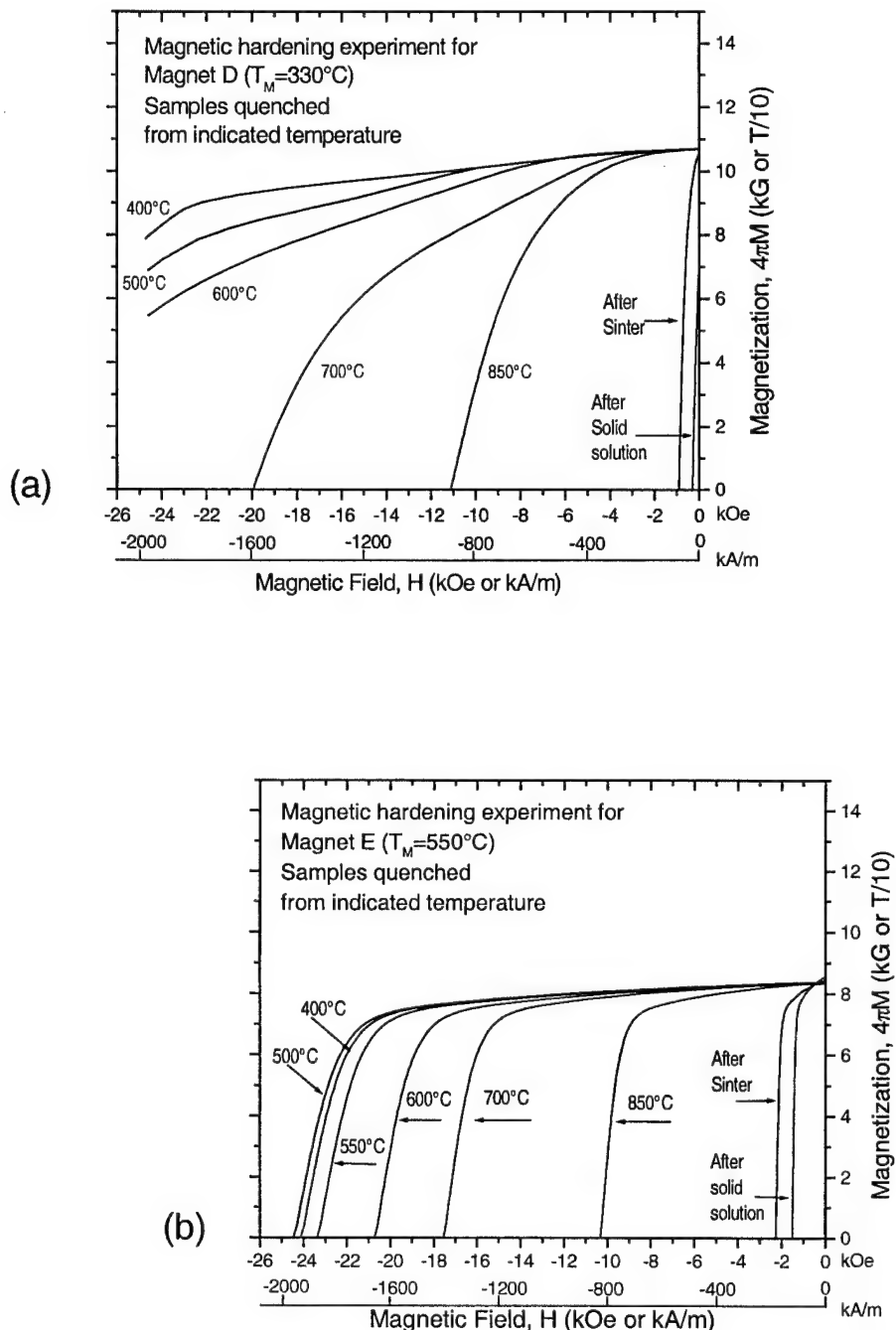


Figure 3.23. Intrinsic demagnetization curves for the magnetic hardening experiment.

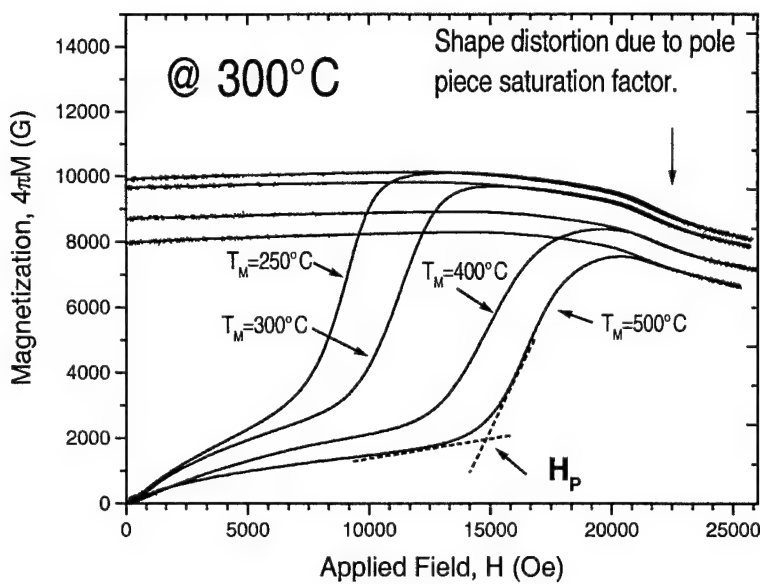


Figure 3.24. Initial magnetization curves for the magnets with different T_M .

Table 3-7. Pinning Field H_p at 300°C

| | $T_M = 250^\circ\text{C}$ | $T_M = 330^\circ\text{C}$ | $T_M = 400^\circ\text{C}$ | $T_M = 500^\circ\text{C}$ | $T_M = 550^\circ\text{C}$ |
|-------------|---------------------------|---------------------------|---------------------------|---------------------------|---------------------------|
| H_p (kOe) | 7.0 | 9.5 | 13.0 | 15.0 | 15.2 |

3.5.6 Microstructure and Crystal Structure

Figure 3.25 is a scanning electron microscopy (SEM) micrograph of $\text{Sm}(\text{Co}_{0.794}\text{Fe}_{0.1}\text{Cu}_{0.09}\text{Zr}_{0.026})_{7.0}$ after aging. The nominal z value of the magnet specimen is 6.46. In other words, the magnet specimen contains very high Sm. Under this condition, it still shows a uniform "one-phase" microstructure. It is easy to understand, from the phase equilibrium relationship in the binary Sm-Co phase diagram, that decreasing z value (or increasing Sm content) will result in more precipitation of the Sm-rich cell boundary phase. This will lead to either a finer cellular microstructure, or thicker cell boundary phase, or both, provided the precipitation has a fixed Sm content. Generally speaking, a finer cellular microstructure benefits coercivity development at high temperatures as reported in [5,10]. However, results presented in Figure 3.2 suggest

that for each temperature level there seems to exist an optimum dimension of the cellular microstructure. We believe, however, that the Sm- and Cu- rich cell boundary phase does not have a fixed composition, but has a compositional range depending on the original alloy composition and the heat treatment parameters. Therefore, the explanation of the effect of Sm content on high temperature coercivity shown in Figure 3.2 can be very complicated.

A transmission electron microscopy (TEM) micrograph given in Figure 3.26 shows a typical 2:17 cellular and platelet structure for magnet type D with $T_M = 500^\circ\text{C}$. For these high temperature 2:17 magnets, two major factors may contribute to the excellent performance at high temperatures. One is the high Co content, which results in higher T_C and higher anisotropy field [1,38]. As shown in Table 3-2, the magnets with higher T_M have higher Co contents. Both high T_C and high anisotropy field help to maintain magnetization.

The second factor is the high volume of cell boundaries in the microstructure, which results in an increased number of pinning sites. Also shown in Table 3-2 is that magnets with higher T_M have lower z (higher Sm) and higher x for Cu in the formula of $\text{Sm}(\text{Co}_w\text{Fe}_v\text{Cu}_x\text{Zr}_y)_z$. Higher concentrations of Cu and Sm atoms in the 2:17 phase enable the alloy to have more precipitating sites and form more 1:5 cell boundary phase. Figure 3.27 shows the TEM microstructures for magnet type B with $T_M = 330^\circ\text{C}$ and magnet type D with $T_M = 500^\circ\text{C}$. It was observed that the cell size for magnet type D is ~ 78 nm, and for magnet type B is ~ 123 nm. The cell size of magnet type D is about 37% smaller than that of magnet type B. By rough calculation, the volume of cell boundaries for magnet D is ~ 1.5 times that for magnet B. It is believed that a high volume of cell boundaries plays a role in the high resistance to thermal demagnetization. It is also believed that the cell of the microstructure maintains 2:17 stoichiometry even though the effective z is about 7.6 for magnets with $T_M > 500^\circ\text{C}$.

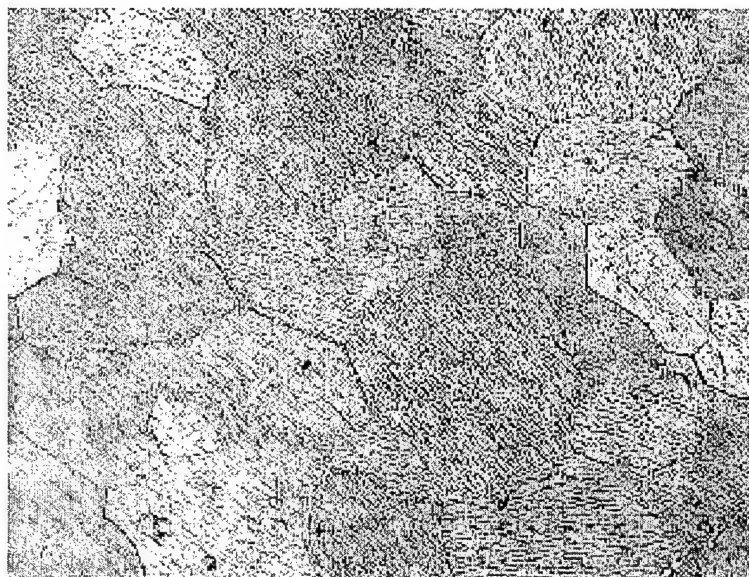


Figure 3.25. SEM micrograph of $\text{Sm}(\text{Co}_{0.794}\text{Fe}_{0.1}\text{Cu}_{0.09}\text{Zr}_{0.026})_{7.0}$ (Nominal $z = 6.46$).

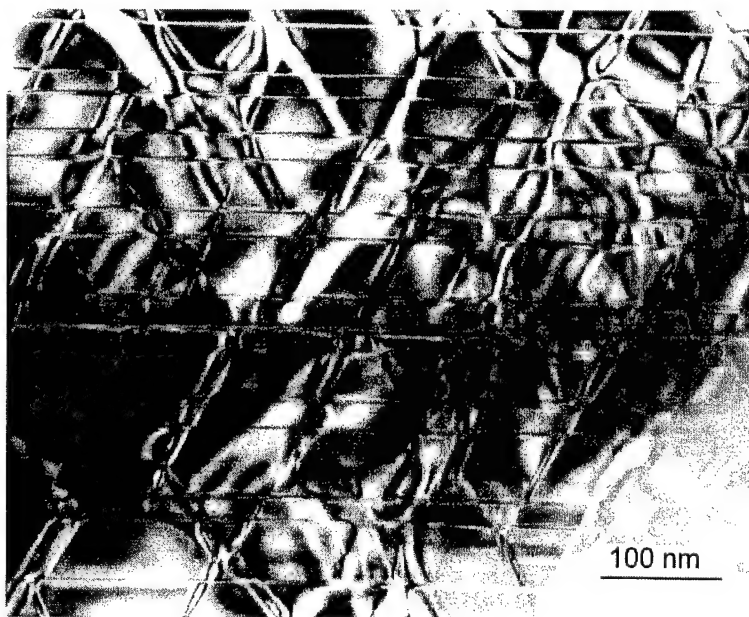


Figure 3.26. TEM microstructure for magnet D with $T_M = 500^\circ\text{C}$. (TEM work by Prof. J. Fidler of the University of Vienna, Austria.)

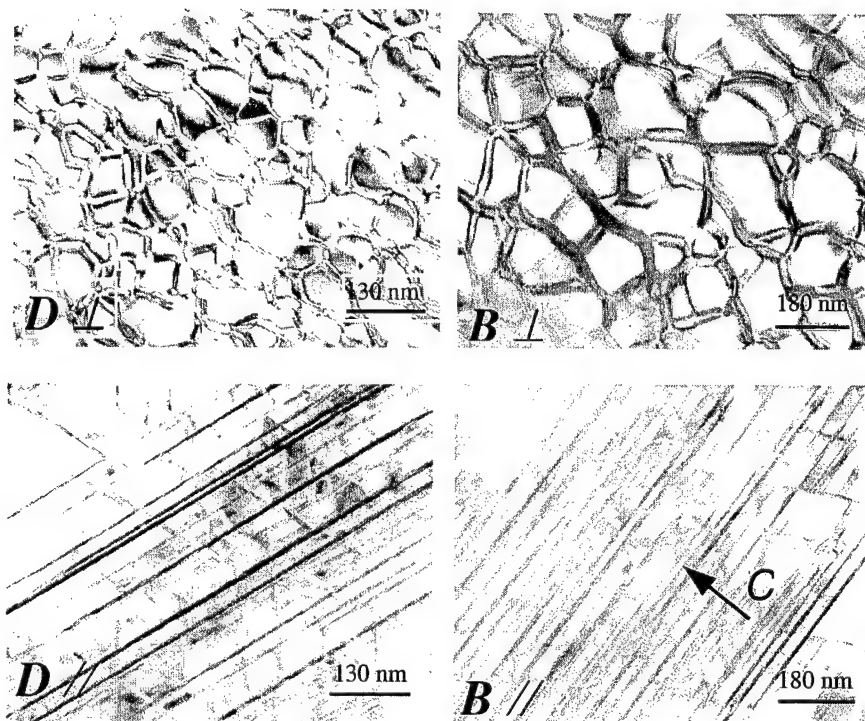


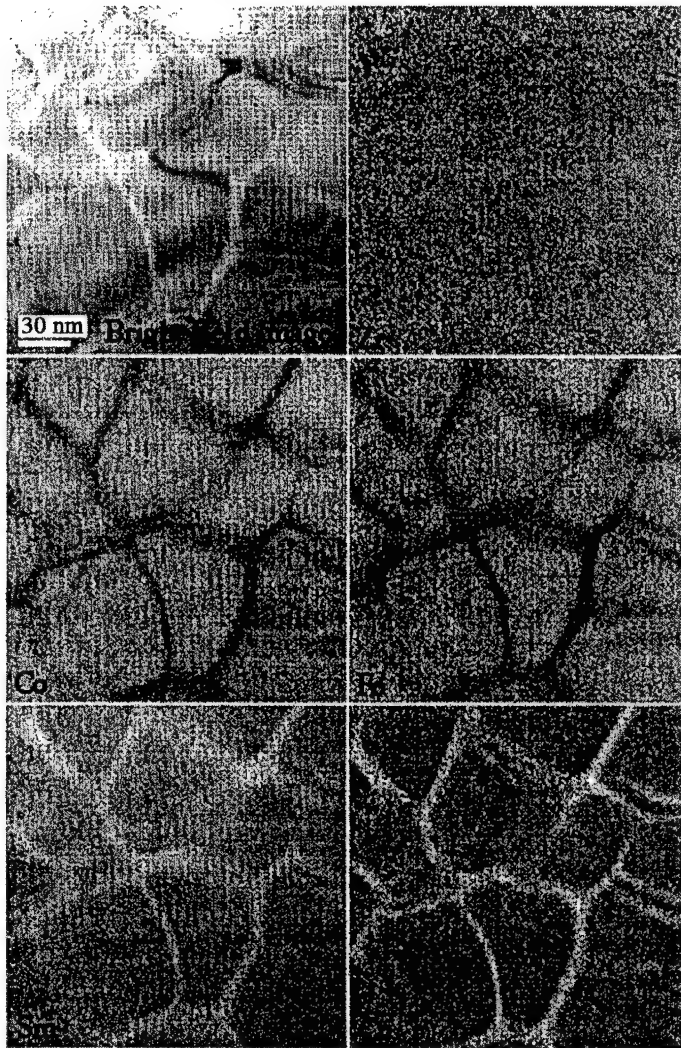
Figure 3.27. TEM microstructure for magnets D with $T_M = 500^\circ\text{C}$ and B with $T_M = 330^\circ\text{C}$.

Cell size is 78 nm for magnet D, and 123 nm for magnet B.

(By G. Hadjipanayis and Dr. Y. Zhang of University of Delaware, USA.)

Figure 3.28 shows a composition map for magnet type D with $T_M = 500^\circ\text{C}$. It is observed that Fe and Co atoms prefer to reside inside the cells. The amounts of Fe and Co along the cell boundaries are much less than that inside the cells. Zr seems to distribute uniformly in this crystal direction. (This direction is perpendicular to the easy axis, or the c-axis.) Cu atoms are mostly concentrated along the cell boundaries. Sm atoms are found in higher percentage along the cell boundaries than inside the cell. The maps illustrate that the 1:5 cell boundary phase contains mostly SmCu_5 .

Figure 3.29 is an XRD pattern of $\text{Sm}(\text{Co}_{0.794}\text{Fe}_{0.09}\text{Cu}_{0.09}\text{Zr}_{0.026})_{7.0}$ after solid solution heat treatment (SSHT). This figure shows that the magnet specimen is of 2:17 hexagonal crystal structure after SSHT. Figure 3.30 is an XRD pattern of $\text{Sm}(\text{Co}_{0.794}\text{Fe}_{0.09}\text{Cu}_{0.09}\text{Zr}_{0.026})_{7.0}$ after aging and in a high coercivity condition. The XRD result indicates that the magnet specimen consists of a 2:17 rhombohedral phase and a 1:5 hexagonal phase.



Composition map obtained by electron energy loss spectroscopy.

Figure 3.28. Composition map for magnet type D with $T_M = 500^\circ\text{C}$, which was obtained by using electron energy loss spectroscopy.

(By D. Sellmyer and Yi Liu of University of Nebraska, USA.)

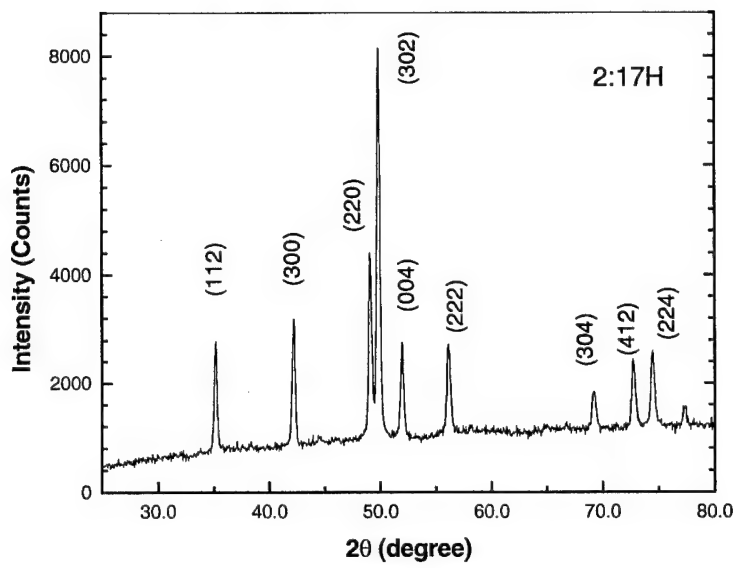


Figure 3.29. XRD pattern of $\text{Sm}(\text{Co}_{0.794}\text{Fe}_{0.09}\text{Cu}_{0.09}\text{Zr}_{0.026})_{7.0}$ after solid solution heat treatment.

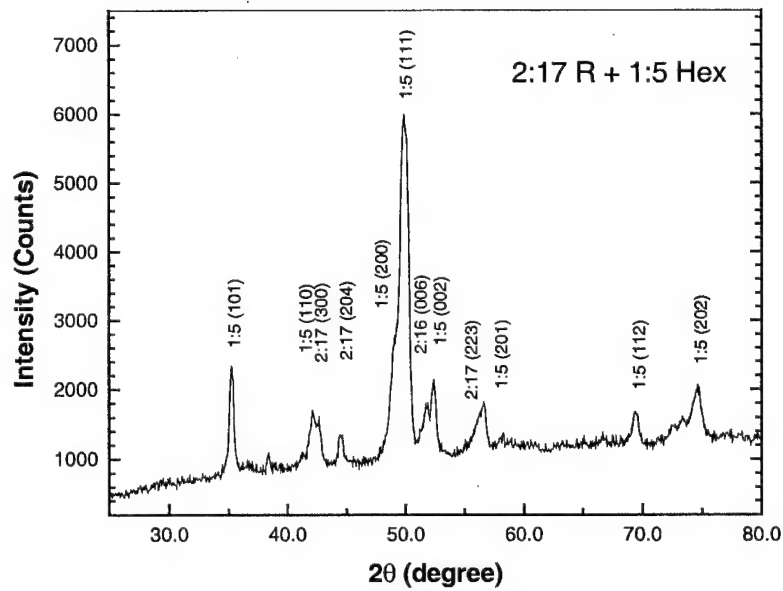


Figure 3.30. XRD pattern of $\text{Sm}(\text{Co}_{0.794}\text{Fe}_{0.09}\text{Cu}_{0.09}\text{Zr}_{0.026})_{7.0}$ after aging.

3.5.7 Novel Temperature Dependence of Intrinsic Coercivity and New Model of Coercivity Mechanism in $\text{Sm}(\text{Co},\text{Fe},\text{Cu},\text{Zr})_7$ Magnets

3.5.7.1 Novel Temperature Dependence of Intrinsic Coercivity

During the course of developing new high temperature permanent magnets, we observed a complex temperature dependence of $_{\text{M}}\text{H}_c$ in some newly-developed magnets as shown in Figure 3.31. Upon heating a new sintered magnet $\text{Sm}(\text{Co}_{\text{bal}}\text{Fe}_{0.04}\text{Cu}_{0.09}\text{Zr}_{0.027})_{7.26}$ (note: 7.26 is an effective ratio of transition metals to Sm; the nominal ratio is 6.60 when the oxygen content equals 0.4 wt%) that possesses high Sm and low Fe contents as compared with conventional 2:17 magnets, its $_{\text{M}}\text{H}_c$ first drops from a room temperature value of 5.1 kOe to 4.3 kOe at 150°C (Figure 3.31). The coercivity then rapidly increases at temperatures above 200°C and reaches a maximum of 7.6 kOe at 500°C. It should be noted that the $_{\text{M}}\text{H}_c$ of this magnet at 500°C is more than 30% higher than its room temperature coercivity value as shown in Figure 3.31. In addition, as shown in Figure 3.4, the intrinsic coercivity of $\text{Sm}(\text{Co}_{\text{bal}}\text{Fe}_{0.1}\text{Cu}_{0.05}\text{Zr}_{0.025})_{7.38}$ at 550°C is more than three times higher than its room temperature coercivity value!

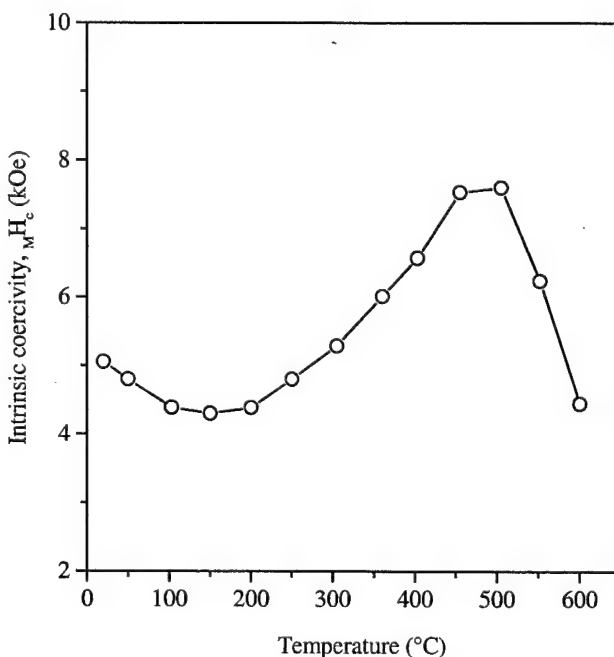


Figure 3.31. Temperature dependence of intrinsic coercivity of sintered $\text{Sm}(\text{Co}_{\text{bal}}\text{Fe}_{0.04}\text{Cu}_{0.09}\text{Zr}_{0.027})_{7.26}$ magnet.

The novel temperature dependencies of MH_c observed in the new high temperature magnets as shown in Figure 3.4 and Figure 3.31 are a challenge to previous coercivity theories. In these theories, the effect of temperature on coercivity is related only to basic magnetic parameters such as saturation magnetization and crystalline anisotropy and, thus, this novel temperature dependence of MH_c cannot be explained. Therefore, a new coercivity model is required which will lead to a better understanding of the nature of coercivity in rare earth permanent magnets.

3.5.7.2 Description of the New Model of Coercivity

Coercivity mechanisms in permanent magnets are very complicated and many factors affect the coercivity development. However, the complex temperature dependence of MH_c shown in Figure 3.31 clearly suggests that there must be two conflicting coercivity mechanisms that control the coercivity of the magnet. The first mechanism results in higher coercivity at higher temperature; the second mechanism leads to lower coercivity at high temperature. As a result of these two conflicting mechanisms, a more or less U shaped MH_c vs. T curve forms at 20 to 500°C.

Mechanism I – Higher MH_c at Higher Temperature: It is well known that the coercivity in 2:17 type magnets originates from domain wall pinning in a Sm- and Cu-rich 1:5 cell boundary phase of a fine-scaled cellular microstructure [39-43]. This is because the cell boundary phase has lower crystalline anisotropy constant K and, in turn, lower domain wall energy E than the 2:17 cell phase. The magnitude of coercivity is determined by the domain wall energy difference between the 1:5 and 2:17 phases. Therefore, higher coercivity at higher temperature implies that the energy difference between the two phases increases with increasing temperature.

The Sm- and Cu-rich 1:5 cell boundary phase has not only a lower crystalline anisotropy, but also a lower Curie temperature (T_C) than the 2:17 cell phase. Thus, the crystalline anisotropy of the 1:5 phase may decrease more rapidly than the 2:17 phase upon heating. This may result in the temperature dependencies of crystalline anisotropy of the 1:5 and 2:17 phases resembling the curves in Figure 3.32. It can be seen from Figure 3.32 that as temperature increases, the anisotropy difference between the two phases also increases. This leads to a higher MH_c at higher temperature.

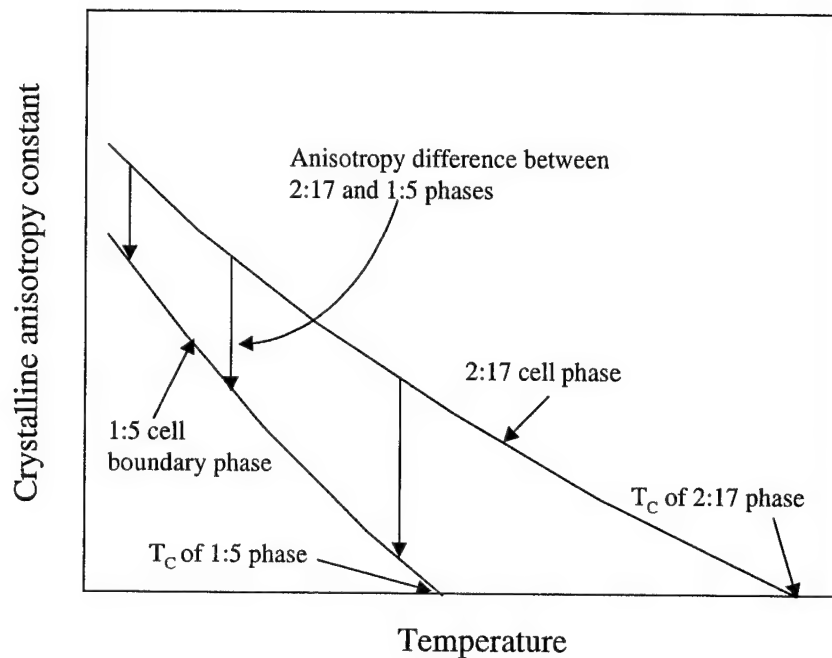


Figure 3.32. Schematic temperature dependence of crystalline anisotropy of 2:17 cell phase and 1:5 cell boundary phase.

Mechanism II – Lower MH_c at Higher Temperature: Since pinning is responsible for higher MH_c at higher temperature, the second coercivity mechanism that leads to lower MH_c at higher temperature has to be related to a process other than pinning. It is postulated that the second mechanism is closely related to a thermal activation process. This assumption is based on the experimental data obtained in 1981 [4] when we observed that the temperature dependence of a commercial 2:17 magnet could be exactly fitted to a simple exponential equation when the temperature was lower than 900 K, as shown in Figure 3.33. We believe that this was not an accident but revealed the nature of the coercivity mechanism in 2:17 type magnets.

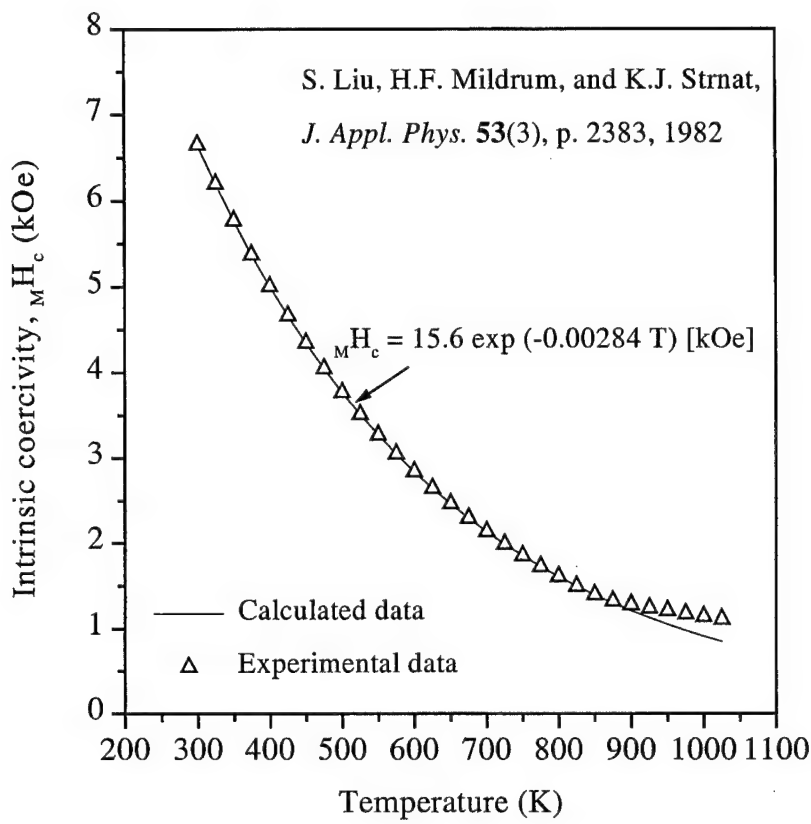


Figure 3.33. Temperature dependence of intrinsic coercivity of $\text{Sm}(\text{Co}_{0.81}\text{Fe}_{0.025}\text{Cu}_{0.14}\text{Mn}_{0.025})_{7.0}$.

As mentioned previously, coercivity in 2:17-type magnets originates from domain wall pinning in the 1:5 cell boundary phase of the cellular microstructure. In order for the domain walls to be broken away from the 1:5 cell boundary phase, they must obtain enough energy to overcome the energy barrier between the 1:5 and 2:17 phases, namely ΔE (Figure 3.34). This energy can be acquired not only from the applied magnetic field (magnetic energy), but also from the thermal energy. It is easy to understand that the higher the temperature, the higher the thermal energy will be, and the domain walls that are in a thermal excited condition would have more chance to climb up the energy barrier. Assuming that the probability ρ of a domain wall to climb up an energy barrier ΔE at temperature T follows the Arrhenius equation,

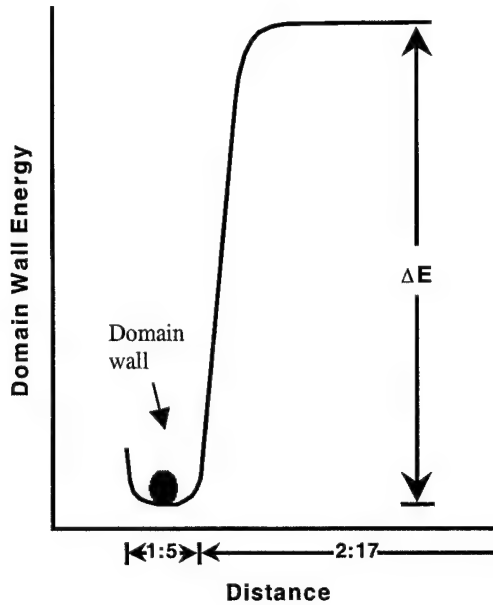


Figure 3.34. Energy barrier between the 2:17 cell phase and 1:5 cell boundary phase.

$$\rho = C \exp(-\Delta E / k_B T) \quad (3-4)$$

where C is a constant and k_B is the Boltzmann constant. Apparently, high ρ means low coercivity. Thus, the relationship between MH_c and temperature T can be expressed as:

$$MH_c = c \exp(\Delta E(T)/k_B T) \quad (3-5)$$

where, c is a constant, and the energy barrier is written as $\Delta E(T)$ to emphasize that it is a function of temperature. It is apparent that $\Delta E(T)$ is the domain wall energy difference between the 2:17 and 1:5 phases and it can be written as:

$$\Delta E(T) = E_{2:17} - E_{1:5} = C_1 \sqrt{A_{2:17} K_{2:17}} - C_2 \sqrt{A_{1:5} K_{1:5}} \quad (3-6)$$

where $A_{2:17}$ and $A_{1:5}$ are exchange constants; $K_{2:17}$ and $K_{1:5}$ are crystalline anisotropy constants for the 2:17 and 1:5 phases, respectively; and C_1 and C_2 are constants. Because the exchange constant A of a ferromagnetic material is a function of its Curie temperature, T_C , it can be written as:

$$A = c k_B T_C \quad (3-7)$$

where k_B is the Boltzmann constant and c is a constant. Substituting Equation (3-7) into Equation (3-6) and redefining the constants gives:

$$\Delta E(T) = c_1 \sqrt{k_B(T_C)_{2:17} K_{2:17}} - c_2 \sqrt{k_B(T_C)_{1:5} K_{1:5}} . \quad (3-8)$$

Substituting Equation (3-8) into Equation (3-5), and considering that K is a function of T , we have

$$M H_c = c \exp\left(\frac{c_1 \sqrt{k_B(T_C)_{2:17} K(T)_{2:17}} - c_2 \sqrt{k_B(T_C)_{1:5} K(T)_{1:5}}}{k_B T}\right). \quad (3-9)$$

In a phenomenological sense, many transition phenomena affected by temperature follow the Arrhenius equation. Examples include (1) transition of electrons from a metal to a lightly doped semiconductor (a sub-atomic scale transition); (2) diffusion of atoms (an atomic scale transition); (3) transition of a dislocation in crystals (a transition of an object with two dimensions in atomic scale); (4) transition of grain boundary (a transition of an object with one dimension on an atomic scale). The domain wall transition is, in a sense, like the transition of grain boundary. In both cases, the objects of the transition have only one dimension on an atomic scale. However, when a domain wall moves, atoms do not actually move. What moves is only a narrow region in which the direction of magnetic moment is different from its neighbors. This is an important difference between a domain wall and other objects that follow the Arrhenius equation. In addition, under a constant applied magnetic field, the thermal energy would play a critical role in domain wall transition and the time-dependent effect occurs. This is the nature of magnetic viscosity phenomena.

3.5.7.3 Explanation of Various Temperature Dependencies of Coercivity Using the New Model

According to this model, by modifying the compositions of the 1:5 cell boundary phase and the 2:17 cell phase, various temperature dependencies of the exponential $\Delta E(T)/k_B T$ can be obtained. There are six different possibilities:

(1) With increasing temperature, $\Delta E(T)$ decreases. In this case, $\Delta E/k_B T$ decreases rapidly with temperature, which results in a large negative temperature coefficient of MH_c , as observed in conventional 2:17 magnets (Figure 3.8, magnet 1);

(2) With increasing temperature, $\Delta E(T)$ increases at a smaller rate than T. In this case, $\Delta E(T)/k_B T$ decreases slowly with temperature, which results in a small negative temperature coefficient of MH_c , as observed in some newly-developed high temperature magnets (Figure 3.8, magnets 2, 3,4);

(3) With increasing temperature, $\Delta E(T)$ increases at the same rate as T. In this case, $\Delta E(T)/k_B T$ is virtually a constant and independent of T, which results in a temperature-independent MH_c , as observed in some newly-developed high temperature magnets (Figure 3.8, magnet 5);

(4) With increasing temperature, $\Delta E(T)$ remains the same and is independent of T, which results in a typical exponential relationship between MH_c and T;

(5) With increasing temperature, $\Delta E(T)$ increases at a larger rate than T. In this case, $\Delta E(T)/k_B T$ increases with temperature, which results in a positive temperature coefficient of MH_c ;

(6) $\Delta E(T)$ changes differently with temperature at different temperature ranges, which results in a complex temperature dependence of coercivity as observed in some newly developed high temperature magnets (Figure 3.31).

As mentioned previously, coercivity mechanisms in permanent magnets are very complex and many factors affect the coercivity development. We believe that Equation (3-9) reveals the primary nature of coercivity mechanisms in 2:17 permanent magnets. Other factors that influence the coercivity, such as the geometry of the cellular structure and the width of the 1:5 cell boundary phase, can be attributed to a modification of the constant c or an addition of a secondary term in Equation (3-9).

3.5.7.4 Calculations of Temperature Dependence of MH_c Using the Proposed Model

We calculated temperature dependence of MH_c using Equation (3-9). We assumed three $\Delta E(T)$ cases. In each case, the calculated result is surprisingly similar to the observed experimental result.

Case I: $\Delta E(T)$ decreases with T. The assumed temperature dependence of crystalline anisotropy constants of the 2:17 cell phase and the 1:5 cell boundary phase is shown in Figure 3.35. The calculated result is shown in Figure 3.36. This case results in a large negative temperature coefficient, as observed in conventional 2:17 magnets (Figure 3.8, magnet 1);

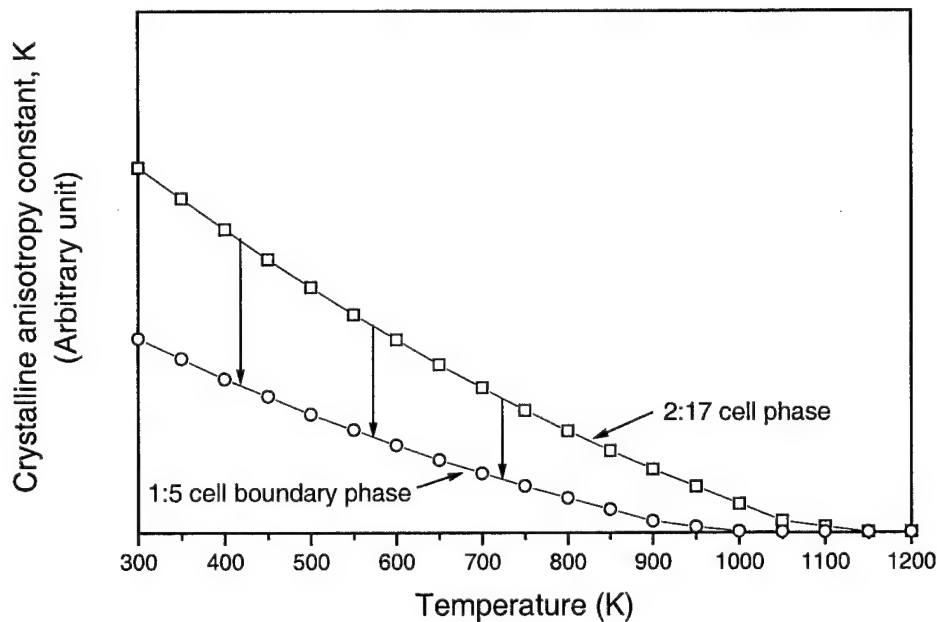


Figure 3.35. Assumed temperature dependence of crystalline anisotropy constant for 2:17 cell phase and 1:5 cell boundary phase. Case I, $\Delta E(T)$ decreases with T.

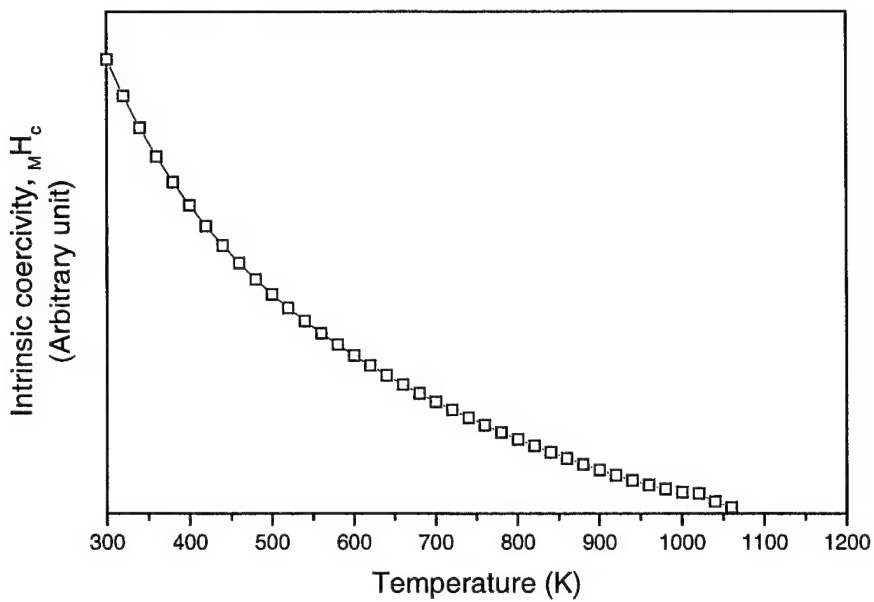


Figure 3.36. Calculated temperature dependence of mH_c . Case I, $\Delta E(T)$ decreases with T.

Case II: $\Delta E(T)$ increases with T. The assumed temperature dependence of crystalline anisotropy constants of the 2:17 cell phase and the 1:5 cell boundary phase is shown in Figure 3.37. The calculated result is shown in Figure 3.38. This case results in a small negative temperature coefficient, as observed in some newly-developed high temperature 2:17 magnets (Figure 3.8, magnet 4);

Case III: $\Delta E(T)$ increases rapidly with T at high temperature range (500 to 800 K). The assumed temperature dependence of crystalline anisotropy constants of the 2:17 cell phase and the 1:5 cell boundary phase is shown in Figure 3.39. The calculated result is shown in Figure 3.40. This case results in complex temperature dependence, as observed in some newly-developed high temperature 2:17 magnets (Figure 3.31).

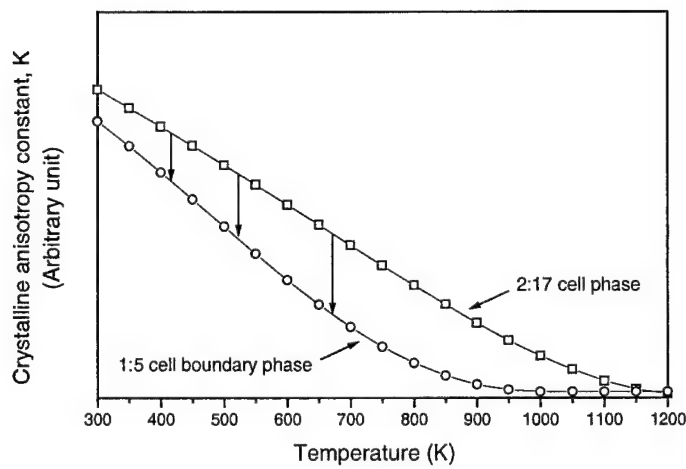


Figure 3.37. Assumed temperature dependence of crystalline anisotropy constant for 2:17 cell phase and 1:5 cell boundary phase. Case II, $\Delta E(T)$ increases with T.

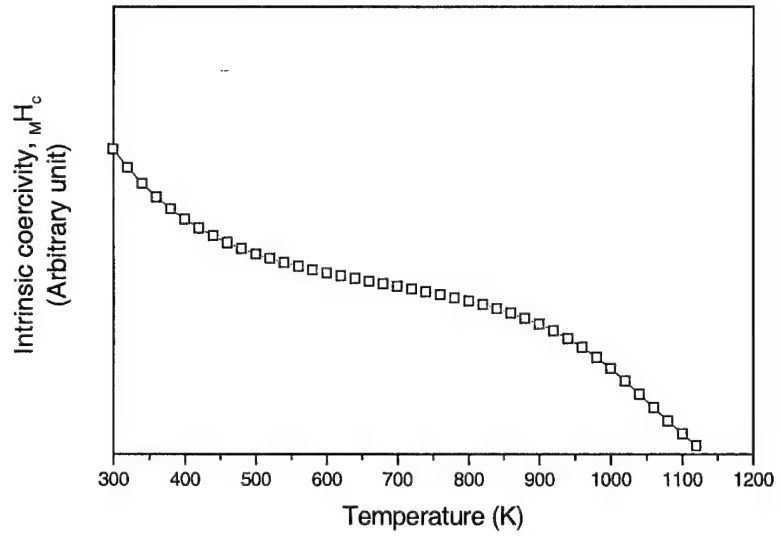


Figure 3.38. Calculated temperature dependence of M_Hc . Case II, $\Delta E(T)$ increases with T.

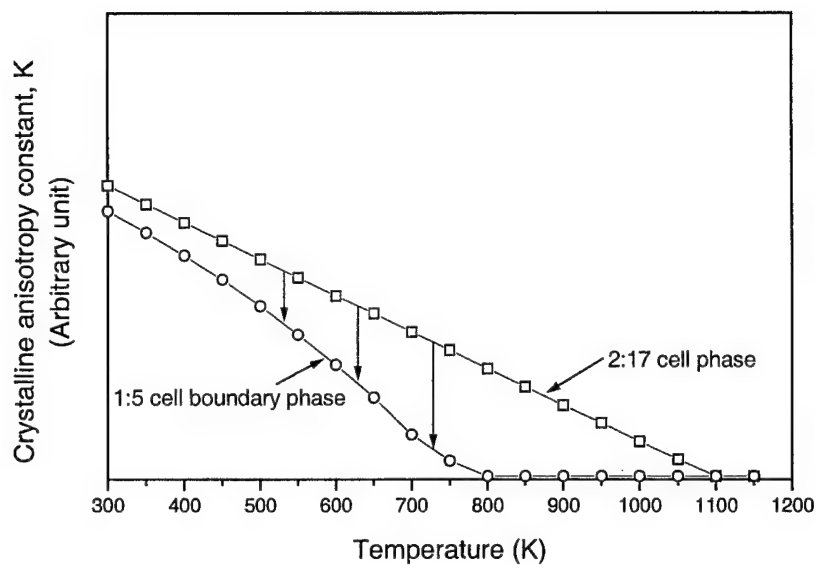


Figure 3.39. Assumed temperature dependence of crystalline anisotropy constant for 2:17 cell phase and 1:5 cell boundary phase. Case III, $\Delta E(T)$ increases rapidly with T .

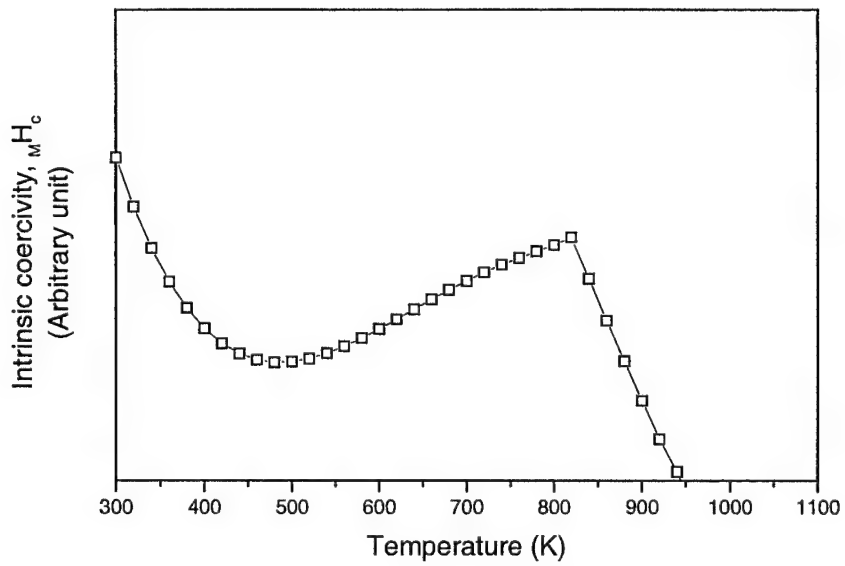


Figure 3.40. Calculated temperature dependence of MH_c . Case III, $\Delta E(T)$ increases rapidly with T .

3.5.7.5 Discussion on the Model

The basis of this new model lies in the argument that there are two conflicting mechanisms that control the coercivity in 2:17 magnets. One mechanism is related to the domain wall energy difference $\Delta E(T)$, which results in either decreased or increased coercivity with increasing temperature T . Another mechanism is related to the thermal energy $k_B T$, which leads to decreased coercivity with increasing temperature T . Only the coercivity model that incorporates these two conflicting mechanisms can explain the novel temperature dependence of intrinsic coercivity observed in the new magnets. Equation (3-6) was derived assuming that the transition of domain walls, which is affected by the thermal energy, observes the Arrhenius equation. This is only one of a few possibilities and is to be confirmed by experiment. Another possibility is that MH_c is related to the exponential of $(\Delta E(T) - k_B T)$ rather than $(\Delta E(T) / k_B T)$:

$$MH_c = c \exp(\Delta E(T) - k_B T). \quad (3-10)$$

Formally, Equation (3-10) is more similar to the equation given in Figure 3-33 than Equation (3-9). Equation (3-10) can also explain the novel temperature dependence of the new magnets. The exact equation of coercivity as a function of $\Delta E(T)$ and $k_B T$ can be determined only by further studies and experiments.

3.5.7.6 Applications of the New Coercivity Model

It is clear from above discussions that this new model of coercivity can satisfactorily explain not only the abnormal temperature dependence of MH_c shown in Figures 3.4 and 3.31, but also the temperature dependence of MH_c in conventional 2:17 magnets. This is because the two conflicting mechanisms exist not only in magnets with an abnormal temperature dependence of MH_c but in all 2:17 type permanent magnets. For conventional 2:17 magnets the pinning mechanism is relatively weak at high temperatures and the thermal activation mechanism dominates over the entire temperature range. However, in the newly developed magnets, the pinning mechanism is so strong at high temperatures that the magnets demonstrate small negative or even positive temperature coefficients of MH_c .

Further, we strongly believe that this thermal activation-pinning model also applies to most magnets that are controlled by crystalline anisotropy, including magnets that previously have been called nucleation type magnets such as sintered Nd-Fe-B and SmCo₅ magnets. During the demagnetization process in the Nd-Fe-B and SmCo₅ magnets, as well as in 2:17 type magnets, there certainly exists a nucleation process at the beginning of the demagnetization process, provided the magnet was fully magnetized to saturation prior to the demagnetization. However, it is not the nucleation field but the pinning field that determines the intrinsic coercivity in most cases. For example, it has been experimentally observed that the pinning of domain walls at the grain boundary Nd-rich phase plays a critical role for coercivity development in Nd-Fe-B magnets. It has also been experimentally observed that the pinning of domain walls at the grain boundary and/or at the minor Sm₂Co₇ phase appeared at the grain boundary plays an important role for coercivity development in SmCo₅ magnets. The difference is only that in 2:17 magnets the pinning sites are fine-scaled and dispersed, while in Nd-Fe-B and SmCo₅ magnets the pinning sites are localized and closely related to grain boundaries. The magnets to which this model does not apply are magnets controlled by shape anisotropy such as Alnico and magnets controlled by stress and/or nonferromagnetic inclusions such as the old steel magnets.

3.6 New Sintered Rare Earth Permanent Magnets Based on SmCo₇ Phase

3.6.1 X-ray Diffraction Result and Microstructure

The XRD data of Sm(Co_{0.6}Fe_{0.15}Cu_{0.085}Ti_{0.043})_{6.4} can be fitted to a 1:7 hexagonal crystal structure as shown in Figure 3.41 and Table 3-8. It can be seen from Table 3-7 that with increasing Fe content the c-axis is expanded. A SEM micrograph of Sm(Co_{0.6}Fe_{0.15}Cu_{0.085}Ti_{0.043})_{6.4} is shown in Figure 3.42. It is apparent that the microstructure is basically a single phase with a few inclusions.

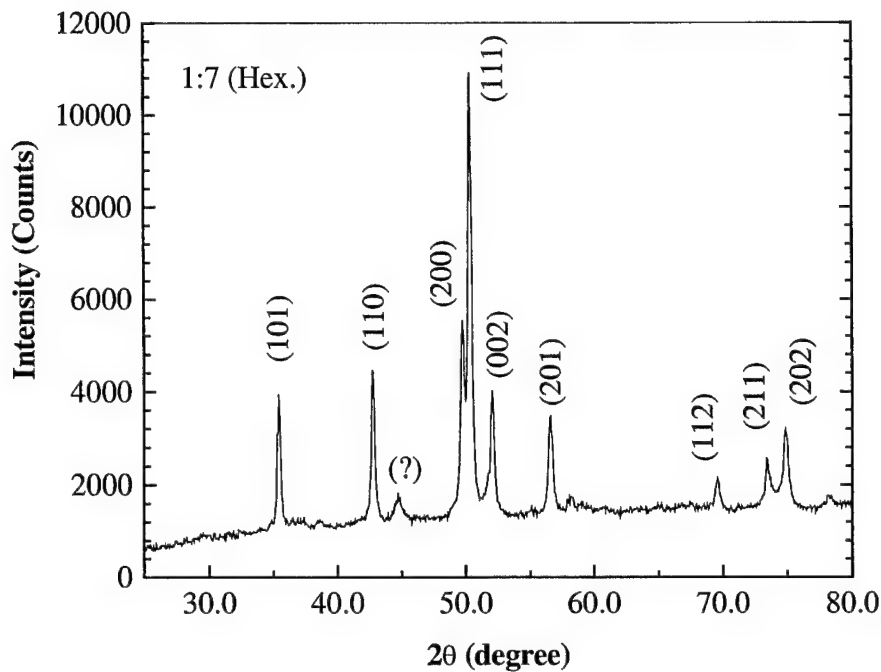


Figure 3.41. X-ray diffraction pattern of $\text{Sm}(\text{Co}_{\text{bal}}\text{Cu}_{0.085}\text{Ti}_{0.043})_{6.4}$.

Table 3-8. XRD Data for $\text{Sm}(\text{Co}_{\text{bal}}\text{Fe}_v\text{Cu}_{0.085}\text{Ti}_{0.043})_{6.4}$

| v | Structure | a (Å) | c (Å) | v (Å ³) |
|------|------------|--------|--------|---------------------|
| 0 | 1:7 (Hex.) | 4.9116 | 4.0754 | 85.1427 |
| 0.05 | 1:7 (Hex.) | 4.9137 | 4.0897 | 85.5400 |
| 0.09 | 1:7 (Hex.) | 4.9076 | 4.0908 | 85.3268 |
| 0.10 | 1:7 (Hex.) | 4.9118 | 4.0954 | 85.5662 |
| 0.15 | 1:7 (Hex.) | 4.9108 | 4.1077 | 85.1889 |

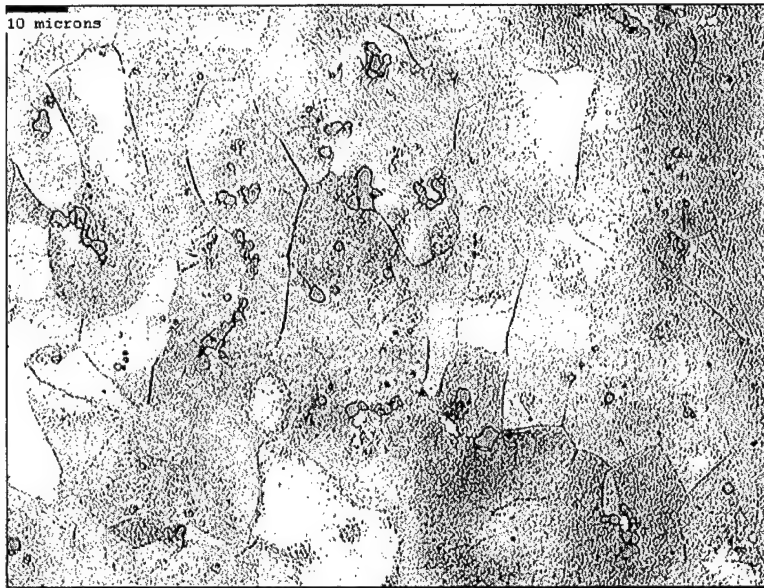


Figure 3.42. SEM micrograph of $\text{Sm}(\text{Co}_{\text{bal}}\text{Fe}_{0.15}\text{Cu}_{0.085}\text{Ti}_{0.043})_{6.4}$.

3.6.2 Effects of Compositions on Magnetic Properties

Figure 3.43 shows the effect of Fe substitution for Co on magnetic properties of $\text{Sm}(\text{Co}_{\text{bal}}\text{Fe}_v\text{Cu}_{0.085}\text{Ti}_{0.043})_{6.4}$. It can be seen from Figure 3.43 that the Fe substitution for Co enhances B_r . When v is increased from 0 to 0.043, MH_c drops. Further increasing v to 0.15 results in slightly increased MH_c . As shown in Figure 3.44, Cu effectively increases MH_c up to $x = 0.14$, but decreases B_r . Magnetic properties of $\text{Sm}(\text{Co}_{\text{bal}}\text{Cu}_{0.085}\text{Ti}_y)_{6.4}$ are sensitive to Ti content, y , as can be seen from Figure 3.45. When increasing y , B_r decreases monotonously as was expected. However, there appears a sharp peak in coercivity when $y = 0.04$. It can be concluded from Figure 3.46 that magnetic properties of $\text{Sm}(\text{Co}_{\text{bal}}\text{Cu}_{0.085}\text{Ti}_{0.043})_z$ are not very sensitive to z value. Figure 3.47 illustrates demagnetization curves of $\text{Sm}(\text{Co}_{0.957}\text{Ti}_{0.043})_{6.4}$. The intrinsic coercivity in this Cu-free magnet sample is 1.8 kOe. Adding Cu increases coercivity, but decreases remanence, as can be seen from demagnetization curves of $\text{Sm}(\text{Co}_{0.872}\text{Cu}_{0.085}\text{Ti}_{0.043})_{6.4}$ shown in Figure 3.48. Another magnet specimen of $\text{Sm}(\text{Co}_{0.875}\text{Cu}_{0.085}\text{Ti}_{0.04})_{6.4}$ displays much higher intrinsic coercivity of 4.5 kOe (Figure 3.49). It is anticipated that better magnetic performance can be achieved by optimizing compositions and heat treatment conditions.

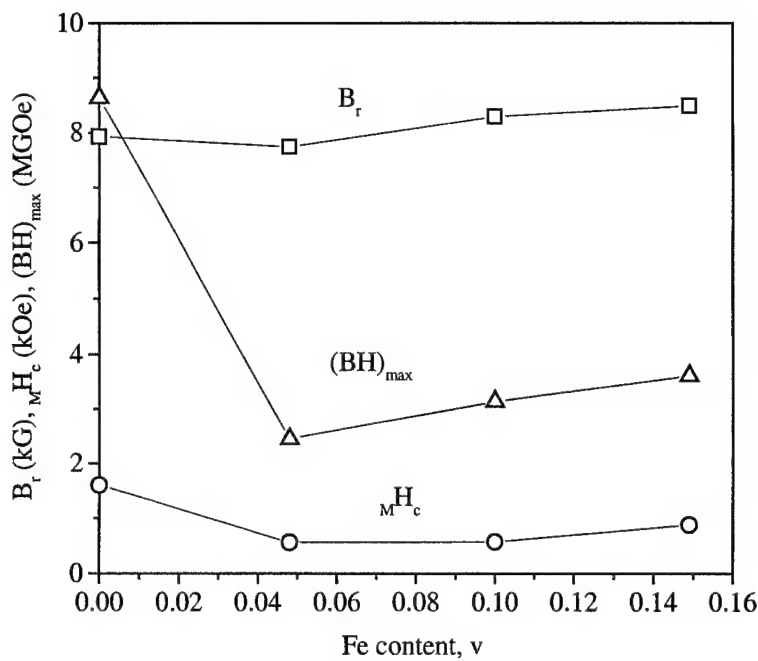


Figure 3.43. Magnetic properties vs. Fe content, v , in $\text{Sm}(\text{Co}_{\text{bal}}\text{Fe}_v\text{Cu}_{0.085}\text{Ti}_{0.043})_{6.4}$.

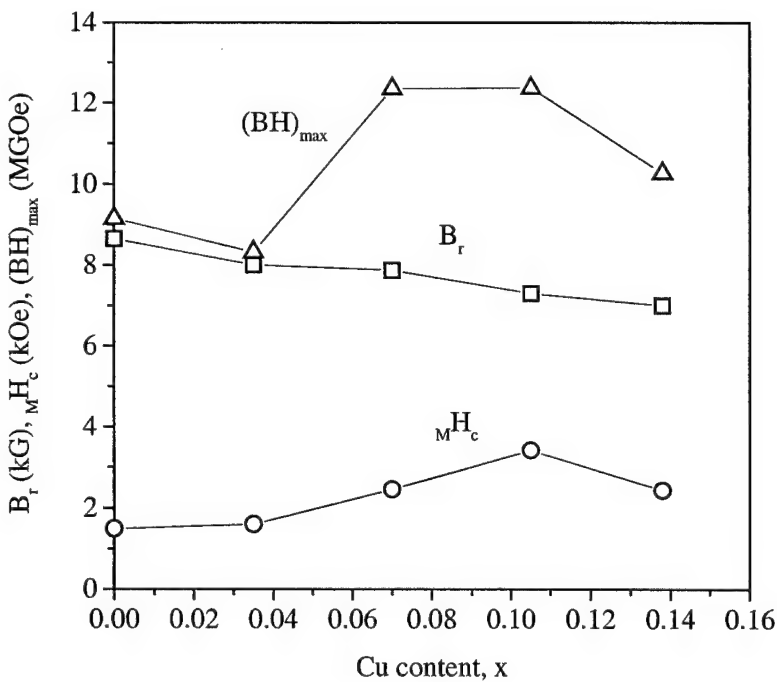


Figure 3.44. Magnetic properties vs. Cu content, x , in $\text{Sm}(\text{Co}_{\text{bal}}\text{Cu}_x\text{Ti}_{0.043})_{6.4}$.

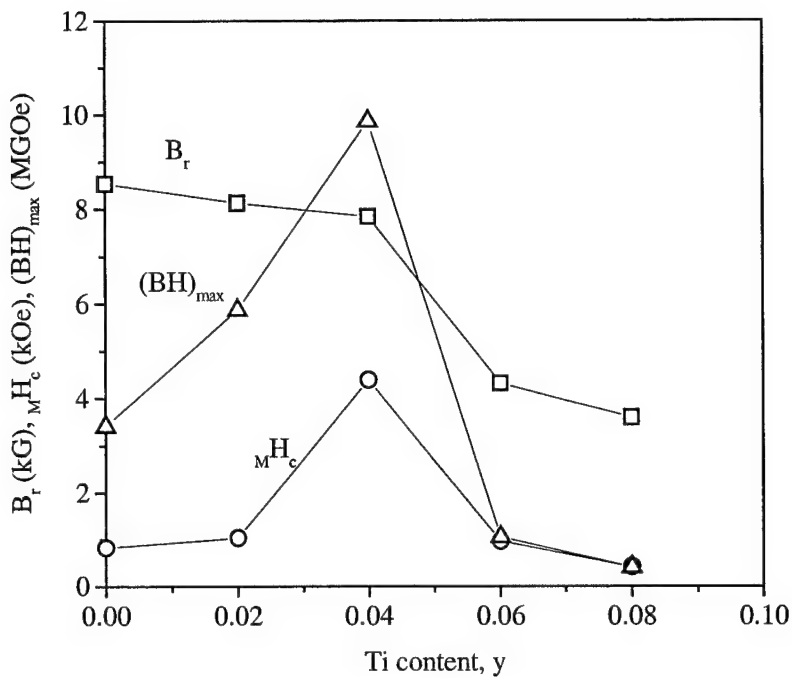


Figure 3.45. Magnetic properties vs. Ti content, y , in $\text{Sm}(\text{Co}_{\text{bal}}\text{Cu}_{0.085}\text{Ti}_y)_{6.4}$.

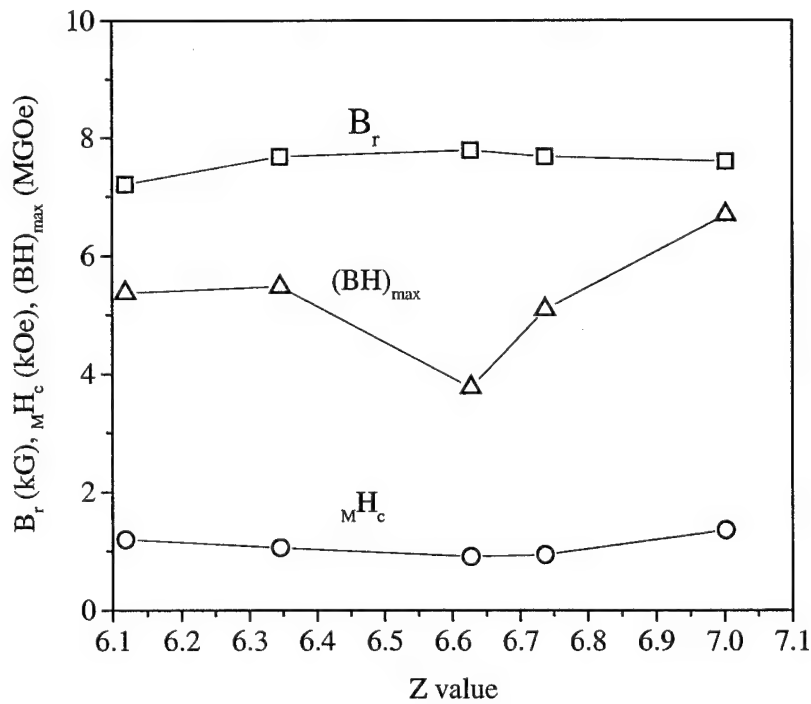


Figure 3.46. Magnetic properties vs. z value in $\text{Sm}(\text{Co}_{\text{bal}}\text{Cu}_{0.085}\text{Ti}_{0.043})_z$.

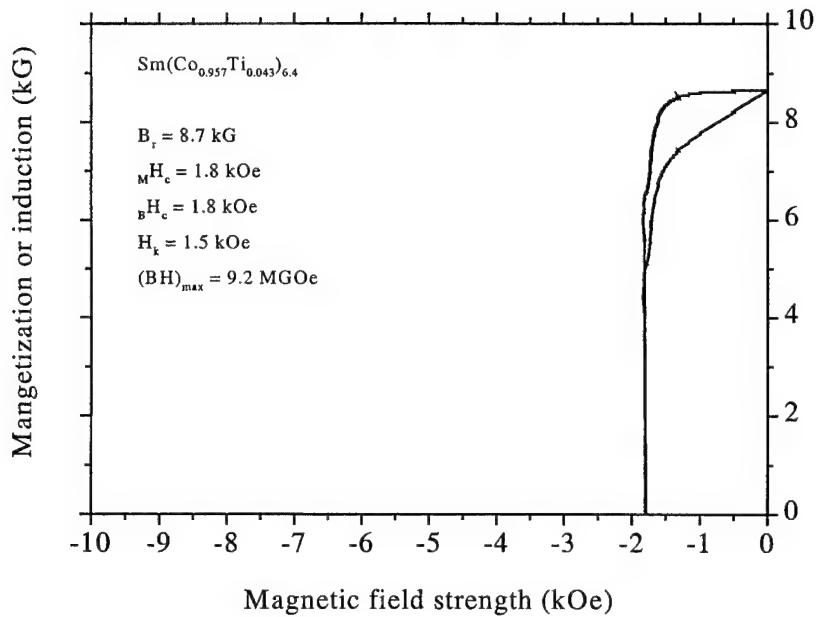


Figure 3.47. Demagnetization curves of $\text{Sm}(\text{Co}_{0.957}\text{Ti}_{0.043})_{6.4}$.

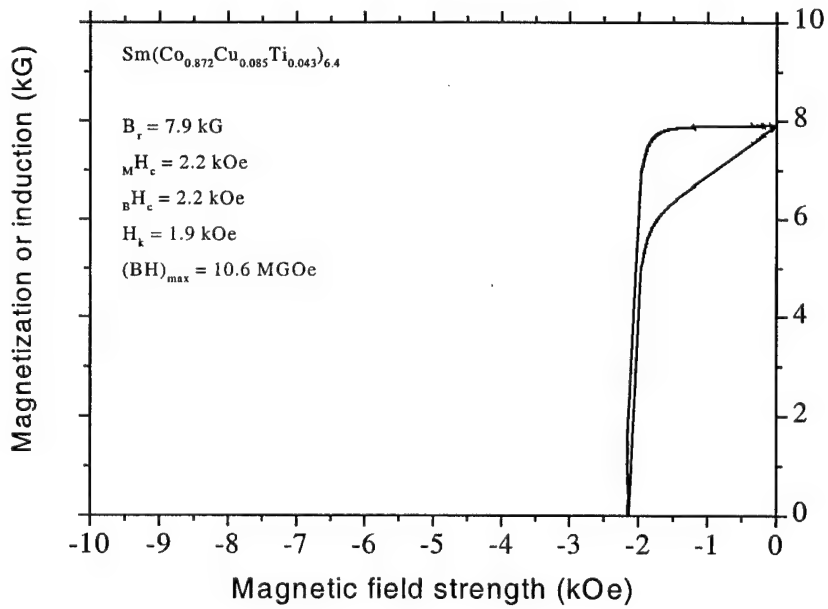


Figure 3.48. Demagnetization curves of $\text{Sm}(\text{Co}_{0.872}\text{Cu}_{0.085}\text{Ti}_{0.043})_{6.4}$.

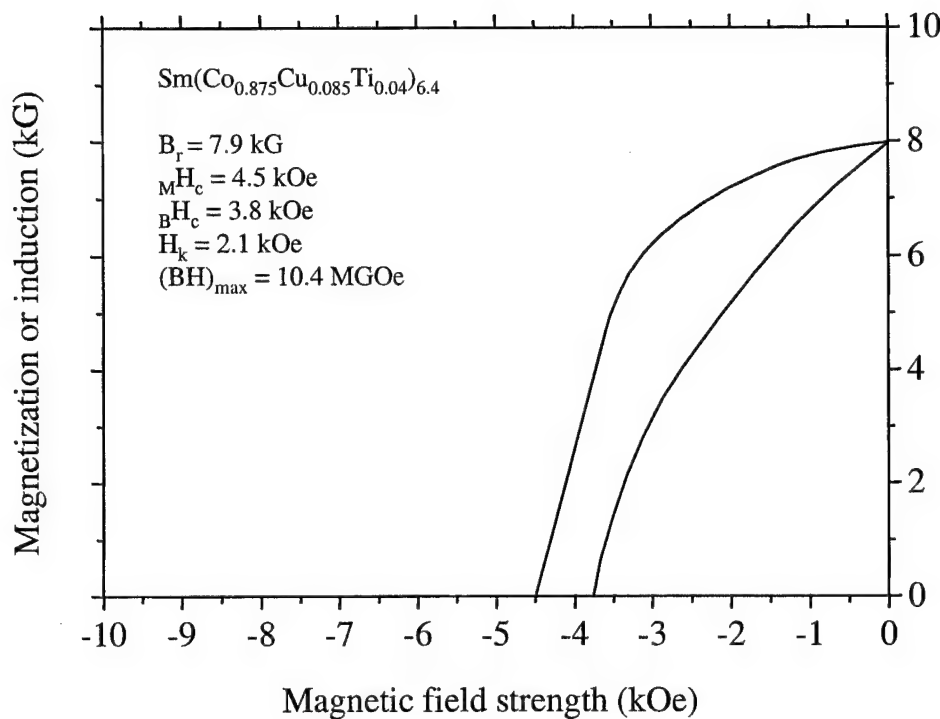


Figure 3.49. Demagnetization curves of $\text{Sm}(\text{Co}_{0.875}\text{Cu}_{0.085}\text{Ti}_{0.04})_{6.4}$.

3.7 Temperature-Compensated Rare Earth Permanent Magnets

3.7.1 A New Approach for Calculating Temperature Coefficient

A new approach for calculating the temperature coefficient, α_T , of magnetic parameters was developed in order to more accurately describe the high temperature characteristics of magnetic materials. Using this new approach, the “true” (or instantaneous) α_T of any magnetic parameter at a specific temperature can be determined and a plot of α_T vs. temperature can be obtained. This new type of plot is a very useful tool for presenting temperature characteristics of a magnetic parameter.

The most commonly used parameter for temperature dependence of magnetic properties is α_T . The α_T of a magnetic parameter Q over a temperature interval between T_1 and T_2 is defined as:

$$\alpha_{(T_1 \rightarrow T_2)} = \frac{Q_{T_2} - Q_{T_1}}{Q_{T_1}(T_2 - T_1)} \times 100 [\%/\text{°C}]. \quad (3-11)$$

The α of Q at a specific temperature T is defined as:

$$\alpha_T(\Delta T=0) = \frac{\Delta Q}{Q \Delta T} \times 100 [\%/\text{°C}]. \quad (3-12)$$

It is obvious that $\alpha_{(T_1 \rightarrow T_2)}$ is an average of α of Q over the temperature interval $T_1 \rightarrow T_2$. However, $\alpha_{(T_1 \rightarrow T_2)}$ is not necessarily an accurate description of the temperature dependence of Q , especially when the interval between T_1 and T_2 is large. Further, when Q is not a monotonous function of temperature T , Equation (3-11) may give a misleading result. On the other hand, α_T gives the “true” α of Q at a specific temperature T . It is the instantaneous α and is a more accurate description of the temperature dependence of Q . Unfortunately, in practice, it is impossible to calculate α_T when $\Delta T=0$ by simply using Equation (3-12).

The above-mentioned problem can be readily resolved if we use a polynomial to represent Q ,

$$Q(T) = a_0 + a_1 T + a_2 T^2 + \dots + a_n T^n = \sum_{i=0}^n a_i T^i, \quad (3-13)$$

and redefine the α of Q at T as:

$$\alpha_T = \frac{dQ}{dT} \times \frac{1}{Q} \times 100 [\%/\text{°C}]. \quad (3-14)$$

Coefficients $a_0, a_1, a_2, \dots, a_n$ in Equation (3-13) can be determined using a least squares fit. Calculating the derivative of this polynomial yields

$$\frac{dQ}{dT} = a_1 + 2a_2 T + \dots + n a_n T^{n-1} = \sum_{i=1}^n i a_i T^{i-1}. \quad (3-15)$$

Substituting Equations (3-13) and (3-15) into Equation (13-4), we have

$$\alpha_T = \sum_{i=1}^n i a_i T^{i-1} / \sum_{i=0}^n a_i T^i \times 100 [\%/\text{°C}]. \quad (3-16)$$

Using Equation (3-16), the “true” instantaneous α_T of any magnetic parameter Q at any temperature T can be readily determined and a plot of α_T vs. T can be drawn. Normally, since α_T is more sensitive to T than Q , the α_T vs. T plot is a very useful tool to represent temperature characteristics of a magnetic parameter. The average α $\alpha_{(T_1 \rightarrow T_2)}$ can be also calculated using Equation (3-13). The calculated results are very close to those determined by more conventional methods.

As an example, Figure 3.50 shows the temperature dependence of magnetization at 10 kOe of a commercial sintered $\text{Gd}_2(\text{Co,Fe,Cu,Zr})_{17}$ magnet. Prior to the measurement, the specimen was magnetized using a 100 kOe pulse field. In Figure 3.50, the squares represent the experimental data, while the curve is a 6th degree polynomial fit. In any experimental characterization, random errors are always associated with the results of measurements. A least squares fit eliminates those random errors and therefore is generally a better representation than the original experimental data.

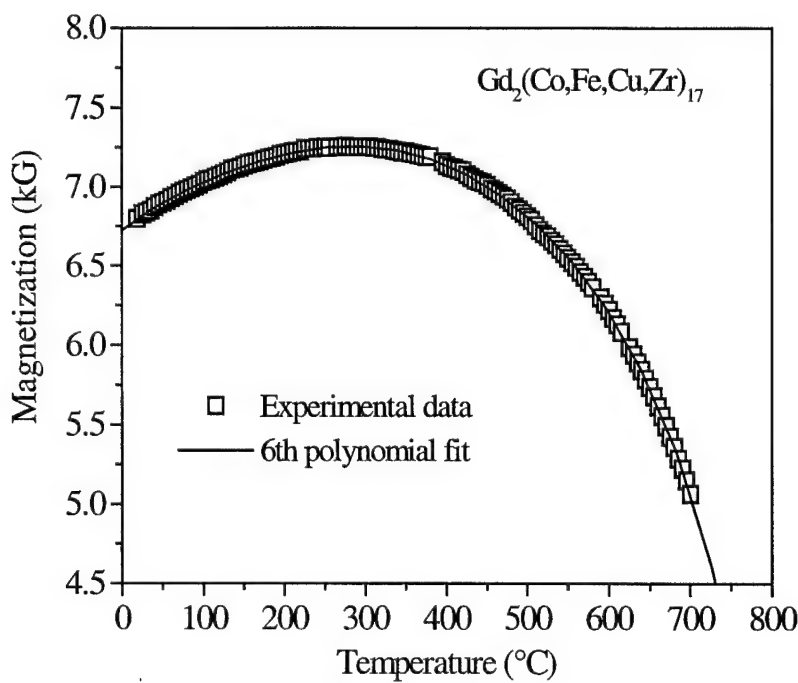


Figure 3.50. Temperature dependence of $4\pi M$ at 10 kOe of $\text{Gd}_2(\text{Co,Fe,Cu,Zr})_{17}$.

Figure 3.51 is a plot of α_T of magnetization at 10 kOe vs. T for commercial sintered $\text{Sm}_2(\text{Co,Fe,Cu,Zr})_{17}$, $\text{Gd}_2(\text{Co,Fe,Cu,Zr})_{17}$, SmCo_5 , GdCo_5 , and Nd-Fe-B magnets.

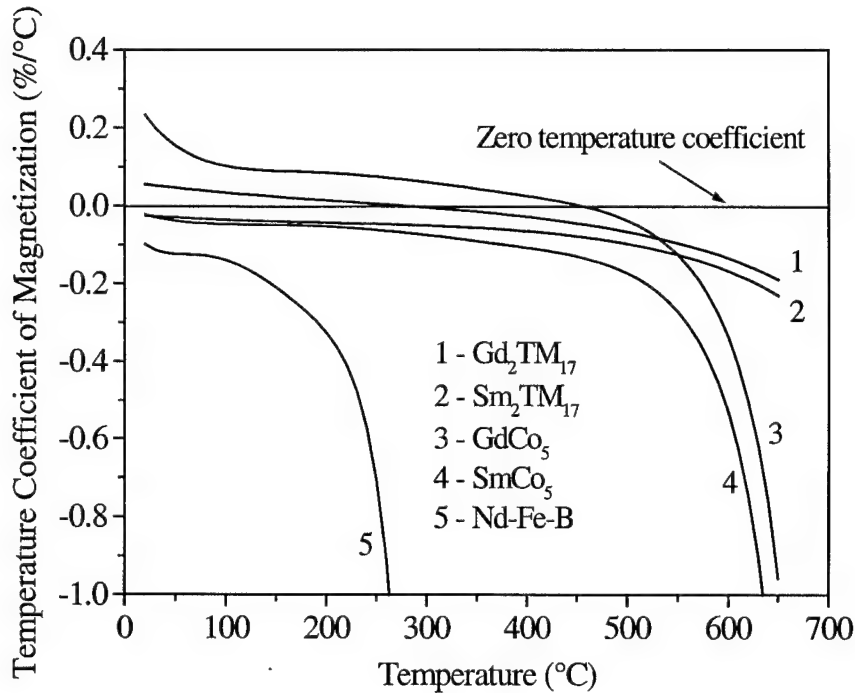


Figure 3.51. α of $4\pi M$ at 10 kOe of some rare earth permanent magnets.

It can be seen from Figure 3.51 that only curves of HRE permanent magnets $\text{Gd}_2(\text{Co,Fe,Cu,Zr})_{17}$ and GdCo_5 (curves 1 and 3) have a region of positive α . Generally speaking, α_T vs. T curves of 2:17 magnets are flatter than those of 1:5 magnets because 2:17 magnets have a higher T_C . It can be also seen from Figure 3.51 that the Nd-Fe-B magnet demonstrates very high thermal sensitivity.

Figure 3.52 and Figure 3.53 show α_T of MH_c and $(BH)_{\text{max}}$ vs. T for sintered $\text{Sm}_2(\text{Co,Fe,Cu,Zr})_{17}$, SmCo_5 , and Nd-Fe-B magnets, respectively. It can be seen from these figures that $\text{Sm}_2(\text{Co,Fe,Cu,Zr})_{17}$ has better α_T of MH_c and $(BH)_{\text{max}}$ than SmCo_5 at high temperatures. Nd-Fe-B demonstrates the highest temperature sensitivity of all of the materials.

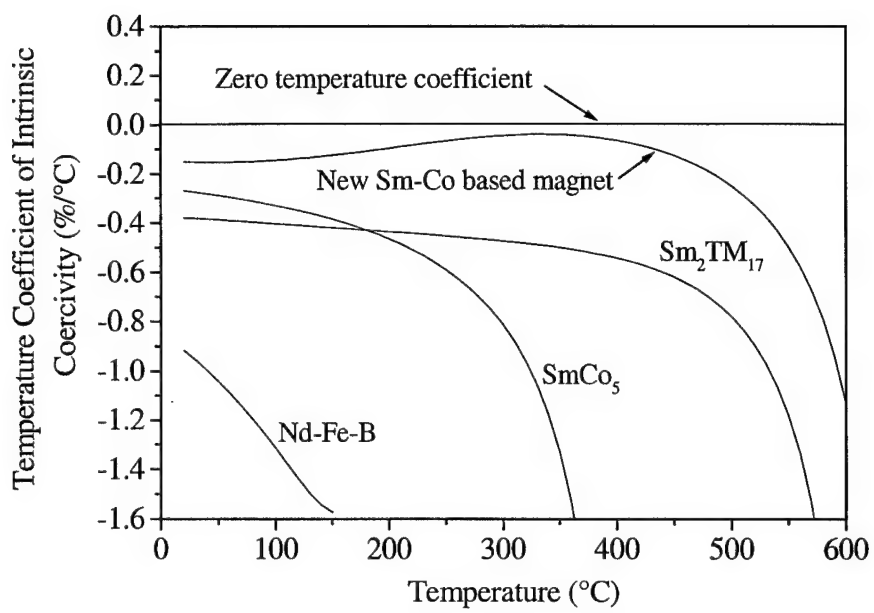


Figure 3.52. α of ${}_{\text{M}}\text{H}_c$ of some rare earth permanent magnets.

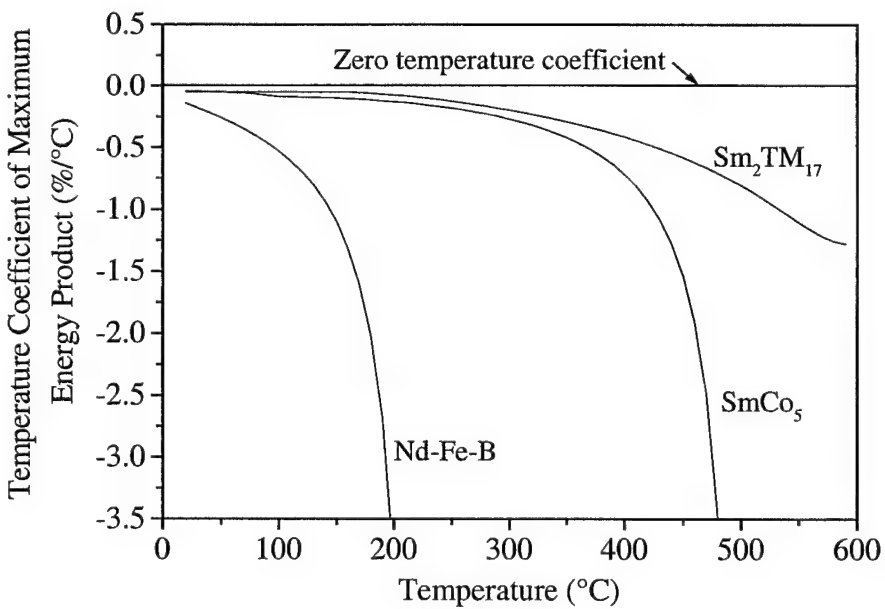


Figure 3.53. α of $(\text{BH})_{\text{max}}$ of some rare earth permanent magnets.

3.7.2 Modeling of Temperature Coefficients in (LRE-HRE)-TM Compounds

Magnetic property characterization shows that the $(BH)_{max}$ of the best commercial $Sm_2(Co,Fe,Cu,Zr)_{17}$ magnets drop as much as 40% when heated from room temperature to 400°C. For applications involving a wide temperature range, temperature compensation using an HRE is often necessary. In order to extend the temperature compensation over a wide temperature range (for example, from 20 to 500°C), more than one HRE may be required. A project of this nature typically requires considerable laboratory effort to determine the optimum combination of the LRE and the HREs. In research practice, a method of blending powders is often used. For example, by melting only two alloys of $SmCo_5$ and $GdCo_5$, any alloy having the composition of $(Sm_{(1-x)}Gd_x)Co_5$, with $0 < x < 1$, can be obtained by blending powders of $SmCo_5$ and $GdCo_5$. We have used the approach of calculating the α of magnetization of $(LRE_{(1-x)}HRE_x)$ -TM alloys to eliminate much of the time and cost of blending powders experimentally. The following describes this approach.

Because $4\pi M_s$ is an intrinsic property, it is possible to calculate the α of $4\pi M_s$ for a temperature-compensated RE-TM magnet based on an assumption that the magnetization of a $(LRE_{(1-x)}HRE_x)$ -TM compound is independently contributed by LRE-TM and HRE-TM, respectively. For example, we first experimentally determined the temperature dependence of $4\pi M_s$ for $SmCo_5$ and $GdCo_5$ alloys and obtained two functions $M_1(T)$ and $M_2(T)$. Then, polynomials were used to represent each of them. Following that, we “blended” (added) the two polynomials instead of blending two alloys, and obtained a third polynomial, $M_3(T) = (1-x)M_1(T) + xM_2(T)$, where $0 \leq x \leq 1$. Next, we used Equation (3-15) to determine the derivative of $M_3(T)$. Finally, using Equation (3-16) we derived the α_T of the new “alloy” at any specific temperature. In other words, we established the α_T vs. T relationship for the new “alloy”.

The concept of calculating $4\pi M_s$ in HRE-substituted rare earth permanent magnets was first proposed by F. E. Camp et al. [44, 45]. However, the approach they used for the calculation and their algorithms employed were not mentioned. We proposed to use a polynomial to represent the temperature dependence of $4\pi M_s$ and moved one step forward by proposing to calculate the α of $(\text{LRE}_{(1-x)}\text{-HRE}_x)\text{-TM}$ systems [46, 47].

Using this approach, we calculated the α of $4\pi M$ of the $(\text{Sm}_{(1-x)}\text{Gd}_x)\text{Co}_5$ and $(\text{Sm}_{(1-x)}\text{Gd}_x)_2(\text{Co,Fe,Cu,Zr})_{17}$ systems with $0 \leq x \leq 1$ in the temperature range of 20 to 600°C. In a plot of α_T vs. T , when α_T changes its sign from positive to negative, the α_T vs. T curve crosses the line of $\alpha_T = 0$, and determines the temperature at which the α_T becomes zero for magnets with various HRE contents. We determined the temperatures corresponding to the $\alpha_T = 0$ points for $4\pi M$ at 10 kOe applied field for $(\text{Sm}_{(1-x)}\text{Gd}_x)_2(\text{Co,Fe,Cu,Zr})_{17}$ and $(\text{Sm}_{(1-x)}\text{Gd}_x)\text{Co}_5$ systems with $0 \leq x \leq 1$ and compared the temperature compensation effect of Gd in these two systems.

Figure 3.54 is a plot of α_T of $4\pi M$ at 10 kOe of $(\text{Sm}_{(1-x)}\text{Gd}_x)\text{Co}_5$ vs. T . The temperatures corresponding to the $\alpha_T = 0$ points for magnets with various Gd contents are summarized in Table 3-9. The effects of Gd compensation on α_T of $4\pi M$ in $(\text{Sm}_{(1-x)}\text{Gd}_x)\text{Co}_5$ and $(\text{Sm}_{(1-x)}\text{Gd}_x)_2(\text{Co,Fe,Cu,Zr})_{17}$ systems are summarized in Figure 3.55. Figure 3.55 also shows the variation of $4\pi M$ of $(\text{Sm}_{(1-x)}\text{Gd}_x)\text{Co}_5$ and $(\text{Sm}_{(1-x)}\text{Gd}_x)_2(\text{Co,Fe,Cu,Zr})_{17}$ versus Gd content. It is obvious from Table 3-9 and Figure 3.55 that Gd shows a much stronger effect for temperature compensation in the $(\text{Sm}_{(1-x)}\text{Gd}_x)\text{Co}_5$ system than in the $(\text{Sm}_{(1-x)}\text{Gd}_x)_2(\text{Co,Fe,Cu,Zr})_{17}$ system. However, it must also be noted that the temperature compensation effects are at the expense of $4\pi M$ in both systems.

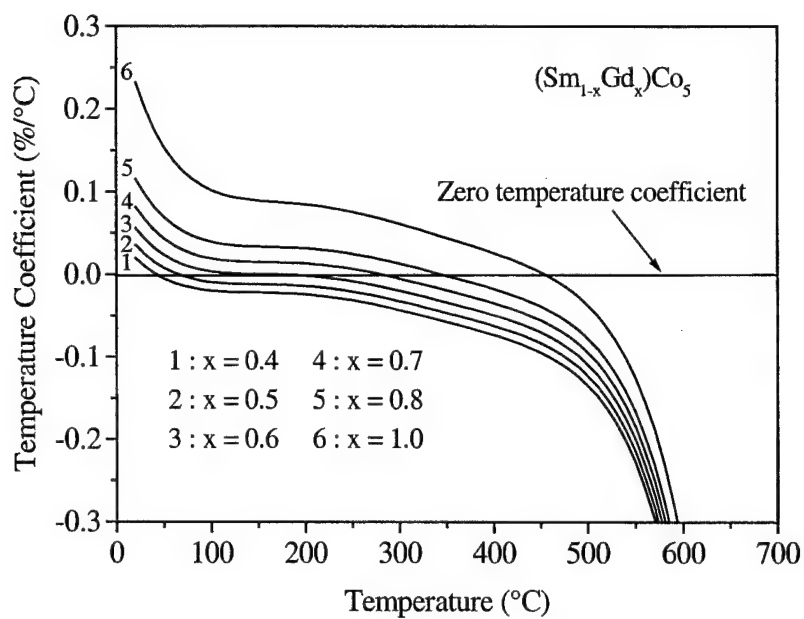


Figure 3.54. α of $4\pi M$ at 10 kOe of $(\text{Sm}_{1-x}\text{Gd}_x)\text{Co}_5$ vs. temperature.

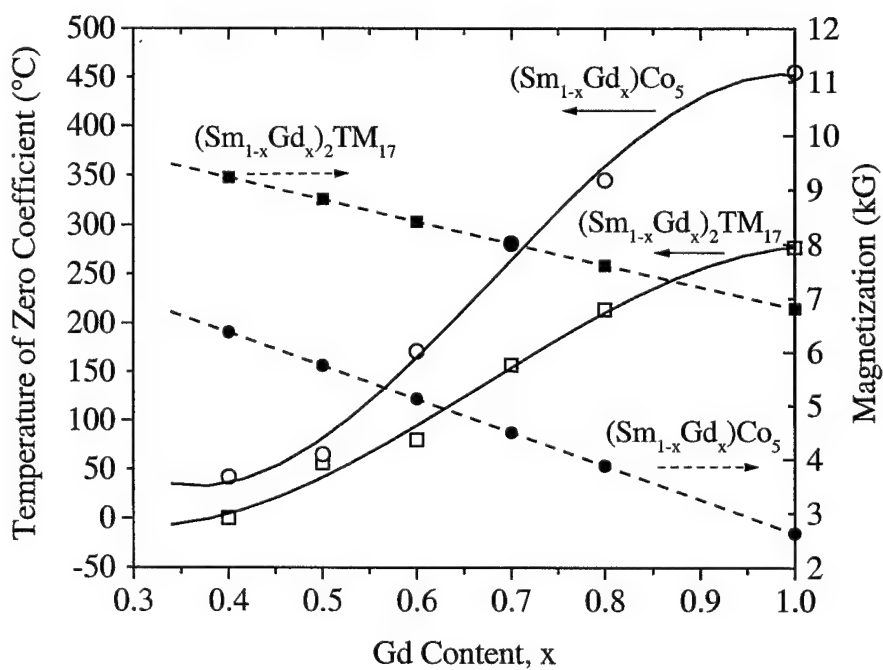


Figure 3.55. Temperature for zero α of $4\pi M$ and $4\pi M$ vs. Gd content in $(\text{Sm}_{1-x}\text{Gd}_x)\text{Co}_5$ and $(\text{Sm}_{1-x}\text{Gd}_x)_2\text{TM}_{17}$ systems.

Table 3-9. Temperatures for Zero α of $4\pi M$ for $(\text{Sm}_{(1-x)}\text{Gd}_x)\text{Co}_5$ and $(\text{Sm}_{(1-x)}\text{Gd}_x)_2(\text{Co},\text{Fe},\text{Cu},\text{Zr})_{17}$ Magnets

| Gd content, x | Temperature for zero α (°C) | |
|---------------|---|--|
| | $(\text{Sm}_{(1-x)}\text{Gd}_x)\text{Co}_5$ | $(\text{Sm}_{(1-x)}\text{Gd}_x)_2\text{TM}_{17}$ |
| 0.4 | 42 | 0 |
| 0.5 | 65 | 56 |
| 0.6 | 171 | 80 |
| 0.7 | 281 | 157 |
| 0.8 | 345 | 214 |
| 1.0 | 455 | 277 |

3.8 Preliminary Results of Nanocrystalline Composite Permanent Magnet Materials

Three compositions of Sm-Co-Fe-M have been chosen for the study of Sm-Co nanocomposite magnets. Small quantity of C, and/or Ti, or Nb was added to the Sm-Co-Fe system to make it easier to form amorphous alloys. The compositions of the ribbons are summarized in Table 3-10. The cast alloys and ribbons were prepared by induction melting and a melt spinning process at the Rhodia plant in Phoenix, AZ.

Table 3-10. Composition of Sm-Co-Fe-M-C Ribbons

| Sample | M | x | Sm | Co | Fe | C | Ti | Nb |
|---|----|--------|-------|-------|-------|-------|-------|-------|
| $\text{Sm}(\text{Co}_{0.773}\text{Fe}_{0.186-x}\text{M}_x\text{C}_{0.041})_{10.44}$ | | | (wt%) | (wt%) | (wt%) | (wt%) | (wt%) | (wt%) |
| $\text{Sm}(\text{Co}_{0.773}\text{Fe}_{0.186}\text{C}_{0.041})_{10.44}$ | | 0 | 20.34 | 64.30 | 14.66 | 0.70 | | |
| $\text{Sm}(\text{Co}_{0.773}\text{Fe}_{0.186}\text{Ti}_{0.0205}\text{C}_{0.041})_{10.44}$ | Ti | 0.0205 | 20.38 | 64.45 | 13.08 | 0.70 | 1.39 | |
| $\text{Sm}(\text{Co}_{0.773}\text{Fe}_{0.186}\text{Nb}_{0.0205}\text{C}_{0.041})_{10.44}$ | Nd | 0.0205 | 20.12 | 63.62 | 12.91 | 0.69 | | 2.66 |

XRD patterns of the as-spun ribbons are shown in Figures 3.56 through 3.58. An initial phase analysis on these XRD data indicated all samples had a 1:7 structure and α -Fe. The Bragg peak intensity of the α -Fe for these ribbons with Ti and Nb was lower than $\text{Sm}(\text{Co}_{0.773} \text{Fe}_{0.186} \text{C}_{0.041})_{10.44}$ ribbons. The widths of XRD peaks suggested the large grain sizes in the as-spun ribbons. DTA data did not show any phase transition at low temperature (< 850 °C).

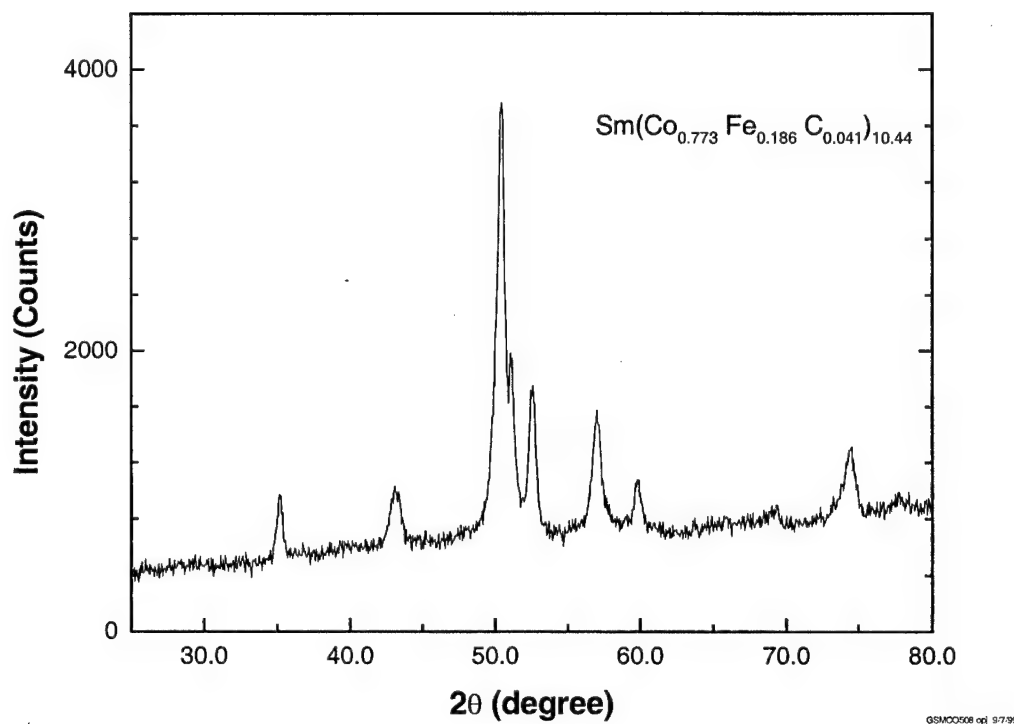


Figure 3.56. XRD patterns of as-spun ribbons for $\text{Sm}(\text{Co}_{0.773} \text{Fe}_{0.186} \text{C}_{0.041})_{10.44}$.

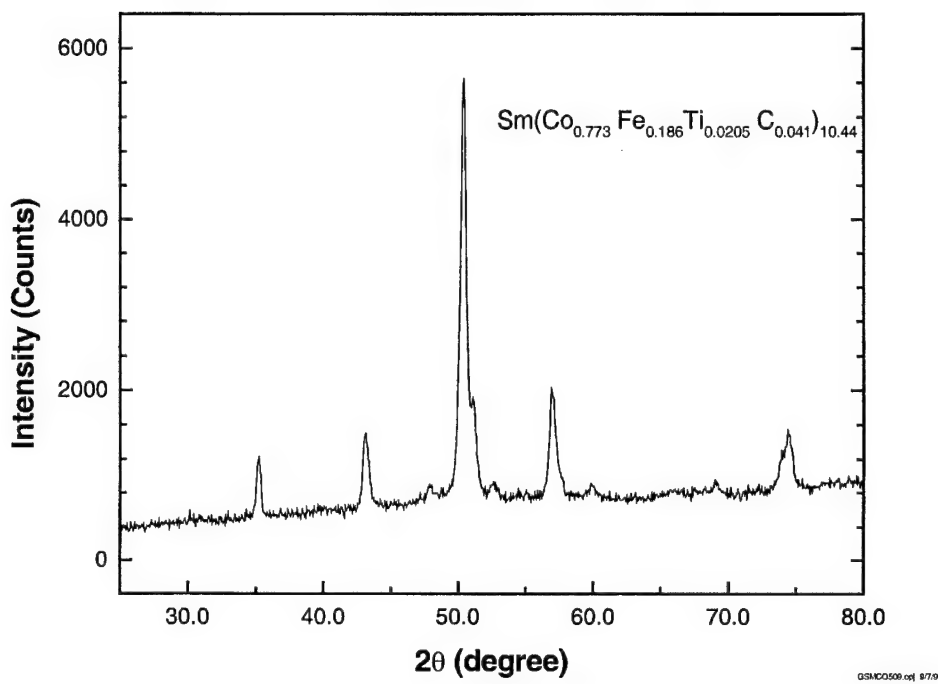


Figure 3.57. XRD patterns of as-spun ribbons for $\text{Sm}(\text{Co}_{0.773}\text{Fe}_{0.186}\text{Ti}_{0.0205}\text{C}_{0.041})_{10.44}$.

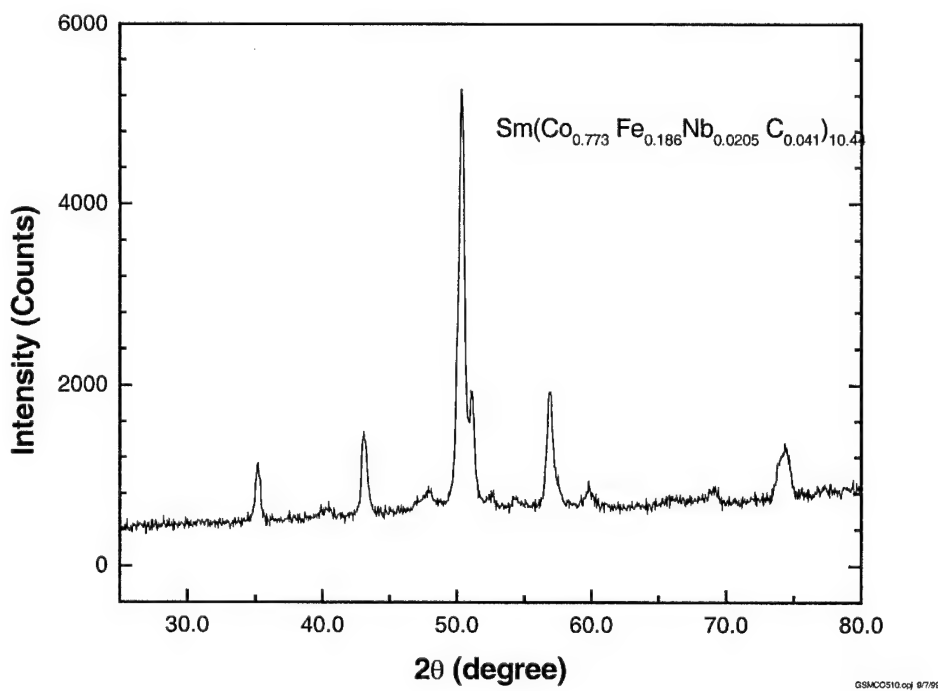


Figure 3.58. XRD patterns of as-spun ribbons for $\text{Sm}(\text{Co}_{0.773}\text{Fe}_{0.186}\text{Nb}_{0.0205}\text{C}_{0.041})_{10.44}$.

The ribbons were heat-treated at 650, 700, 750, 800 and 850°C for 10 minutes. Low coercivities of 1 to 2 kOe were obtained from the heat-treated ribbons. Magnetic properties of the ribbons are summarized in Table 3-11. In general, the magnetic properties obtained are fairly poor. This is attributed to the large grain size in the precursor and/or high amount of soft phases. The microstructure should be improved by further adjustment on the compositions and process. Because Sm-Co alloys have much higher melting temperatures as compared with Nd-Fe-B based alloys, it is more difficult to obtain nanometer scale grains or amorphous alloys. Future studies should be carried out in the following areas:

- (1) Employ additive elements to effectively enhance glass-forming capability;
- (2) Improve melt-spinning conditions to increase the cooling rate;
- (3) Use an alternative approach, for example mechanical alloying or milling, to obtain nanocomposite alloys.

Table 3-11. Magnetic Properties of "Nanocomposite" Sm-CO-based Magnets

| Sample ID | Temperature [°C] | B _r [kG] | _M H _c [kOe] | _B H _c [kOe] | (BH) _{max} [MGoe] |
|-----------|------------------|---------------------|-----------------------------------|-----------------------------------|----------------------------|
| S508 | as received | 3.72 | 0.7 | 0.6 | 0.5 |
| | 650 | 3.7 | 0.9 | 0.7 | 0.7 |
| | 700 | 3.7 | 0.8 | 0.7 | 0.6 |
| | 750 | 3.1 | 0.9 | 0.7 | 0.6 |
| | 800 | 2.4 | 0.9 | 0.7 | 0.18 |
| | 850 | 0.25 | 1.18 | 0.78 | 2.86 |
| S509 | as received | 3.2 | 1.0 | 0.8 | 0.5 |
| | 650 | 3.4 | 0.8 | 0.6 | 0.5 |
| | 700 | 3.5 | 1.0 | 0.8 | 0.6 |
| | 750 | 3.9 | 1.0 | 0.8 | 0.9 |
| | 800 | 2.3 | 0.9 | 0.7 | 0.4 |
| | 850 | 2.8 | 1.0 | 0.7 | 0.5 |
| S510 | as received | 3.3 | 1.0 | 0.8 | 0.7 |
| | 650 | 3.3 | 0.9 | 0.7 | 0.6 |
| | 700 | 3.5 | 0.9 | 0.7 | 0.6 |
| | 750 | 2.2 | 0.9 | 0.7 | 0.4 |
| | 800 | 2.4 | 0.8 | 0.6 | 0.2 |
| | 850 | 2.5 | 0.9 | 0.7 | 0.5 |

4. CONCLUSIONS AND RECOMMENDATIONS

The research efforts conducted by UDRI/EEC/Rhodia team under the ONR/DARPA AMPS program resulted in a complete success. Not only were new high temperature magnets with a breakthrough maximum operating temperature developed with properties adequate for many high temperature applications, but they were also successfully commercialized during the course of the program by EEC. Outstanding accomplishments in the program included:

- Effects of Sm, Co, Fe, Cu, Zr on high temperature performance of 2:17 type magnets were systematically investigated and these effects were thoroughly understood.
- Intrinsic coercivity of the new sintered magnets reached 9 kOe at 500°C; four to nine times higher than conventional high temperature magnets.
- Induction demagnetization curves of the new magnets remain linear up to as high as 550°C, 250 to 350°C higher than the conventional high temperature magnets.
- The maximum operating temperature of permanent magnets was increased by as much as 250°C, to 550°C.
- Sintered magnets with constant intrinsic coercivity from room temperature to 450°C and magnets with positive temperature coefficients of intrinsic coercivity were made.
- New high temperature magnets showed very good long-term stability and excellent dynamic performance at high temperatures.
- In order to explain the abnormal temperature dependence of intrinsic coercivity, a new model of coercivity mechanisms was proposed. This deepened our understanding of magnetic hardening in 2:17 type magnets and domain wall motion in magnetic materials.

Because the new operating temperature had not previously existed for permanent magnets, essentially no permanent magnet device designs that currently exist that can directly use these magnets. New designs will have to be accomplished before the unique magnetic properties of these new magnets can be fully demonstrated.

It is highly recommended that there be a follow-on program to the one described in this report that demonstrates the operability of these magnets in an actual system that operates at temperatures comparable to the magnet performance limits. The follow-on program would develop these magnets and report on the actual device performance in an operational environment. Since performance at high temperatures is at the expense of room temperature performance, the operating temperature and the operating load line of the device need to be defined before the magnet composition can be defined. Once the operating temperature is defined, the values of w, v, x, y, and z can be optimized for the $\text{Sm}(\text{Co}_w\text{Fe}_v\text{Cu}_x\text{Zr}_y)_z$ magnets to be produced.

It is also highly recommended that additional materials research be performed to develop new high temperature permanent magnet materials with magnetic properties superior to $\text{Sm}_2\text{TM}_{17}$ system. In some RE-TM systems, there exist 1-13 or 3-29 compounds which have both higher saturation magnetization and higher Curie temperature than the 2:17 compound. Therefore, these new compounds can potentially be developed into new high temperature permanent magnets. However, neither SmCo_{13} nor $\text{Sm}_3\text{Co}_{29}$ exist in the binary Sm-Co system. It is possible that these compounds may be formed by either adding a third element or through a special synthesis process, such as melt spinning or mechanical alloying.

One final recommendation is to conduct a materials research effort to complete the development of a unified model of the development of coercivity in most technically important permanent magnets, including rare earth permanent magnets and hard ferrites. Such an effort would substantially deepen understanding of the origin of coercivity development in permanent magnets and it would serve to guide the development of new permanent magnets with even better properties than those developed under this program.

5. REFERENCES

- [1] A. E. Ray and K. J. Strnat, *IEEE Trans. Magn.* **8** (1972), 516.
- [2] A. E. Ray, *J. Appl. Phys.* **55** (1984), 2094.
- [3] A. E. Ray and S. Liu, *J. Materials Engineering and Performance* **1** (1992), 183.
- [4] S. Liu, H. F. Mildrum, and K. J. Strnat, *J. Appl. Phys.* **53** (1982), 2383.
- [5] A. S. Kim, *J. Appl. Phys.* **83** (1998), 6715.
- [6] S. Liu and E. P. Hoffman, *IEEE Trans. Magn.* **32** (1996), 5091.
- [7] B. M. Ma, Y. L. Liang, J. Patel, D. Scott, and C. O. Bounds, *IEEE Trans. Magn.* **32** (1996), 4377.
- [8] S. Liu, G. P. Hoffman, and J. R. Brown, *IEEE Trans. Magn.* **33** (1997), 3859.
- [9] C. H. Chen, M. S. Walmer, M. H. Walmer, S. Liu, E. Kuhl, and G. Simon, *J. Appl. Phys.* **83** (1998), 6706.
- [10] J. F. Liu, Y. Zhang, Y. Ding, D. Dimitrov, and G. C. Hadjipanayis, *Proc. 15th Intl. Workshop on REPM*, 1998, 607.
- [11] W. E. Wallace and K.S. Narasimhan, *Science and Technology of Rare Earth Materials* (1980), 395.
- [12] H. Saito, M. Takahashi, T. Wakiyama, G. Kodo, and H. Nakagawa, *J. Magn. Magn.* **82** (1989), 322.
- [13] K. H. Buschow and F. J.A den Broeder, *J. Less-Common Met.* **3** (1973), 191
- [14] J. Yang, O. Mao, and Z. Altounian, *IEEE Trans. Magn.*, **32** (1996), 4390.
- [15] M. Q. Huang, W. E. Wallace, and M. McHenry, *J. Appl. Phys.* **83** (1998), 6718.
- [16] P. Liu et al., to be published.
- [17] K. J. Strnat, "Rare Earth-Cobalt Permanent Magnets," ed. E.P. Wohlfarth and K.H.J. Buchow, Elsevier Science Publishers B.V. (1988), 154.
- [18] University of Dayton Magnetics Lab unpublished data.
- [19] M. G. Benz, R. P. Laforce, and D. L. Martin, AIP Conf. Proc. 1974, No.18/2, eds. C. D.Graham and J. J. Rhyne (American Institute of Physics, New York), p. 1173
- [20] F. G. Jones and M. Tokunaga, *IEEE Trans. Magn.* **12**, 1976, p. 968

- [21] R. J. J. Martis, N. Gupta, S. G. Sankar and V.U.S. Rao, *J. Appl. Phys.* **49** (1978), 2070.
- [22] K. S. V. L. Narasimhan, 1981, *J. Appl. Phys.* **52**, p.2512.
- [23] D. Li, E. Xu, J. Liu, and Y. Du, *IEEE Trans. Magn.* **16** (1980), 988
- [24] D. Li, J. Liu, S. Zhou, X. Jin, and E. Xu, *Proc. 7th Int. Workshop on Rare Earth Permanent Magnets and Their Applications*, China Academic Publishers (1983), 495
- [25] H. F. Mildrum, J. B. Krupar and A. E. Ray, *J. Less-Common Met.* **93** (1983), 261.
- [26] E. F. Kneller and R. Hawig, *IEEE Trans. Magn.* **27** (1991), 3588.
- [27] A. Manaf, M. Leonowicz, H. A. Davies, and R. A. Buckley, *Proc. 12th Int'l. Workshop on REPM and Their Appl.* (1992), 1.
- [28] R. Skomski, *J. Appl. Phys.* **76** (1994), 7059.
- [29] T. Schrefl, J. Fidler, and H. Kronmuller, *Phys. Rev. B* **49** (1994), 6100.
- [30] W. Gong and G. C. Hadjipanays, *J. Appl. Phys.* **75** (1994) 6649.
- [31] J. F. Liu, H. A. Davies, and R. A. Buckley, *Proc. 13th Int'l. Workshop on REPM and Their Appl.* (1994), 79.
- [32] S. Hirosawa and H. Kanekiyo, *Proc. 13th Int'l. Workshop on REPM and Their Appl.* (1994), 87.
- [33] K. O'Donnell, C. Kuhrt, and J.M.D. Coey, *J. Appl. Phys.* **76** (1994), 7068.
- [34] J. M. Yao, T. S. Chin, and S. K. Chen, *J. Appl. Phys.* **76** (1994), 7071.
- [35] A. E. Ray, *IEEE Trans. Magn.* **20** (1984), 1614.
- [36] A. E. Ray, *J. Appl. Phys.* **67** (1990), 4972
- [37] J. Fidler, P. Skalicky, and F. Rothwarf, *IEEE Trans. Magn.*, **19** (1983), 2041.
- [38] K. J. Strnat, "Rare Earth-Cobalt Permanent Magnets," ed. E. P. Wohlfarth and K. H. J. Buchow, Elsevier Science Publishers B.V. (1988), 131.
- [39] J. D. Livingston and D. L. Martin, *J. Appl. Phys.* **48** (1977), 2608.
- [40] H. Nagel, *J. Appl. Phys.* **50**, 1026 (1979).
- [41] R. K. Mishra, G. Thomas, T. Yoneyama, A. Fukuno, and T. Ojima, *J. Appl. Phys.* **52** (1981), 2517.

-
- [42] A. E. Ray, W. A. Soffa, J. R. Blachere, and B. Zhang, *IEEE Trans. Magn.* **23** (1987), 2711.
 - [43] B. Zhang, J. R. Blachere, W. A. Soffa, and A. E. Ray, *J. Appl. Phys.* **64** (1988), 5729.
 - [44] F. E. Camp, K .S. V. L. Narasimhan, and J. C. Hurt, *IEEE Trans. Magn.* **21** (1985), 1970.
 - [45] Bao-Min Ma, K. S. V. L. Narasimhan, and J. C. Hurt, *IEEE Trans. Magn.* **22** (1986), 1081.
 - [46] S. Liu, A. E. Ray, and H. F. Mildrum, *Proc. 11th Intl. Workshop on REPM.* (1990), 389 .
 - [47] S. Liu, A. E. Ray, and H. F. Mildrum, *J. Appl. Phys.* **67** (1990), 4975.

APPENDIX: PUBLICATIONS

The work supported by ONR/DARPAR AMPS program under this contract has resulted in fifteen publications. Eight of them were published and another seven will be published in 2000. The publications are as follows:

1. Marlin S. Walmer, Christina Chen, Michael Walmer, Sam Liu, and Ed Kuhl, "New Class of High-Temperature Permanent Magnets," to be presented at *16th International Workshop on Rare-Earth Magnets*, Sendai, Japan, September, 2000.
2. Sam Liu, Ed Kuhl, Christina Chen, Michael Walmer, Wei Gong, and J.P. Liu, "New Sintered Permanent Magnet Materials Based on SmCo₇ Phase," to be presented at *16th International Workshop on Rare-Earth Magnets*, Sendai, Japan, September, 2000.
3. Sam Liu, Ed Kuhl, Christina Chen, Marlin Walmer, Michael Walmer, Wei Gong, "High Temperature Sm₂(Co,Fe,Cu,Zr)₁₇ Magnets and their Dynamic Thermal Stability," to be presented at *16th International Workshop on Rare-Earth Magnets*, Sendai, Japan, September, 2000.
4. Sam Liu and Ed Kuhl, "Coercivity mechanisms in 2:17 type of permanent magnets," to be presented at *16th International Workshop on Rare-Earth Magnets*, Sendai, Japan, September, 2000.
5. Christina H. Chen, Marlin S. Walmer, Michael H. Walmer, Sam Liu, and G. Edward Kuhl, "Thermal stability at 300-550°C for a new series of Sm₂TM₁₇ materials with maximum use temperature up to 550°C," to be published in *IEEE Trans. Magn. 36* (2000).
6. Marlin S. Walmer, Christina H. Chen, Michael H. Walmer, "A new class of Sm₂TM₁₇ magnets with operating temperature up to 550°C," to be published in *IEEE Trans. Magn. 36* (2000).
7. Sam Liu, Gregory Potts, George Doyle, Jie Yang, G. Edward Kuhl, Christina Chen, Marlin Walmer, Michael Walmer, "Effect of z value on high temperature performance of Sm(Co,Fe,Cu,Zr)_z with z = 6.5 - 7.3," to be published in *IEEE Trans. Magn. 36* (2000).
8. Sam Liu, Jie Yang, George Doyle, Gregory Potts, G. Edward Kuhl, C.H. Chen, M.S. Walmer, and M.H. Walmer, "Abnormal temperature dependence of intrinsic coercivity in sintered Sm-Co based permanent magnets," *J. Appl. Phys.* **87**, 6728 (2000).

9. Christina Chen, Marlin S. Walmer, Michael Walmer, Jingfang Liu, Sam Liu, and G. Edward Kuhl, "Magnetic pinning strength for the new Sm-TM magnet materials for use up to 550°C," *J. Appl. Phys.* **87**, 6719 (2000).
10. Sam Liu and G. Edward Kuhl, "Temperature coefficients of rare earth permanent magnets," *IEEE Trans. Magn.* **35**, 3371 (1999).
11. Sam Liu, Jie Yang, George Doyle, G. Edward Kuhl, Christina Chen, Marlin Walmer, Michael Walmer, and Gerard Simon, "New sintered high temperature Sm-Co based permanent magnet materials," *IEEE Trans. Magn.* **35**, 3325, (1999).
12. Christina H. Chen, Marlin S. Walmer, Michael H. Walmer, Sam Liu, G. Edward Kuhl, and Gerard K. Simon, "New series of Sm₂TM₁₇ magnet materials for applications at temperatures up to 550°C", *Materials Research Society Symposium Proceedings 577, Advanced Hard and Soft Magnetic Materials*, 277 (1999).
13. C. H. Chen, M. S. Walmer, M. H. Walmer, Wei Gong, and Bao-Min Ma, "The relationship of thermal expansion to magnetocrystalline anisotropy, spontaneous magnetization and T_C for permanent magnets," *J. Appl. Phys.* **85**, 5669 (1999).
14. Marlin S. Walmer, Christina H. Chen, Michael H. Walmer, Sam Liu, G. Edward Kuhl, "Use of heavy rare earth element Gd in RECo₅ and RE₂TM₁₇ magnets for high temperature applications," *Proceedings of 15th International Workshop on REPM*, 689 (1998).
15. Christina H. Chen, Marlin Walmer, Michael Walmer, Sam Liu, G. Edward Kuhl, and Gerard Simon, "Sm₂(Co,Fe,Cu,Zr)₁₇ magnets for use at temperature $\geq 400^\circ\text{C}$," *J. Appl. Phys.* **83**, 6706 (1998).

REPORT DOCUMENTATION PAGE

Form Approved
OMB No. 0704-0188

Public reporting burden for this collection of information is estimated to average 1 hour per response, including the time for reviewing instructions, searching existing data sources, gathering and maintaining the data needed, and completing and reviewing the collection of information. Send comments regarding this burden estimate or any other aspect of this collection of information, including suggestions for reducing this burden, to Washington Headquarters Services, Directorate for Information Operations and Reports, 1215 Jefferson Davis Highway, Suite 1204, Arlington, VA 22202-4302, and to the Office of Management and Budget, Paperwork Reduction Project (0704-0188), Washington, DC 20503.

| | | |
|---|--|---|
| 1. AGENCY USE ONLY (Leave blank) | 2. REPORT DATE | 3. REPORT TYPE AND DATES COVERED |
| | September 2000 | FINAL; 1 June 98 - 30 Sept 00 |
| 4. TITLE AND SUBTITLE Development of New High Temperature and High Performance Permanent Magnet Materials | | 5. FUNDING NUMBERS N00014-98-1-0636 PR 00PR04238-00 |
| 6. AUTHOR(S) S. Liu and G. Edward Kuhl | | |
| 7. PERFORMING ORGANIZATION NAME(S) AND ADDRESS(ES) University of Dayton Research Institute 300 College Park Dayton, OH 45469-0170 | | 8. PERFORMING ORGANIZATION REPORT NUMBER UDR-TR-2000-00092 |
| 9. SPONSORING/MONITORING AGENCY NAME(S) AND ADDRESS(ES) US Navy Office of Naval Research Ballston Centre Tower One 800 North Quincy Street Arlington, VA 22217 | | 10. SPONSORING/MONITORING AGENCY REPORT NUMBER |
| 11. SUPPLEMENTARY NOTES | | |
| 12a. DISTRIBUTION/AVAILABILITY STATEMENT Approved for Public Release; Distribution is Unlimited | | 12b. DISTRIBUTION CODE |
| 13. ABSTRACT (Maximum 200 words) Permanent magnet materials capable of operating at high temperatures ($\geq 400^{\circ}\text{C}$) are required for advanced aerospace systems. Prior to this program, the best available high temperature permanent magnets could not operate above 300°C . The strength of conventional magnets, as characterized by their intrinsic coercivity (MH_c) drops sharply upon heating, from 20 to 30 kOe at room temperature to only 1 to 3 kOe at 500°C . This also results in nonlinear 2 nd -quadrant induction demagnetization curves (B curves) at temperatures above 200 to 300°C . A linear B curve is critical in all dynamic applications such as in generators and motors. This research advanced the maximum operating temperature of permanent magnets by as much as 250°C , to 550°C . The MH_c of these new Sm-Co based magnets reached 9 kOe at 500°C , with linear B curves to as high as 550°C . In a conventional long-term aging test (500°C in air for 1,000 hours) the new magnets show a flux density loss less than one-third that of the best conventional 2:17 magnets. Using a dynamic characterization method (cycled between 0 and -6 kOe) at 400°C , the new magnet displays a dynamic energy product more than 20 times higher than the best conventional 2:17 magnet. | | |
| 14. SUBJECT TERMS | | 15. NUMBER OF PAGES 92 |
| | | 16. PRICE CODE |
| 17. SECURITY CLASSIFICATION OF REPORT UNCLASSIFIED | 18. SECURITY CLASSIFICATION OF THIS PAGE UNCLASSIFIED | 19. SECURITY CLASSIFICATION OF ABSTRACT UNCLASSIFIED |
| | | 20. LIMITATION OF ABSTRACT SAR |